THE DEVELOPMENT OF ON-CHIP OPTOFLUIDIC DROPLET LASERS

by

HAN ZHANG

Presented to the Faculty of the Graduate School of

The University of Texas at Arlington in Partial Fulfillment

of the Requirements

for the Degree of

DOCTOR OF PHILOSOPHY

THE UNIVERSITY OF TEXAS AT ARLINGTON

May 2020

Doctoral Committee:
      Professor Yuze (Alice) Sun, Chair
      Professor Sungyong Jung
      Professor Robert Magnusson
      Professor Michael Vasilyev
      Professor Weidong Zhou

Han Zhang

han.zhang37@mavs.uta.edu

ORCID iD: 0000-0002-8555-252X

Acknowledgements

I would like to thank the following people who have helped me on my research: my supervisor Dr. Yuze (Alice) Sun, for her passion on the projects, for her support, guidance and patience; the Shimazu Institute Nano Technology Research Center and University of Texas at Arlington, for providing the facility for the fabrication of my devices. I also thank all my friends that have helped me to get through the hardships during my PhD program. Thanks to my parents for their encouragement and unconditional support.

4 22, 2020

Abstract

THE DEVELOPMENT OF ON-CHIP OPTOFLUIDIC DROPLET LASERS

HAN ZHANG, PhD

The University of Texas at Arlington, 2020

Supervising Professor: Yuze Sun

Optofluidic lasers have been an emerging field for the applications of biological sensing and diagnosis, chemical sensing, and point-of-care devices. Droplets, as optical cavities, confines whispering gallery modes with high quality factors in small volumes. Optofluidic droplet lasers have brought the droplet-based microfluidics and droplets as micro-resonators to one platform, showing potentials on applications in highly sensitive bio/chemical detection, tunable lasers, cell tracking and tissue imaging. Until now, optofluidic droplet lasers can be categorized into two types, static droplet lasers and droplet lasers on the flow. Static droplet lasers offer long lifetime for biosensing, while droplet lasers on the flow produce highly monodisperse droplets with high throughput.

My research has been mostly focused on building a platform that can combine the advantages from both static droplet lasers and droplet lasers on the flow. Firstly, we demonstrated an optofluidic droplet dye laser that is generated by an array of microfluidic nozzles fabricated on a polycarbonate chip, showing a new approach to generating on-chip laser source and laser arrays in a simple, reproducible, reconfigurable, and low-cost fashion. Next, we transfer the same idea with similar design to a Si-based platform and achieved a reconfigurable 2x2 droplet laser array, which has great potentials in applications of on-chip spectroscopic analysis and point-of-care systems. Besides the conventional spectrum-based lasing threshold analysis method, we developed

an image-based method to measure the lasing thresholds of droplet lasers from their lasing images, offering a low-cost method for the lasing characterization of droplet-based microlasers. Due to the liquid-liquid interface of droplet lasers, we reported an optofluidic droplet laser with a monolayer gain at the surface of droplets. The monolayer gain configuration fully resonates with the nature of whispering gallery modes and all the gain molecules participate in the lasing emission, leading to a low lasing-threshold system. The monolayer configuration also provides insights on the molecular density on the surface of droplets, enabling the study of molecular spacing in certain biological models. Lastly, to truly combine the long lifetime of static droplet lasers and the highly controlled size generation of droplet lasers on the flow into one platform, a pneumatic method was applied to control the size in droplet generation. With a LabView feedback control program, we achieved a droplet-on-demand on-chip optofluidic laser. This platform will offer great potentials for intra-cavity and interfacial-cavity sensing applications.

Table of Contents

List of Illustrations

List of Tables

Chapter 1

Introduction

1.1 Optofluidic lasers

Optofluidics has been an emerging field in the last two decades. The broad definition of optofluidics is a system that involves both optics and microfluidics. However, a more specific definition would be that a microsystem in which the light manipulates the fluids or the fluids manipulate the light.[1] So far, extensive studies have been explored on developing optofluidic light sources,[2] effective and miniaturized fluidic sensors with high sensitivity of integrated micro-photonic devices,[3] tunable and reconfigurable optical microdevices with the use of microfluidics.[4] On one hand, the physical properties of the fluid, such as refractive index, viscosity, flow rate and surface tension, provide the flexibility and tunability for the optical response of an optofluidic system. On the other hand, the radiation pressure, heating effects and photochemical effects[5] of the light can be utilized to manipulate the fluid.

Optofluidic lasers, as one type of optofluidic light sources, have been drawing great attention on the applications of biological sensing and diagnosis, chemical sensing, on-chip spectroscopy and point-of-care devices. Optofluidic lasers, just like most traditional lasers, have three key factors: 1. optical cavities are integrated with the use of microfluidic devices; 2. microfluidics (as gain medium) interact with optical cavities; 3. external pump source provides the energy for population inversion. Traditionally, fluorescence-based methods have been used for sensing applications, which have a broad emission band (~50 nm) of the fluorescence spectrum and all directional emission, leading to a low signal-to-noise ratio (SNR). However, the optofluidic lasers have a very narrow emission band (less than 0.5 nm) and directional light emission, resulting a high SNR. The sensitivity of optofluidic-laser-based sensing systems is three magnitudes[6] higher compared

to that of fluorescence-based methods. When compared with conventional solid-material-based lasers, optofluidic lasers also have their own advantages[1, 7]: microfluids and microfluidic networks provide flexible, reconfigurable gain mediums and optical cavities; well-established liquid lasers can be miniaturized on microfluidic devices; due to the flexibility and reconfigurability of microfluidics, novel frequency tuning mechanisms, such as mechanical stretching and pneumatic actuation, can be implemented on the optofluidic lasers. Many different types of optofluidic lasers have been developed, in terms of different optical cavities used. For example, Fabry–Pérot (FP) cavities, distributed feedback gratings (DFB) and ring resonators (RR) have been employed on optofluidic lasers with integrated microfluidic networks. Also based on the bio-compatibilities and different emission wavelengths of optofluidic lasers, organic dyes, quantum dots and fluorescent proteins are used as gain mediums for specific purposes.

1.1.1 Optical cavities

Optical cavities are the type of structures that can confine light and cause the light to be trapped to form standing waves. Here are three popular optical cavities that have been widely used for optofluidic lasers are listed as following.

First, optofluidic FP lasers. Due to the simple cavity structure and easy fabrication process of FP cavities, microfluidic devices have employed and optimized the design of FP cavities to develop optofluidic FP lasers. Helbo, *et al.*[8] demonstrated an integrated microfluidic dye laser with two metallic mirrors working as a FP cavity, as shown in Fig. 1-1(a). As the dye solution (gain medium) was passing through the microfluidic channel and optically pumped by a nanosecond pulsed laser, the interaction between dye solution and the FP cavity eventually lead to laser emission. Kou, *et al.*[9] further developed the microfluidic dye laser platform into a collinear dual-color laser system, as shown in Fig. 1-1(b). By adding two types of dyes (Rhodamine 6G and sulforhodamine) into the solution,

2
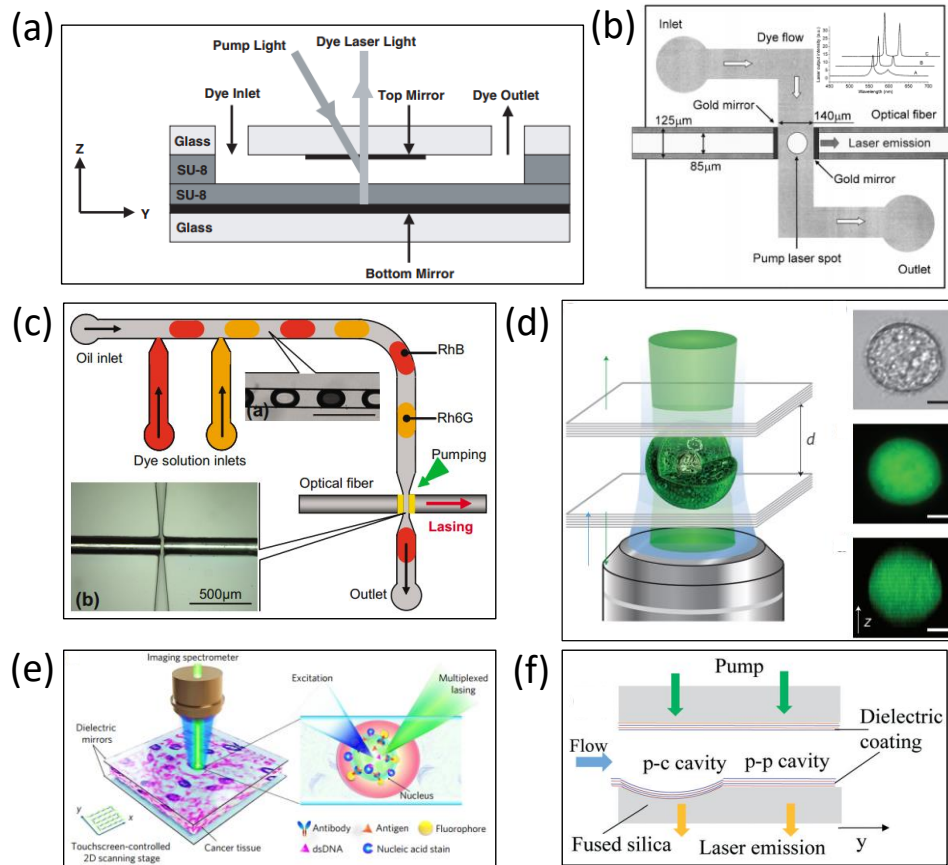
Figure 1-1 Optofluidic lasers with Fabry–Pérot (FP) cavities. (a) A micro-cavity fluidic dye laser with metallic mirrors, which serve as the FP cavity integrated within a microfluidic channel. The microfluids doped with Rhodamine 6G work as the gain medium (ref. 8). (b) A microfluidic dye laser with collinear dual-color emission. Rhodamine 6G and sulforhodamine are dissolved in the fluids, leading to simultaneous laser emission at wavelengths 559 nm and 597 nm (ref. 9). (c) A droplet-based microfluidic system that is integrated with a FP cavity has achieved single-mode lasing emissions and fast switch due to two different dyes within the droplet streams (ref. 10). (d) Single-cell lasers that utilize two highly reflective distributed Bragg reflectors (DBRs) as a high-Q FP cavity. Mammalian cells with encoded green fluorescent proteins work as gain medium (ref. 11). (e) A scanning laser-emission-based microscope. Site-specific and biomarker-specific antibody-conjugated dyes are sandwiched in a FP microcavity for building laser-emission images (ref. 12). (f) An optofluidic laser array with stable plano-concave FP microcavities (ref. 13).

simultaneous laser emission at wavelengths 559 nm and 597 nm was achieved, which

could improve the functionality of biological and chemical sensors. Aubry, *et al.*[10]

developed a droplet-based microfluidic system integrated with a FP cavity, as shown in

3

Fig. 1-1(c). By adding two different dyes into the droplet streams, the laser system not only has dual-color emission but also has achieved fast switch between two emission wavelengths. This system has potential applications in on-chip spectroscopy and flow cytometry. Gather, et al.[11] demonstrated single-cell lasers for the first time by using two highly reflective distributed Bragg reflectors (DBRs) as a high-Q FP cavity and mammalian cells with encoded green fluorescent proteins as gain medium, as shown in Fig. 1-1(d). The realization of single-cell lasers could lead to great applications on intracellular sensing, flow cytometry and tissue/cell imaging. Chen, et al.[12] and his colleagues developed a laser-emission based scanning microscope for cancer screening and diagnosis, as shown in Fig. 1-1(e). Tissue samples labelled with site-specific and biomarker-specific dyes were analyzed with a FP cavity while excited by a laser beam to build a laser-emission image. This laser-emission based microscopic system could find use in precision medicine and cell biology. Besides singe FP cavities, Wang, et al.[13] demonstrated an optofluidic FP laser array with a 2-by-2 FP cavity arrangement, as shown in Fig. 1-1(f). The laser array development can enhance the functionality of laser-based biochemical sensors and on-chip optofluidic light sources.

Second, optofluidic DFB lasers. Due the well-developed microfabrication process and easy integration of DFB gratings, optofluidic DFB lasers have been developed over the years. Balslev, et al.[14] demonstrated the first DFB grating microfluidic dye lasers. SU-8 DFB gratings worked as the resonators and Rhodamine 6G dissolved in ethanol worked as the active gain medium. Through high-order DFB gratings (in the 130s order) and multimode waveguides, single mode emission was achieved. This laser system could be suitable for polymer-based lab-on-a-chip microsystems, as shown in Fig. 1-2(a). Li, et al.[15] successfully developed a continuously tunable optofluidic DFB dye laser on a monolithic replica molded poly(dimethylsiloxane) (PDMS) chip. Due to the elastomeric nature of
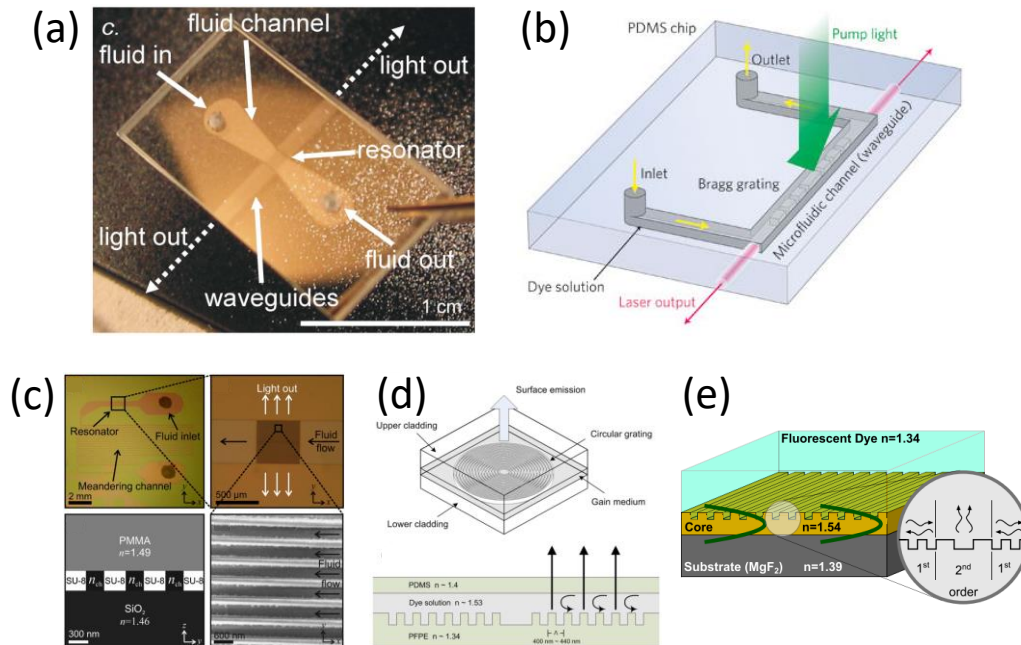
Figure 1-2 Optofluidic lasers with DFB gratings. (a) A final laser device with SU-8 DFB gratings as resonators and waveguides on both sides of the gratings. This laser worked at a high-order mode (in the 130s) (ref. 14). (b) The PDMS DFB gratings lasers with tuning ability. The laser output wavelength can be tuned by mechanically stretching the PDMS grating period due to its own elasticity (ref. 15). (c) Polymer-based third order DFB lasers with low lasing threshold due to the use of third-order DFB gratings (ref. 16). (d) Circular second-order DFB lasers with low lasing thresholds and surface emitting feature (ref. 17). (e) Second-order DFB lasers with low refractive index of the substrate and optimized resonating mode shape (ref. 18).

PDMS, through mechanical stretching and compressing ~60 nm tuning range was obtained.

To decrease the lasing threshold, Gersborg-Hansen, *et al.*[16] designed polymer-based third-order DFB optofluidic lasers integrated with an array of nanofluidic channels, as illustrated in Fig. 1-2(c). Later on, Chen, *et al.*[17] demonstrated surface emitting optofluidic dye lasers with the use of second-order DFB gratings, as illustrated in Fig. 1-2(d). Karl, *et al.*[18] optimized the mode shape for second-order Bragg grating and increased the overlapping between evanescent field and gain medium, successfully demonstrated a record-low pump threshold (of E_{TH}=520 nJ) for optofluidic DFB lasers, as illustrated in Fig. 1-2(e). Due to
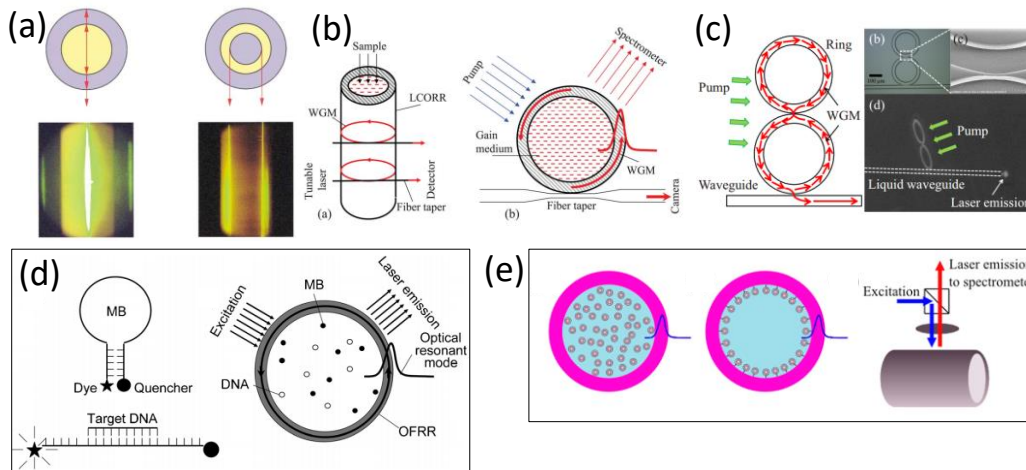
Figure 1-3 Optofluidic lasers with ring resonators (RR). (a) Cylindrical optofluidic lasers with (left) radial lasing and (right) whispering gallery mode (WGM) lasing (ref. 19). (b) Liquid core ring resonators (LCORRs) optofluidic dye lasers. With tapered fiber coupling, easy laser output is obtained (ref. 20). (c) Coupled Optofluidic ring resonator (OFRR) lasers with single mode output operation (ref. 21). (d) DNA sequences distinguishment through OFRR lasers (ref. 6). (e) Quantum-dots-based OFRR lasers (ref. 22).

the low cost and easy integration of DFB gratings, optofluidic DFB lasers can be used for developing low-cost and compact coherent light sources, highly integrated microfluidic analysis chips, and even constructing compact spectroscopic systems.

Third, optofluidic RR lasers. Through total internal reflection (TIF), light can be confined with RRs. Due to the nearly perfect spherical shape of RRs, light bounces back and forth within the microcavity for tens of thousands of times to form whispering gallery modes (WGMs) with an ultrahigh cavity Q. Moon, *et al.*[19] utilized this advantage of WGMs and achieved WGM lasing emission when the gain only interacted with the evanescent field of the WGM's. As shown in Fig.1-3(a), WGMs located within the inner surface of the single-mode fiber and gain medium resided outside the fiber, so that the cavity Q of the cross-section of fiber was not affected by the gain medium and high-Q WGMs were maintained during lasing emissions. Shopova, *et al.*[20] demonstrated liquid core ring resonators (LCORRs) optofluidic dye lasers by using a fused silica capillary with

a wall thickness of only a few microns. The core was filled with a low refractive index solvent with gain medium. The cross section of the capillary formed a high-Q RR and the evanescent field of WGMs within the inner wall of capillary interacted with fluids in the core to support laser emission. Besides, the evanescent field of WGMs extending to the capillary outer surface allowed the outcoupling of laser emission, as shown in Fig. 1-3(b). Lee, *et al.*[21] overcame the multi-mode nature of WGMs and demonstrated single-mode optofluidic ring resonator lasers through the Vernier effect. The on-chip PDMS-based two coupled ring resonators successfully suppressed the side modes and obtained a single mode operation of the OFRR through a highly efficient coupling. The single mode optofluidic OFRR lasers provided great advantages in developing on-chip laser sources and integrated on-chip optofluidic sensing systems, as shown in Fig. 1-3(c). Sun, *et al.*[6] developed an intra-cavity DNA sensing system through OFRR lasers and successfully distinguished the small hybridization differences between the target DNA strands and the single-base mismatched DNA strands, which showed the tremendous capability of OFRR lasers for bio-sensing and DNA detection purposes, as shown in Fig. 1-3(d). Kiraz, *et al.*[22] replaced the organic dye with quantum dots (QDs) as gain medium and demonstrated QD-based optofluidic lasers, as shown in Fig. 1-3(e). QDs suffered much less photobleaching than organic dyes, thus the working lifetime of QD-based optofluidic lasers could be extended.

1.1.2 Gain medium

For optofluidic lasers, the gain medium is usually homogeneously distributed in the bulk solution, which is the microfluid. Through surface chemistry, the gain medium can also be distributed on a surface that is able to interact with external pump sources. In general, the gain medium can be any materials that emit fluorescence with proper excitation. Organic dyes, fluorescent proteins and quantum dots (QDs) are three most commonly used gain media for optofluidic lasers. Organic dyes provide a large variety of

options for different emitting wavelengths, but suffer from severe photobleaching problems, which often limits the working lifespan of optofluidic lasers. Fluorescent proteins originally come from biological materials, so that through gene engineering fluorescent proteins can be directly expressed within the biological tissues and considered as biomarkers for imaging and sensing purposes. However, they also suffer from photobleaching problems. QDs can be engineered to have different emission bands by controlling the size of QDs. QDs by themselves are cytotoxic, not biocompatible, however through proper surface functionalization/modification, the biocompatibility of QDs can be increased.

1.1.3 Advantages over conventional solid-phase-based lasers

Traditional lasers are mostly based on solid-phase materials, such as semiconductor lasers, polymer-based dye lasers, Ti:sapphire lasers, Nd:YAG lasers. Once assembled, those lasers are usually bulky and hard to be integrated with other systems. Comparing with solid-phase-based lasers, optofluidic lasers have their own advantages: first, microfluids provide flexible, reconfigurable gain mediums and optical cavities; second, microfabrication technology allows the miniaturization of well-established liquid lasers on microfluidic devices; third, with the flexibility of microfluidic devices novel tuning mechanisms (such as mechanical stretching, pneumatic actuation) can be implemented.

1.2 Optofluidic droplet lasers

In principle, droplet cavities belong to the category of ring resonators, because they support WGMs through their equators. Because of the interfacial tension between droplets and their surrounding environment, droplets have nearly perfect spherical shape and optically smooth surface. When the refractive index of droplets is higher than that of the surrounding environment, the inner surface of droplets confines the light and supports WGMs with a high Q factor (10^4-10^7).[23] Meanwhile, the droplet-based microfluidic devices have been developed for droplet generation, transfer, separation and delivery. Due to their high throughput and small volume consumption, droplet-based microfluidic devices have found their applications in analyte encapsulation, drug delivery and biological/chemical process monitoring. Thus, it would be promising to utilize the optical properties of droplets to develop optofluidic lasers for bio/chemical sensors or optofluidic light sources. Based on the motion of droplets, optofluidic droplet lasers have two main types: static droplet lasers and droplet lasers on the flow. The schematics of both types of droplet lasers are as shown in Fig 1-4(a) and (b). For static droplet lasers, after being generated, droplets are supported by a superhydrophilic or superhydrophobic substrate, and stay static during the laser operation. For droplet lasers on the flow, droplets form a long series of stream and
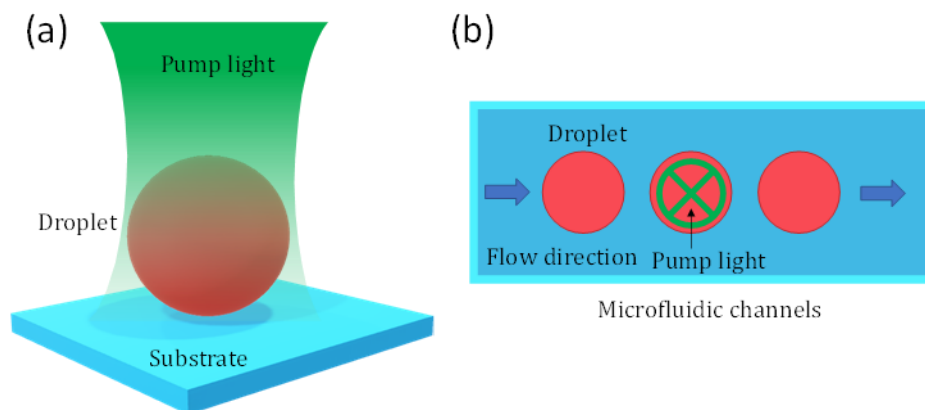
Figure 1-4 Optofluidic droplet laser schemes. (a) Static droplet lasers. (b) Droplet lasers on the flow.

continuously flow along the microfluidic channels during the laser operation.

1.2.1 Static droplet lasers

Azzouz, *et al.*[24] in Fig. 1-5(a) for the first time observed lasing emission from a levitated dye droplet, which was trapped by ultrasonic standing waves. However, due to ultrasonic waves, trapped droplets suffered from the shape deformation, deteriorating the Q factor of droplets and worsening the lasing performance. To obtain a better spherical shape for droplets, Özelci, *et al.*[25] in Fig. 1-5(b) demonstrated an optofluidic droplet laser supported by a superhydrophobic surface. In their work, the Förster resonance energy transfer (FRET) was utilized for the microlaser development, which showed a great potential on applications in highly sensitive bio/chemical detection. However, when water-based droplets are exposed to air, they suffer from water evaporation. Aas, *et al.*[26] in Fig. 1-5(c) developed oil emulsion droplet lasers in surrounding water environment to eliminate the evaporation of droplets. Through a dual-beam optical trapping method, droplets were manipulated to have different degrees of deformation of their shape, allowing all-optical tuning of laser emission wavelength. Chen, *et al.*[27] in Fig. 1-5(d) developed a different type of tunable droplet laser from self-assembled polymer with a tunable range of about 100 nm. Clearly tuned lasing modes were demonstrated by mechanical deformation. Large tunable wavelength range and flexible property offer a good platform for plastic optoelectronic devices. Humar, *et al.*[28] in Fig. 1-5(e) achieved intracellular microlasers through oil droplets and micro-beads, which can be good bio-markers for cell tracking and tissue imaging.
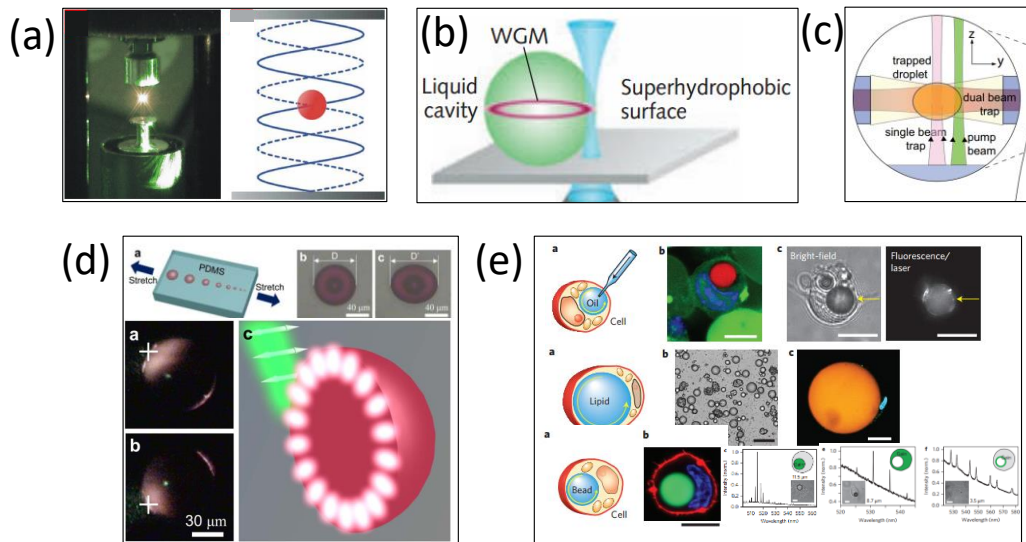
Figure 1-5 Optofluidic droplet lasers: static droplet lasers. (a) Water droplet laser was levitated by standing ultrasonic waves (ref. 24). (b) Water droplet was supported by a superhydrophobic surface, which created minimal deformation and provided high Q factor for droplet lasers (ref. 25). (c) Tunable oil emulsion droplet lasers were achieved by optically stretching in a dual-beam trap (ref. 26). (d) Self-assembled polymer droplets were embedded in PDMS. Due to the flexibility of PDMS, tunable droplet lasers were achieved through mechanical stretching (ref. 27). (e) Intracellular microlasers were demonstrated through soft (oil and lipid droplets) and solid (micro-beads) materials (ref. 28).

1.2.2 Droplet lasers on the flow

In 1986, Qian, *et al.*[29] in Fig. 1-6(a) demonstrated the first free falling droplet lasers with water-air interface. The lasing spectra helped to study the dynamical changes in droplet size, shape, and orientations. But the droplets suffered from evaporation issue. Later, Tanyeri, *et al.*[2] in Fig. 1-6(b) generated monodispersed water droplets in fluorinated oil in a microfabricated channel with high throughput and achieved lasing from the droplets. Due to their small size (~50 μm in diameter), it's good for intra-cavity bio/chemical sensing. Tang, *et al.*[30] in Fig. 1-6(c) upgraded the design of microfluidic channel and demonstrated a dual-color droplet laser with fast switching frequencies up to 3.6 kHz, showing potential applications in on-chip spectroscopy and flow cytometry. With similar microfluidic channel design, Tang, *et al.*[31] in Fig. 1-6(d) produced benzyl alcohol
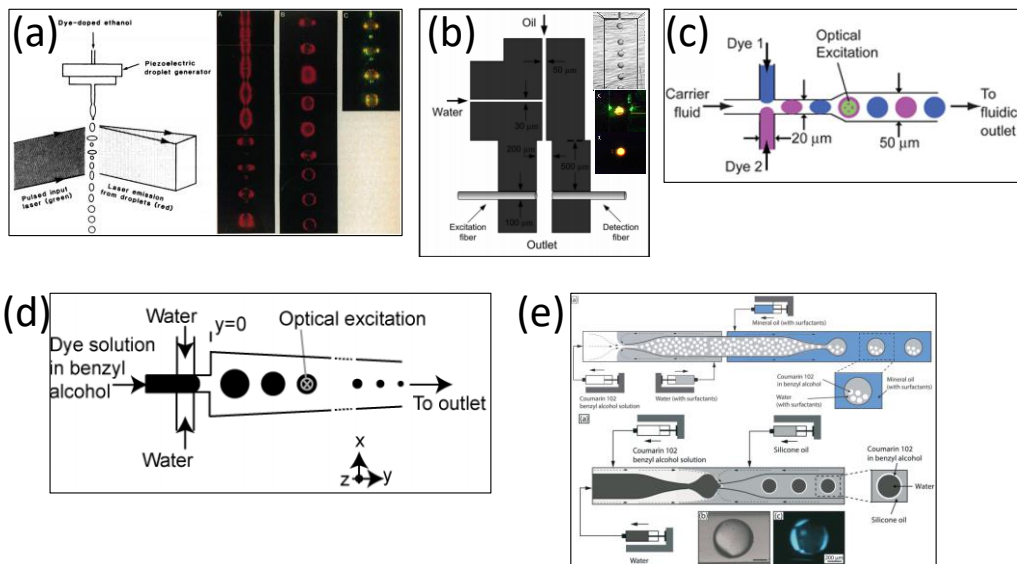
Figure 1-6 Optofluidic droplet lasers: droplet lasers on the flow. (a) Free falling water-based droplet lasers (ref. 29). (b) Water-based droplet lasers in fluorinated oil (ref. 2). (c) Dual-color fast-switching droplet lasers (ref. 30). (d) Continuously tunable droplet lasers (ref. 31). (e) Embedded droplet lasers within or around aqueous droplets (ref. 32).

droplets in water. Since benzyl alcohol and water are partially miscible, as the size of droplets decreased, tunable microdroplet lasers were achieved with wavelength of emission ranging from 620 nm to 700 nm. Double emulsion itself has been a good platform for analyte encapsulation, transportation and release. Thus, Zheng, *et al.*[32] in Fig. 1-6(e) developed embedded droplet lasers within or around aqueous droplets through double emulsion configurations, which can be useful for online monitoring of biochemical processes and sensitive detection of biomolecules.

1.2.3 Advantages and disadvantages for both types of droplet lasers

For static droplet lasers, after the droplet generation they have a long operating lifetime before their shape starts to deform. This provides enough sensing time for developing bio-sensing platforms. However, limited by their generation methods (details seen in *Section 1.4.2*) there is a large size distribution ranging from 10 μm to 100 μm. This

makes it not convenient to probe each individual droplet. For droplet lasers on the flow, due to the confinement of microfluidic channels monodisperse droplets can be generated with a high throughput and their size can be well controlled by different flow rate profiles. Because of the high generation frequency (10-1000 Hz), each droplet has a small time window (0.001-0.1 s), which makes it difficult to keep track on every droplet. It would be challenging to develop bio-sensing platforms from droplet lasers on the flow system.

1.3 Optical properties for microdroplets

1.3.1 Quality factors for microdroplets

When the refractive index of droplet is higher than that of the surrounding environment, light can be confined within the surface of droplet through total internal reflection (TIR). After a round trip, light comes back to the starting point and forms WGMs, as shown in Fig. 1-7(a).[24] According to Gorodetsky, *et al.*,[33] quality factor (Q) of microdroplets should be expressed as

$$Q^{-1} = Q_{rad}^{-1} + Q_{liquid}^{-1} + Q_{S.S.}^{-1} \qquad (1\text{-}1)$$

in Eqn. (1-1), Q_{rad}^{-1} is the intrinsic radiative (curvature) loss, reversibly proportional to the diameter of droplets. In perfect spheres or droplets, if the diameter $D/\lambda \geq 15$, radiative quality factor $Q_{rad} > 10^{11}$. Q_{liquid}^{-1} is liquid (absorption) loss, $Q_{liquid} = \frac{2\pi n}{\alpha\lambda}$ depends on the absorption of specific liquid (n – refractive index, α - absorption coefficient, λ – wavelength in vacuum). At visible wavelengths, Q_{liquid} of $\sim 10^8$ have been predicted for water microdroplets in air.[34] $Q_{S.S.}^{-1}$ is the scattering loss on residual surface inhomogeneities. Since the surface of droplet is optically smooth, the scattering loss is negligible. Estimated $Q_{S.S.}$ could reach up to $\sim 10^{11}$.[35] Therefore, the overall intrinsic Q factor for perfect spheres or microdroplets is very high (more than $\sim 10^8$). However, in the reality the shape of droplets is usually spheroid due to gravity-induced deformation or the viscous drag force
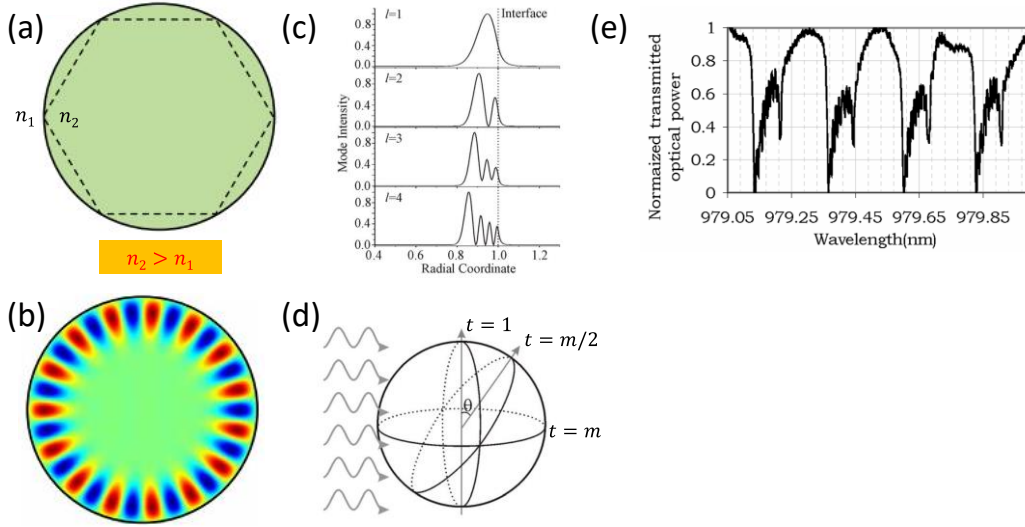
Figure 1-7 Whispering gallery modes within droplets. (a) The schematics of WGMs. When the refractive index of droplet (n_2) is higher than that of the surrounding environment (n_1), total internal reflection can be supported (ref. 24). (b) A numerical example for WGMs within droplets. Order number $l = 1$, mode number $m = 15$ (ref. 24). (c) The influence of mode order on the WGM intensity in radial field (ref. 38). (d) Each WGM has a $(2m + 1)$ azimuthal mode degeneracy (ref. 38). (e) The red shifting of azimuthal modes for a prolate spheroid (a water droplet) (ref. 23).

from the moving streams in microfluidics. This results in a decrease of Q_{rad} for the optical paths that are perpendicular to the equatorial plane of the spheroid comparing to undeformed droplets. In order to measure the Q factor for WGMs, two methods have been demonstrated, tapered fiber coupling method[35, 36] and free space coupling method.[37] Measured Q factor ranges from 10^5 to 10^8.[23]

1.3.2 Whisper gallery modes for microdroplets

The discrete wavelengths that support WGMs inside a droplet depend on the size parameter x, refractive index n and shape of the droplet. The size parameter is defined as

$$x = \frac{\pi D}{\lambda} \tag{1-2}$$

The internal field of WGMs resembles a standing wave, which is formed by m wavelengths circulating near the circumference of the droplet. The mode number m describes the WGM intensity variation in the angular distribution along the surface of

14

droplets. The radial variation of WGMs is described by mode order l. One simulated result for a WGM with order number $l = 1$, mode number $m = 15$ is presented in Fig. 1-7(b).[24] The influence of the variation of mode order on the mode intensity in radial field is presented in Fig.1-7(c).[38] It clearly shows that WGMs with higher mode order penetrate deeper into the droplet. Besides, each WGM has a $(2m + 1)$ azimuthal mode degeneracy, which is illustrated in Fig. 1-7(d).[38] The azimuthal mode number is described by t. When $t = m$, the azimuthal mode is the fundamental WGM mode with mode number m. However, the deformation of a droplet toward a spheroid would lead to the emerging of the azimuthal mode degeneracy on spectrum. The wavelength spacing between a azimuthal mode and the fundamental mode is $(m - |t|)\delta\lambda_{ec}$, where $\delta\lambda_{ec}$ is[23, 39, 40]

$$\delta\lambda_{ec} = \pm\frac{\Delta\lambda_{FSR}\varepsilon^2}{2} \qquad \left(\varepsilon = \frac{\sqrt{a^2 - b^2}}{a}\right) \tag{1-3}$$

in which, a is the equatorial radius, b is the axial radius, ε is the eccentricity of the spheroid, respectively. $\Delta\lambda_{FSR}$ is the free spectral range of two adjacent fundamental WGMs. The positive/negative sign in Eqn. (1-3) stands for an oblate/prolate spheroid. In terms of spectrum, the prolate spheroid would have a red shift for the resonant wavelengths of azimuthal modes; the oblate spheroid would have a blue shift for the resonant wavelengths of azimuthal modes. As shown in Fig. 1-7(e), the transmission spectrum of a fiber-taper coupled to the water droplet (diameter is 1 mm) presents a red shift of the azimuthal modes, which means the water droplet is a prolate spheroid.[23]

1.3.3 WGM lasing emissions from microdroplets

When dye-doped droplets are excited by an external laser source, once the round-trip gain from gain medium exceeds the round-trip loss from absorption and radiation leakage of droplets, WGM lasing emissions emerge. As illustrated in Fig. 1-8(a), the schematic of the fluorescence and absorption spectra of Rhodamine 6G in bulk ethanol.
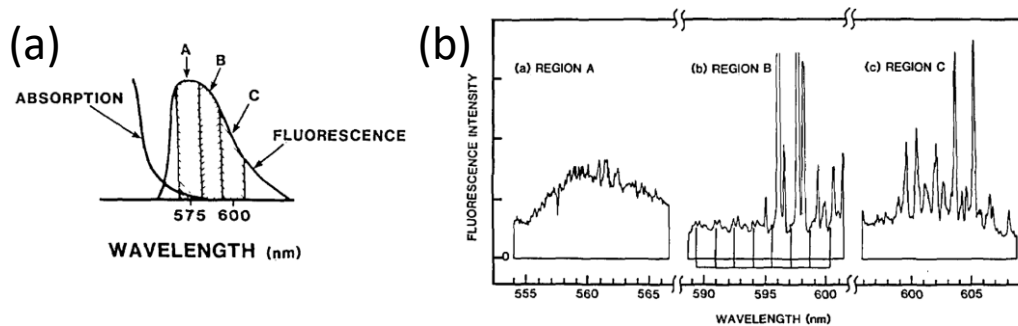
Figure 1-8 The fluorescent and lasing emission for Rhodamine 6G in ethanol. (a) The schematic of the fluorescence and absorption spectra of Rhodamine 6G in bulk ethanol (ref. 41). (b) The lasing spectrum of Rhodamine 6G in bulk ethanol droplets (ref. 41).

When the gain becomes larger than loss, the WGM lasing emission emerges from ethanol droplets doped with Rhodamine 6G, as shown in Fig. 1-8(b).[41] Regions A-C correspond to the regions in Fig. 1-8(a). The region B presents the transition from fluorescence emission to lasing emission. The cut-off wavelength is 595 nm. Therefore, when $\lambda < 595nm$, the gain is less than the loss, only fluorescence occurs; when $\lambda > 595nm$, the gain becomes larger than the loss, lasing emission is obtained. However, this is a simplified example when only one mode order is considered. When the pump energy is high enough, different higher orders of WGMs would emerge as well. Lin, *et al*. achieved lasing emission from a 15.3-μm Rhodamine 6G in water solution droplet, and identified several different mode orders of lasing took place at once.[42]
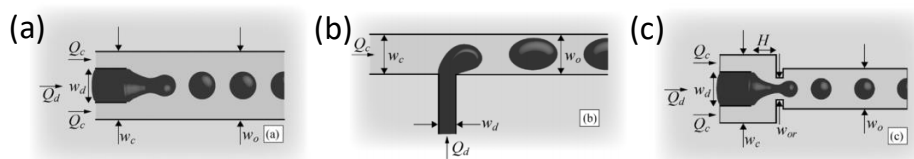
Figure 1-9 Illustration of passive generation methods for droplets. (a) Co-flowing streams (ref. 43). (b) Cross-flowing streams (ref. 43). (c) Flow-focusing geometry (ref. 43).

1.4 Microfluidics for droplet generation

Microfluidic technology has been one of the most promising methods for droplet generation. The pre-defined microfluidic channels, easy control on the fluid flow rate profiles and external active control mechanisms, all of them contribute a dynamic and monodispersed droplet generation. Thus, microfluidic technology plays an important role in utilizing the unique fluidic characteristics of droplets, such as reconfigurability, flexibility and compartmentalization.

1.4.1 Methods for droplet generation

The generation of droplets can be categorized into two types, passive generation and active generation. Passive generation methods mainly rely on the design of microfluidic channels and flow rate differences between continuous phase and dispersed phase. Driven by high pressure syringe pumps, the dispersed phase extends into a jet stream within the continuous phase. Due to the instability of interfacial tension, droplets get pinched off from the jet stream and form a series of droplets within the channels. There is no moving parts or external sources needed for passive generation methods. They can be characterized into three categories by the nature of flow pinch-off process, co-flowing streams (Fig. 1-9(a)), cross-flowing streams (Fig. 1-9(b)) and flow-focusing streams (Fig. 1-9(c)).[43] Based on different flow rate profiles between continuous phase and dispersed phase, droplets can be generated in either dripping mode or jetting mode. In dripping mode, the size of droplets is small (10-100 μm in diameter) and with a high uniformity (less than 1% standard deviation of the droplet diameter); while in jetting mode, the extended long jet stream is not stable. During the process of pinch-off, the size of droplets is not as uniform as the ones under dripping mode. Thus, dripping mode is usually more preferred in many cases that requires high uniformity of droplet size. As for active control methods on droplet generation, there are many methods having been demonstrated in recent years, such as

17

electrical control, thermal control, magnetic control, mechanical control, and piezoelectricity control.[44] To be noted that, active control methods have always been integrated with passive droplet generation methods for a better performance or more advanced control over the generation of droplets.

1.4.2 Other methods for static droplet generation

For the generation of static droplets, usually some conventional methods are used, such as ultra-sonic nebulizer, micro-injection and two-phase mixing. However, when ultra-sonic nebulizer, as shown in Fig. 1-10(a), sprays droplets out, it yields a broad size distribution of droplets due to the turbulent fluctuations during the stochastic process. Micro-injection, as shown in Fig. 1-10(b), allows to produce droplets with tens of micrometers diameter, but this method needs sophisticated setup and tools. Two-phase mixing, illustrated in Fig. 1-10(c), is another quick method to produce droplets. However, it is obvious that through handshaking or vibration the size distribution of droplets can be very broad, from 10 μm to 1 mm.

1.5 Organization of dissertation

In this dissertation, we develop and explore droplet laser systems by utilizing different types of microfluidic systems. Furthermore, our work offers a reliable on-chip
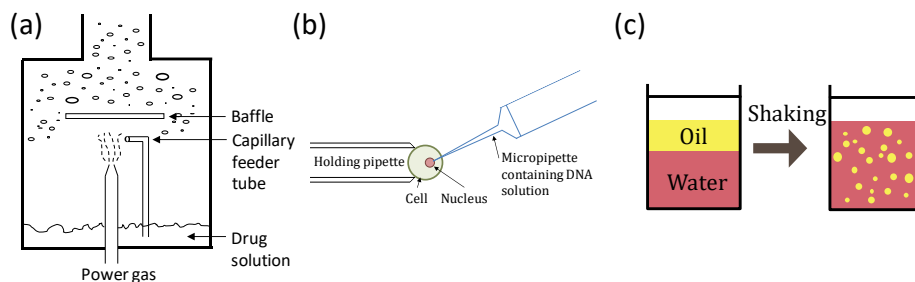
Figure 1-10 Methods for the static droplet generation. (a) Ultra-sonic nebulizer. (b) Micro-injection. (c) Two-phase mixing.

droplet laser system, which helps to develop integrated light sources and on-chip biological/chemical sensors. This study can build the bridge between droplet-based applications (such as drug delivery, compartmentalization and flow cytometry), and laser system, which promotes a more specific insight on biological or chemical reactions, molecular dynamics.

For chapter 2 and 3, lasing emission from droplets by using micro-nozzle structures was achieved. In chapter 2, droplet lasers generated by a single micro-nozzle was demonstrated, showing a prototype of our micro-nozzle structures and the capability of reconfigurable droplet lasers. In chapter 3, a droplet laser array was achieved by using a 2-by-2 micro-nozzle structure. Besides, based the images of lasing droplets, an image-based lasing threshold analysis method was performed, which can be a useful alternative method when the spectral analyzer or monochromator is not available. In chapter 4, a complete monolayer of gain medium was self-assembled at the liquid-liquid interface between droplets and the surrounding environment. The increased participation efficiency of gain medium helped to achieve lasing at a low threshold level. This work also offered an insight on the packing density of surfactant molecules at a liquid-liquid interface. In chapter 5, a droplet-on-demand on-chip optofluidic lasers was successfully demonstrated. We were able to generate different droplets ranging from 28.2 μm to 90.4 μm and the same droplet that grew from 45 μm to 80 μm with one generation round. We also achieved lasing emissions from the droplets that were generated, showing a lasing threshold as low as 1 μJ/mm^2 when the diameter of droplets was around or above 50 μm. We believe the drop-on-demand on-chip optofluidic laser platform offers great potentials for intra-cavity and interfacial-cavity sensing applications. In chapter 6, we conclude the thesis and outlook the future research plans and their potential applications.

Chapter 2

Optofluidic droplet dye laser generated by microfluidic nozzles

In this chapter, we present optofluidic droplet dye laser that is generated by an array of microfluidic nozzles fabricated on a polycarbonate chip. A droplet resonator forms upon pressurizing the nozzle backside microfluidic channel. Multimode low-threshold lasing is observed from individual microdroplets doped with dye. Additionally, droplets can be conveniently released from the nozzle by water rinsing from the top microfluidic channel and subsequently regenerated, and thus achieving optofluidic lasers on-demand. Our work demonstrates a new approach to generating on-chip laser source and laser arrays in a simple, reproducible, reconfigurable, and low-cost fashion.

2.1 Introduction

Optofluidic lasers hold great promise in the development of miniaturized coherent light source on chip. The liquid in the laser system not only offers the unique capability in laser spectral tuning and reconfiguration[10, 26, 30, 31, 45-48], but also opens up a wide variety of new applications in biosensing and medical imaging.[49-52] A number of cavity configurations have been studied in optofluidic lasers, including Fabry-Perot cavities,[10, 51-53] distributed feedback gratings,[54-56] capillary ring resonators,[49, 57-59] droplets,[29, 31, 45, 60-64] and photonic crystals.[65] Droplet microcavities can be conveniently created by using two-phase fluids, liquid droplet in air[29, 45, 63] or liquid droplet in another immiscible liquid,[31, 60-62, 64, 66] which possess a proper refractive index contrast between the droplet and its surrounding medium. Due to surface tension, the droplet has smooth surface at the two-

phase interface (air-liquid or liquid-liquid) and a perfect spherical shape, which supports whispering gallery modes (WMGs) to achieve lasing.

Lasing from droplets was first observed in a pioneering study by Chang *et al.* from a stream of free-falling dye-doped ethanol droplets in air.[29] To prevent droplet evaporation in air, later on, droplet-based optofluidic lasers were commonly made with immiscible two-phase liquids. Lasing from individual stationary droplets that are manipulated by levitation[62] and optical trapping,[60, 67] and are suspended on hydrophobic or hydrophilic surface[45, 63, 64] have been demonstrated in recent years. Lasing emission from the same stationary droplet can be continuously monitored over a prolonged period of time, which offers a unique capability when utilizing droplet lasers for biosensing applications. However, stationary droplets generated in these studies often have a large variation in droplet size. The generation process is not repeatable. Additionally, instrumentation used in droplet levitation and optical trapping is complex, which is challenging to be integrated with a droplet laser on chip. In contrast to stationary droplets, another type of droplet laser is based on a stream of droplets suspended in carrier liquid that flow in microfluidic channels.[10, 61] These monodispersed droplets can be generated with flow-focusing,[68] T-junctions,[69] and co-flowing structures[70] at frequencies up to 100 kHz. The advantages of this laser system are the capability of high-speed droplet generation and switching, and the potential to perform high-throughput on-chip spectroscopy and bioanalysis. However, droplet-on-the-flow limits the capability of tracking lasing emission from the individual droplet. High droplet generation and switching frequency pose a limiting factor that individual droplet is only interacting with the excitation light for a time duration in the range of microsecond to millisecond, which is not suitable for biosensing applications such as the development of micro-total analysis system using droplet laser-based assays.

2.2 Experimental setup
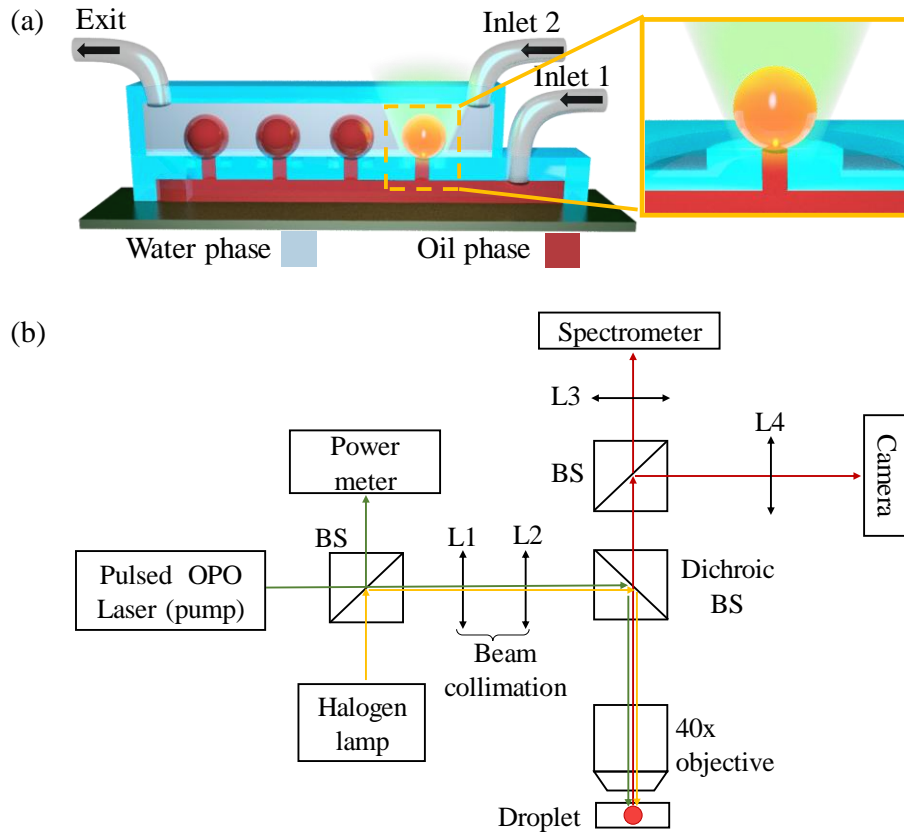
Figure 2-1 Schematics and experimental setup for the droplet laser with micro-nozzle structures. (a) Illustration of optofluidic droplet laser. Oil phase and water phase are delivered through Inlet 1 and Inlet 2 into the backside and top microfluidic channels, respectively. Upon pressurizing backside channel, oil droplets are generated on top of the micro-nozzle structures in the top channel. Droplets can be released from the nozzle by water rinsing in the top channel and regenerated subsequently. Inset: zoom-in image of one micro-nozzle with droplet. (b) The schematic illustration of the experimental setup. Pulsed optical parametric oscillator (OPO) (repetition rate: 20 Hz, pulse width: 5 ns, wavelength: 532 nm) is used for optical excitation. BS: beam splitter. L1, L2, L3, and L4 are lenses with a focal length of 5 cm, 5cm, 2.5 cm, and 2.5 cm, respectively. The fluorescent and lasing emissions from the droplets are sent to a spectrometer. The droplet is imaged by a camera, from which the droplet size is characterized. Green lines indicate pump light. Red lines indicate the emission from the droplet. Yellow lines indicate the illumination light.

Here, we demonstrate an optofluidic droplet laser with combined advantages of stationary droplet laser and droplet-on-the-flow laser, which is capable to reproducibly generate stationary droplets with well-controlled size and regenerate on-demand. The

optofluidic droplet laser is generated by the microfluidic nozzle structure with two-phase immiscible liquids. As illustrated in Fig. 2-1(a), an array of four identical nozzle structures are fabricated on a chip. The microfluidic channel is created on the backside of the chip to deliver the oil phase to the nozzles. A separate microfluidic channel is created on the topside of the chip, where aqueous phase is flowed in and out of the channel. The topside and backside microfluidic channels are connected through the nozzle holes. When a positive pressure is applied to the backside channel, the oil phase emerges from individual nozzles and simultaneously form an array of oil droplets in water (aqueous phase). The microdroplet has a refractive index (e.g., immersion oil, $n = 1.515$) higher than that of the surrounding liquid (water, $n = 1.334$), and thus forms an optical microcavity that supports whispering gallery modes (WGMs) through total internal reflection at the two-phase liquid interface. When a gain material (e.g., organic dye) is added to the oil phase, upon excitation, fluorescence emission that is coupled into the WGMs is amplified in the droplet and thus achieve lasing when the gain surpasses the loss. Due to the low absorption coefficient of the oil phase ($\alpha < 10^{-3} cm^{-1}$), the smooth surface formed at the liquid-liquid interface, and minimal contact region between droplet and nozzle, low-threshold lasing can be achieved in the droplet microcavity. Droplets generated on the nozzles can be conveniently removed by the initiation of water flow in the topside microfluidic channel and subsequently regenerated. The process of generation and regeneration is simple, reproducible, and well-controlled. The micro-nozzle chip with integrated microfluidics presents a versatile platform to achieve reconfigurable and regenerable optofluidic laser array.

2.3 Fabrication of micro-nozzle structures

To demonstrate the concept of microfluidic nozzle droplet platform, polycarbonate (PC) is used in this work. However, the concept and the device design can be readily

(a) Backside microfluidic channel

(b) Nozzle holes

Flip

(c) Nozzle rings

(d) Backside microfluidic channel inlet

(e) Substrate layer bonding

(f) Topside microfluidic channel
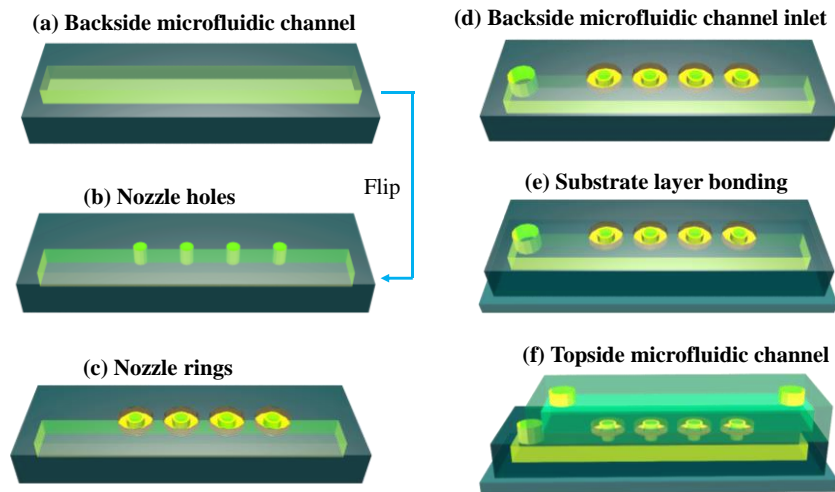
Figure 2-2 Fabrication process flow of the micro-nozzle optofluidic laser device made of polycarbonate chip.

extended to silicon, with devices made by MEMS fabrication to achieve a reduced device footprint. PC is a commonly used material in microfluidic devices in biomedical and bioanalytical applications.[71, 72] Additionally, PC is selected in prototyping our laser system because of its low cost, good machining properties, high glass transition temperature (Tg~145 °C), and transparency in the visible spectral range.[73] Due to good machining properties of PC, the fabrication of microfluidic nozzle structures is simple and straightforward. First, oil phase microfluidic channel is created on the backside of the device, as illustrated in Fig. 2-2(a), using a milling machine. Second, four identical nozzle holes are drilled from device front side to reach the backside channel, as shown in Fig. 2-
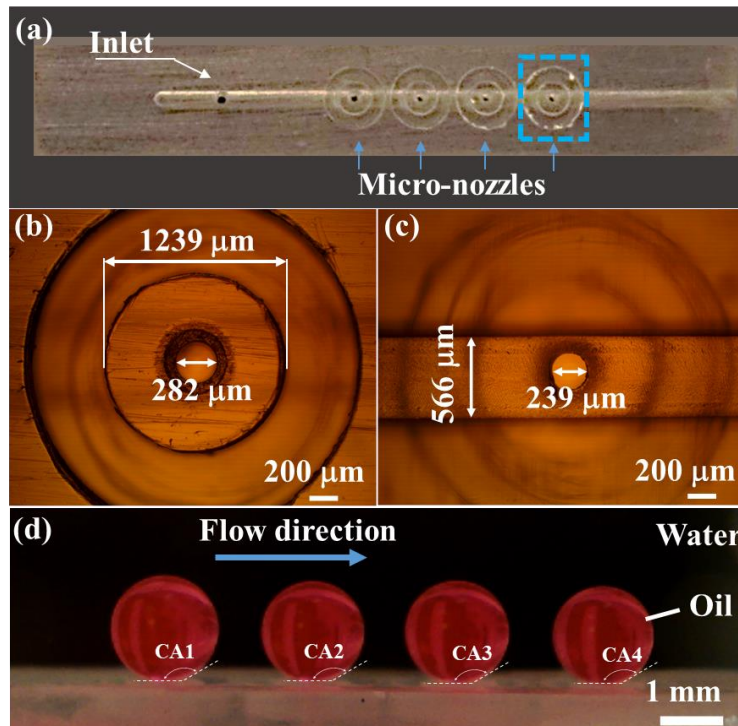
Figure 2-3 Fabricated micro-nozzle structures. (a) An image of 1x4 micro-nozzles made on polycarbonate chip before bonding to the topside microfluidic channel. (b) Top view of the device (image of the area marked in (a)), showing the nozzle hole diameter of 282 μm and the nozzle ring outer diameter of 1239 μm. (c) Backside view of the device (image of the area marked in (a)), showing the backside microfluidic channel width of 566 μm and the nozzle hole diameter of 239 μm. (d) Generation of a droplet array. The average contact angle of the four droplets is 151.1°±2.4°

2(b). Third, nozzle ring surrounding each nozzle hole are created through milling by

carving out a ring-shaped trench at the outer boundary of the nozzle ring, as shown in Fig. 2-2(c). The nozzle ring is designed to minimize the contact between droplets and the nozzle substrate. Fourth, the backside microfluidic channel inlet hole is drilled from the device front side as shown in Fig. 2-2(d). Afterwards, the nozzle PC chip and another PC substrate are sonicated in ethanol for 30 minutes, then in deionized (DI) water for 15 minutes. After air dry, both PC chips are exposed to dichloromethane (DCM) (Sigma-Aldrich) to swell the surface in a vacuum chamber for 30 minutes to facilitate thermal bonding in the next step.[73] The PC nozzle and PC substrate are subsequently bonded together at 125 $^{\circ}$C for 45 minutes, as depicted in Fig. 2-2(e). At last, the bonded device is immersed in ethanolic solution of $SnCl_2$ [20% (w/w)][74] for 8 hours and flushed with water for 5 minutes. Through this treatment, the surface of microfluidic channels becomes hydrophilic, thus decreasing the interfacial tension between microdroplet and the nozzle hence minimizing the contact area between them, which helps maintain a good Q-factor of the droplet microcavity. The surface remains hydrophilic and stable for at least 10 days when the microfluidic channels are immersed in DI water. Similarly, the topside microfluidic channel and the channel inlet

and outlet are created on another PC chip and is bonded to the device shown in Fig. 2-2(e). The final device structure is shown in Fig. 2-2(f). The fabricated nozzle chip before bonding to the topside microfluidic channel is shown in Fig. 2-3(a), where an array of 1x4 nozzles are created. The dimensions of nozzle and backside channel are shown in Figs. 2-3(b) and 2-3(c). The diameter of nozzle hole is 282 μm measured at nozzle top surface and 239 μm measured at the bottom surface. The slightly larger diameter at the top surface is caused by the tapered shape of the drill bit when drilling is conducted from the topside of the device to the backside. The nozzle ring outer diameter is 1.239 mm. The backside microfluidic channel width is 566 μm. To generate the droplet array, a home-built stepwise pump, consisting of a micrometer (Newport) and a 1 μL syringe (Hamilton), is used to deliver the oil phase to the nozzle. The pressure applied to the nozzle can be fine-tuned with a single step injection volume of nL to control and maintain the droplet to the desired size. Organic dye Nile Red (Sigma-Aldrich) dissolved in immersion oil (Sigma-Aldrich) is used as the gain material in the droplet laser. As shown in Fig. 2-3(d), with the proper control of the injection volume, an array of dye-doped droplets is generated simultaneously
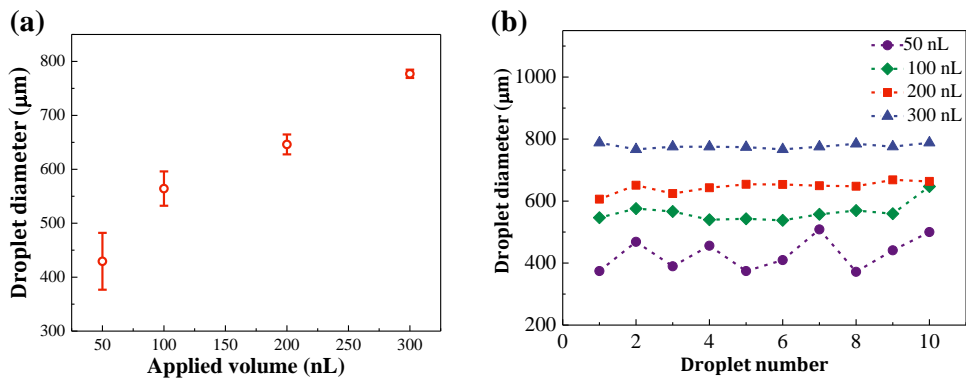
Figure 2-4 Characterization of droplet generation. (a) The relationship between injection volume applied to the backside channel and the size of the droplet generated on the nozzle. The error bar is obtained on ten droplets generated in sequence for each injection volume. (b) The droplet diameter variation at different injection volumes. A total of 40 droplets were measured.

on top of each nozzle. The spherical shape of the droplet is well maintained with minimized contact area between droplet and nozzle substrate. Contact angle of these four droplets are characterized using a side-view camera with a customized setup,[64] which reveals an average contact angle of 151.1°±2.4°. The size of four droplets are identical with a diameter of 1.584±0.058 mm. Additionally, different sizes of droplets can be generated by controlling the injection volume to the backside channel, as shown in Fig. 2-4(a). When injection volume increases from 50 nL to 300 nL, the diameter of the droplet increases accordingly. To demonstrate the generation reproducibility, a total of 40 droplets are generated in sequence, with 10 droplets in each size group. The variation in size for these droplets are shown in Fig. 2-4(b). The size measurement for these droplets are 429±53 μm, 564±32 μm, 646±18 μm, 777±7.7 μm, respectively, in diameter.

2.4 Results and discussion

To study the lasing performance, 500 μM Nile Red in immersion oil is used for laser characterization. As shown in Fig. 2-1(b), a confocal setup is used to excite the microdroplets with a pulsed optical parametric oscillator (OPO) (repetition rate: 20 Hz, pulse width: 5 ns, wavelength: 532 nm, Continuum Surelite). Pump energy is adjusted by a variable neutral density filter. The pump laser beam spot size is 10 mm^2, focused by an objective lens (40x, NA = 0.60). The laser emission signal from the microdroplet is collected via the same objective and sent to a 90/10 beam splitter. 90% of the emission light goes to the spectrometer (Horiba iHR320) for spectrum analysis and 10% of the emission light goes to the CCD camera for droplet monitoring and imaging. The emission spectrum of the droplet is obtained with single pulse excitation from the OPO laser to minimize photobleaching effect. Figure 2-5(a) shows the lasing spectra measured by the spectrometer using 600 g/mm grating from a droplet of 563 μm in diameter under pump energy densities varied from 5.7 μJ /mm^2 to 100 μ J/mm^2. Initially, fluorescence emission
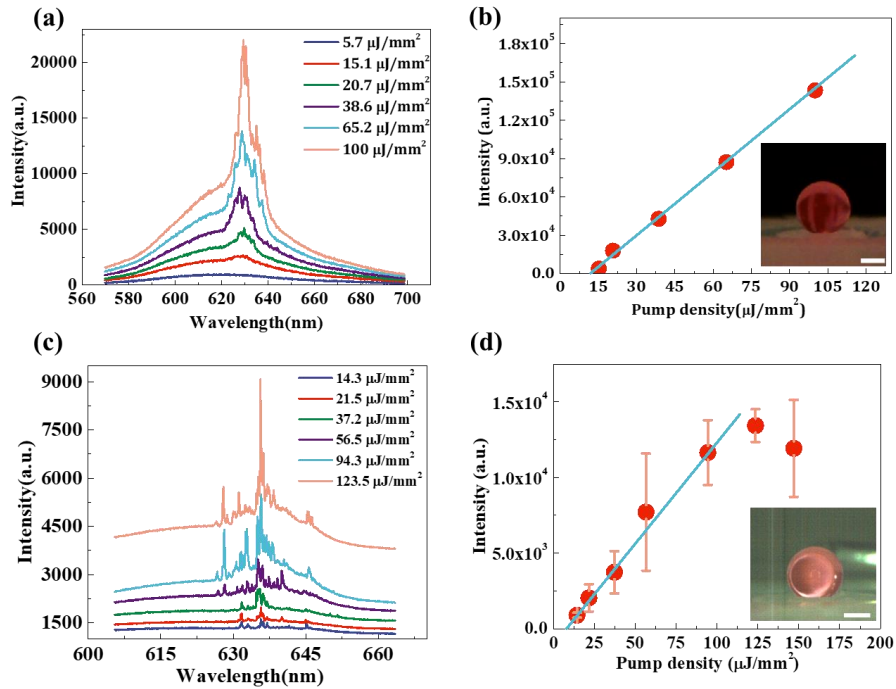
Figure 2-5 Lasing characterization for droplets generated by micro-nozzles. (a) Fluorescence and lasing emission spectra from a 563 μm diameter microdroplet under different pump energy densities. All spectra are taken under a 600 g/mm grating. (b) The plot of integrated lasing intensities as a function of pump energy density. The lasing threshold derived from the linear fitting is approximately 12 μJ/mm². (c) Lasing emission spectra from a 544 μm diameter regenerated microdroplet under different pump energy densities. All spectra are taken under a 1200 g/mm grating. Traces are shifted vertically for clarity. (d) The plot of integrated lasing intensities as a function of pump energy density. The error bar is obtained on three spectra excited under the same pump energy density. The lasing threshold derived from the linear fitting is approximately 10 μJ/mm². Insets in (b) and (d) are the side-view optical microscope images of the measured microdroplets. The scale bar is 250 μm in both images.

is observed at low pump power. Lasing emission is observed when pump energy density is at 15.1 μJ/mm² and above. The lasing peaks occur at the longer wavelength side of the Nile Red fluorescence spectrum. The maximal intensity is centered around 635 nm for lasing emission as opposed to 610 nm for fluorescence emission. The absorption spectrum of Nile Red has a peak at 542 nm and tails around 620 nm and beyond. Thus, the laser gain profile maximum is at the low absorption region of 620 – 650 nm of Nile Red, where lasing

emission should emerge first. According to the size of the droplet, free spectral range (FSR) of the WGMs supported by the droplet cavity can be calculated as

$$\lambda_{FSR} = \frac{\lambda^2}{n_g \pi D} = 0.15nm \qquad (2\text{-}1)$$

where λ is the center wavelength of lasing emission spectrum ($\lambda = 635nm$), is the refractive index of immersion oil ($n_g = 1.515$), and D is the diameter of the microdroplet ($D = 563\mu m$). The FSR cannot be fully resolved due to the limited spectral resolution of the spectrometer (spectral resolution 0.7 nm), which agrees with the measured lasing spectra in Fig. 2-5(a). After subtracting fluorescent background from the lasing spectrum, the integrated lasing intensity of each lasing spectrum is plotted as a function of pump energy density, as depicted in Fig. 2-5(b). The lasing threshold derived from the linear fitting is approximately 12 $\mu J/mm^2$.

With integrated top microfluidic channel, the droplets can be conveniently removed from the nozzle by initiation of a water flow. After water rinsing, another droplet is subsequently regenerated, as shown in the inset of Fig. 2-5(d). The size of this droplet is 544 μm in diameter. The lasing emission from the droplet is characterized with the spectrometer using 1200 g/mm grating (spectral resolution 0.3 nm). The lasing spectra under various pump energy densities are presented in Fig. 2-5(c). Three lasing spectra are taken for each pump energy density to characterize the mean and standard deviation of the lasing emission intensity. The lasing threshold curve is plotted in Fig. 2-5(d). Saturation effect is observed for pump energy density above 120 $\mu J/mm^2$. The lasing threshold derived from the linear fitting below 120 $\mu J/mm^2$ is approximately 10 $\mu J/mm^2$. The lasing threshold demonstrated here is on par with that of other droplet optofluidic lasers reported previously.[61-63, 66] The Q-factor of the droplet is estimated to be in the range of 10^4-10^5 from theoretical modeling[64] and by comparing our lasing threshold to the ones reported in

the previous work in which Q-factor is characterized experimentally.[53] The contact angle of the droplet measured is around 120°, which is smaller than that of the droplets shown in Fig. 2-3(d). The decrease in contact angle is due to relatively large size of the nozzle hole in comparison to the droplet size. The contact region can be further minimized (increase the contact angle) by decreasing the nozzle hole size either through improvement of micromachining precision or fabricating nozzle devices on a silicon chip using MEMS technologies.

As demonstrated in Fig. 2-4, droplets of a variety of sizes can be generated by controlling the injection volume to the backside channel. To characterize the lasing emission from different sizes of droplets, the emission spectra are measured when the droplets are excited at the same pump energy density, which is at ten times above the lasing threshold, while gradually increasing the droplet size. Similar lasing spectra are observed
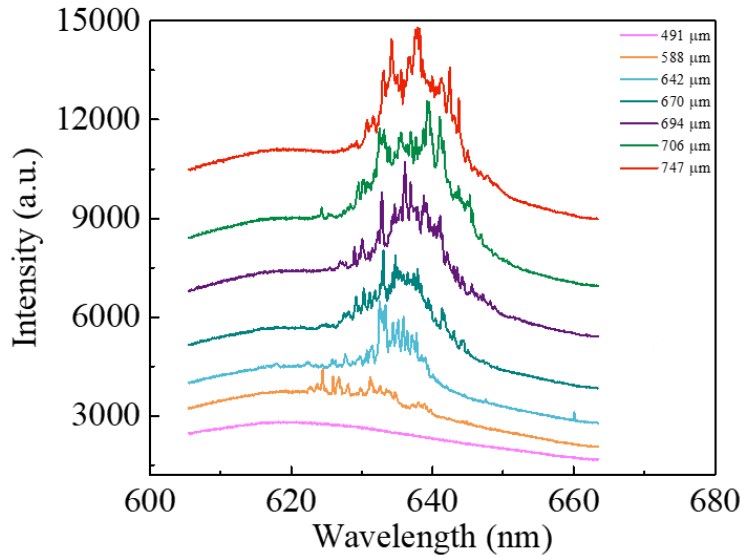
Figure 2-6 The emission spectra measurement of droplets with different sizes. The diameter of the droplets are 491 μm, 588 μm, 642 μm, 670 μm, 694 μm, 706 μm, and 747 μm, respectively.

31

from different sizes of droplets, as presented in Fig. 2-6. Only fluorescence emission is observed from a droplet of 491 μm in diameter, which is due to relatively large nozzle hole size in comparison to the droplet. When droplet size increases, lasing emission starts to emerge. The intensity of the lasing emission increases gradually with the size of the droplet. However, lasing emission spectra is observed in the range of 620 – 650 nm, regardless of the droplet size.

2.5 Conclusion

We have demonstrated an integrated optofluidic droplet laser on PC chip through microfluidic nozzle array structures. Through independent control of oil phase and aqueous phase in separate microfluidic channels, the droplet laser can be generated, removed, and re-generated in a simple and robust manner. The droplet laser design demonstrated here is transferrable to devices made of other materials, such as silicon, to further reduce device footprint. A lasing threshold of 10 $\mu J/mm^2$ is achieved, which can be further improved through increasing the contact angle of the droplet, and hence cavity Q-factor.

Chapter 3

Reconfigurable Optofluidic Droplet Laser Array

In this chapter, optofluidic lasers have been an emerging technology for the development of miniaturized light sources and biological and chemical sensors. However, most optofluidic lasers are at the single optical cavity level, which limits their applications on high-throughput biochemical sensing systems, high speed wavelength switching light sources and on-chip spectroscopic analysis. Thus, here we demonstrated an optofluidic droplet laser array system, in which four individual droplet optical cavities are supported by a 2x2 Si-based nozzle array. The lasing thresholds for droplets with a diameter ranging from 115 μm to 475 μm are obtained in the range of 0.63~2.02 μJ/mm^2. We also developed an image-based lasing threshold analyzing method, which enables the simultaneous lasing threshold analysis for every laser unit within the same laser array. Compared with spectrum-based lasing threshold analyzing method, the average lasing thresholds from the image-based method are within 6.68% difference. The accuracy of the image-based method is mainly limited by the resolution of the camera. By increasing the number of pixels per unit area, it's possible to develop a reliable spectrometer-free system for lasing threshold analysis.

3.1 Introduction

Optofluidic lasers which utilize different types of optical cavities[4, 15, 24, 29, 30, 57, 75] and have easy access to the gain medium, such as organic dyes,[15, 24, 29] fluorescent proteins[76, 77] and quantum dots,[22] have been an emerging technology in recent years. Advances in optofluidic lasers have been achieved on the development of miniaturized

33

coherent light resources[4, 13, 15, 46, 47] and biological and chemical sensors.[78-81] Up to date, various optical cavities have been studied for optofluidic lasers, such as optical ring resonators,[2, 4, 22, 24, 29, 30, 57, 75, 76, 82, 83] distributed feedback gratings (DFB),[14-16, 18, 47, 84] Fabry-Perot (F-P) cavities,[8, 9, 11, 85-91] photonic crystals[92] and random laser cavities.[93-96] However, most of the optofluidic lasers demonstrated till now are at the single optical cavity level, which poses a limitation in the development of high speed wavelength switching light sources,[30, 89, 97, 98] on-chip spectroscopic analysis[97, 99-101] and high-throughput biochemical sensing systems.[102-105] In the last two decades, Oki et al. first demonstrated a DFB grating based dye laser array and achieved digital spectroscopy without wavelength scanning.[99] Maeda et al. improved the DFB dye laser array and achieved high speed wavelength switching through acoustic-optic and thermal-optic effect.[97] Oki et al. demonstrated a flow cytometry chip combined with multiple DFB dye lasers, potentially for biological analysis and medical diagnosis.[103] Meanwhile, other types of optical cavity arrays, such as photonic crystal nanolaser arrays,[98] F-P cavity laser arrays[13] and microdisk laser arrays,[105] are developed for high-throughput bio/chemical sensing as well.

Although laser arrays made of DFB grating, photonic crystal, F-P cavities and micro-disks are easy to fabricate, cost-competitive, and compact, the structure and dimension of these optical cavities are fixed once the device is fabricated. Without introducing external effects, the flexibility in adjusting the cavity size is rather limited. In contrast, liquid microdroplets are easy to generate through either a nozzle sprayer[4] or microfluidic devices (T-junctions,[106] co-flowing,[107] and flow focusing[108]). A microdroplet has a nearly perfect spherical geometry through minimized surface tension, which facilitates to achieve a low lasing threshold. Additionally, a microdroplet inherently provides a liquid environment, which, with proper cavity design, is compatible with biological materials, such as cells, DNAs, and proteins and thus presents potential for

biosensing applications. Currently, microdroplet lasers supported on the superhydrophobic or superhydrophilic surfaces have been demonstrated by spraying[4] or two-phase solution mixing[75]. This type of microdroplet lasers is stationary, with droplets are randomly distributed on the substrate and present a large size distribution. It is challenging to develop controlled droplet laser arrays out of this platform. At the same time, microdroplets generated in the microfluidic devices have a highly monodispersed size distribution. However, each droplet is generated sequentially in the microfluidic channel, and thus the spatial arrangement of multiple droplets is challenging and limited by the fluidic channel geometry.

Considering the unique advantages of microdroplet lasers, here we demonstrate for the first time, to the best of our knowledge, an optofluidic droplet laser array on chip, using a silicon based micronozzle platform. A 2X2 droplet laser array is fabricated and studied in this work as a proof of concept. However, the device can be readily scaled up to a higher density laser array on a silicon chip through standard photolithography and soft lithography. Lasing property of single droplets from the droplet array has been investigated. The lasing threshold for the droplets with diameter varying from 115 μm to 475 μm is in the range of 0.63-2.02 μJ/mm^2. Due to the array arrangement of microdroplets, it is challenging to record the emission spectrum for each droplet in the array simultaneously using a spectrometer to analyze the lasing threshold. Therefore, we develop an image-based analysis method to measure the lasing threshold of all droplets in the array simultaneously. A comparison study shows that the threshold value obtained from the image-based analysis is highly consistent with the one obtained from spectrum-based analysis. The average lasing thresholds achieved by spectrum-based analysis and image-based analysis, respectively, are within 6.68% difference of each other. The accuracy of image-based lasing threshold analysis method can be further improved by increasing the

35

resolution of the camera. Additionally, the image-based analysis enables a cost-effective way to characterize laser performance by eliminating the use of high-resolution spectrometer, which is bulky and expensive. The optofluidic droplet laser array and image-based analysis method demonstrated in this work has contributed to the development of cost effective and integrated coherent light source on chip and compact devices for point-of-care applications.

3.2 Experimental setup and device fabrication

3.2.1 Design

In order to generate multiple droplets simultaneously on chip, a 2X2 micronozzle array and a set of branch-splitting microfluidic channels are designed, as shown in Fig. 3-1(a). Each nozzle is connected to its own microfluidic channel located at the backside of the silicon chip. The main channel splits into two equal branches with a symmetric design. Each of these two branches further splits into another two equal branches, at the end of which locates the micronozzle. The size of the nozzle through hole is 30 μm in diameter. The distance between two adjacent nozzles is 1 mm (center to center). The width of the backside main channel is 500 μm, which tapers down to 200 μm for all subsequent branch channels. The height of the backside channels and the depth of the nozzle holes are 150 μm respectively. Immersion oil (or a hydrophobic phase material) containing dye molecules is delivered to microfluidic channels through inlet when the micronozzle array is immersed in water (or a hydrophilic phase material). When a positive pressure is applied to microfluidic channels, the oil phase will emerge from individual nozzles and simultaneously form an array of oil droplets in water. Microdroplets having a refractive index (*e.g.*, immersion oil, n = 1.515) higher than that of surrounding liquid (water, n = 1.334) and a low absorption coefficient ($\alpha < 10^{-3}$ cm^{-1}) form optical microcavities that support high Q-factor (>10^6)[36, 37] whispering gallery modes (WGMs); light emitted from the gain material (*i.e.*, dye) is
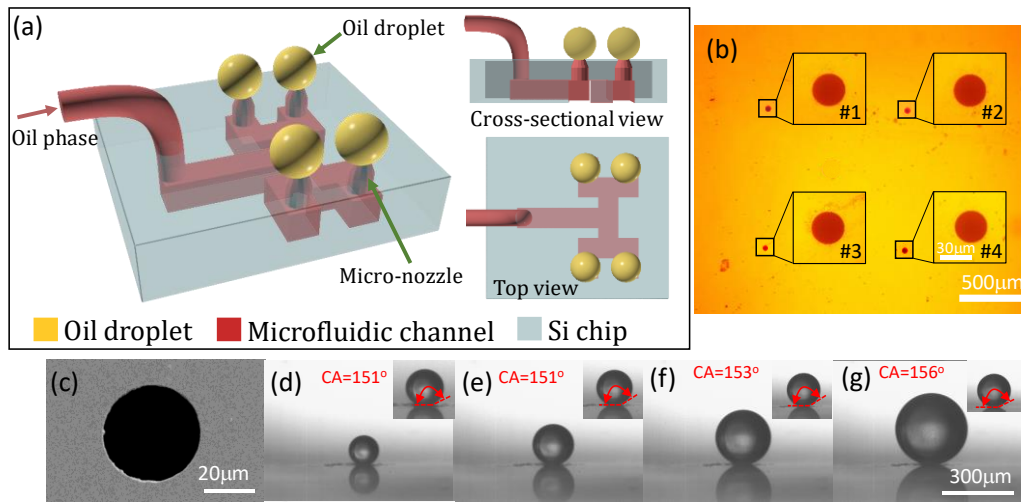
Figure 3-1 Si nozzle array and its droplet generation performance. (a) The schematic of droplet laser arrays on a silicon chip. The main channel splits into four equal branches to guide the fluid into the 2X2 micronozzles. (b) The optical microscope image of nozzle array with zoom-in view of each nozzle. (c) The SEM image shows the size of a nozzle is 30 μm in diameter. (d)-(g) Droplets of different sizes are generated on a nozzle. The droplet diameter is 126 μm, 175 μm, 233 μm, and 303 μm, respectively. The contact angle (CA) of all droplets is larger than 150°, which indicates the droplets have minimal contact with the substrate surface.

confined and amplified in the droplets by total internal reflection at the cavity surface and thus achieve lasing. When oil droplets reach a desired size, water flow is initiated to wash away the droplets, which allows the regeneration of new droplets. The symmetric design of the microfluidic channels helps to maintain the same pressure for every nozzle, so that the droplets generated on each nozzle have the same size. With proper control between the pressurized oil phase and water flow, the generation and regeneration of droplets with different sizes can be easily achieved.

3.2.2 Fabrication of Si nozzle devices

Through standard photolithography technique, the fabrication of micronozzle array device is outlined by three major steps, as shown in Fig. 3-2(a): nozzle through-hole etching from the top side, microfluidic channel etching from the bottom side, and anodic bonding the Si chip to a glass substrate. Bare Si samples (N/Ph<100>, 300±25 μm thick,

37
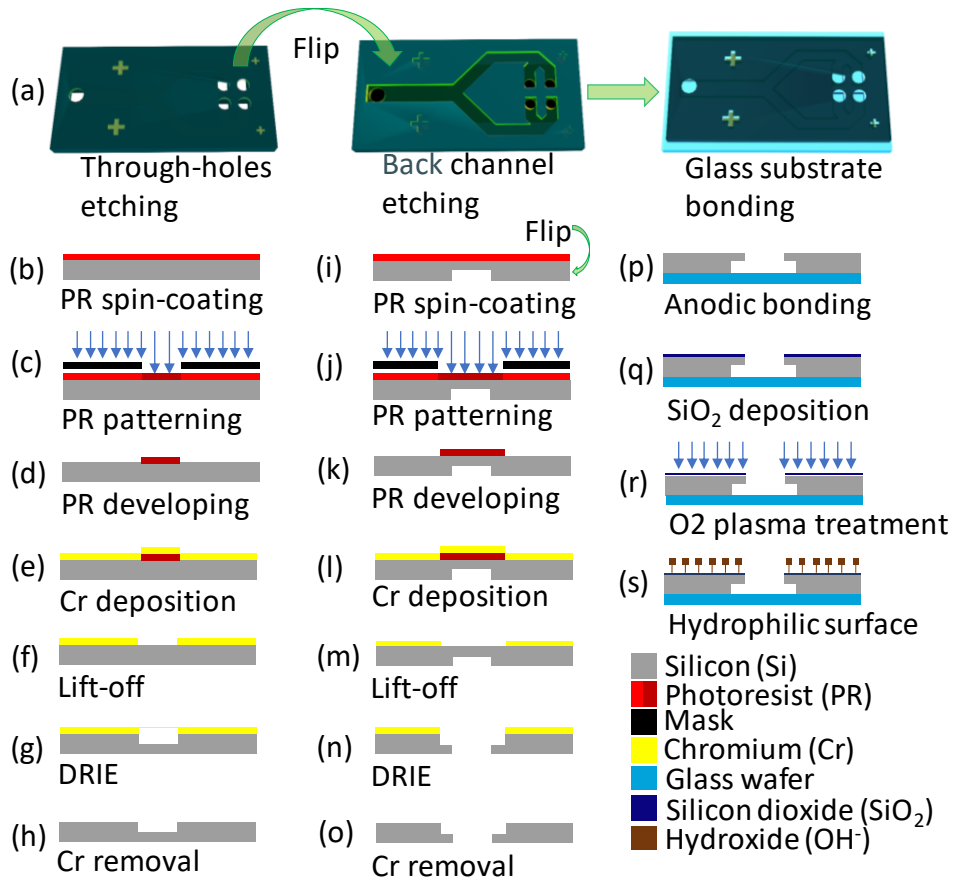
Figure 3-2 The fabrication process flow for micronozzle array.

double-side polished) are immersed in Piranha solution ($V_{surfuric\ acid}$:V_{H2O2}=3:1) for 15 min, rinsed by plenty of DI water and dried under N_2 flow. The cleaned Si samples are spun-coated with NR9 negative photoresist (Futurex) at 500 rpm for 30 s and 4000 rpm for 60 s, then baked at 150 °C for 60 s on a hot plate. The spun-coated Si samples are aligned with pre-designed mask and exposed to UV light at 20 mW/cm^2 power density for 9.5 s under a G-line aligner system (OAI model 800 backside mask aligner). After baked at 100 °C for 60 s and developed for 65 s with agitation, the patterned Si samples are ready for Chromium (Cr) metal mask deposition, which works as a hard mask for nozzle through-
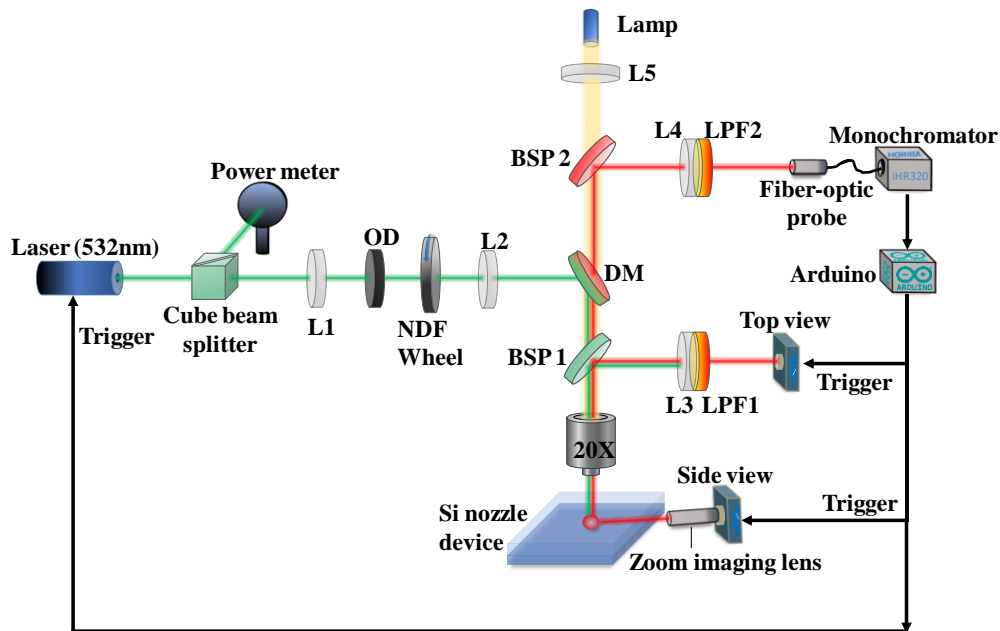
Figure 3-3 The experimental setup for droplet laser array testing. Laser (532nm): OPO laser, repetition rate: 2 Hz, pulse width: 5-7 ns, output wavelength: 532 nm. Cube beam splitter: T:R ratio of 50:50. L1, L2, L3, L4, L5 are lenses with focal length of 5 cm, 5 cm, 15 cm, 2.5 cm, and 7.5 cm, respectively. BSP1, BSP2: beam splitters with T:R ratio of 50:50, 10:90, respectively. OD: neutral density filter with a fixed OD of 1. NDF wheel: neutral density filter wheel with a continuous variable OD from 0 to 2. DM: dichroic mirror with a cut-off wavelength of 550 nm. LPF1, LPF2: long pass filters with cut-off wavelength of 550 nm, 600 nm, respectively. Zoom imaging lens: variable magnification of 1X-6X. Side view, top view are cameras for monitoring droplets.

hole etching. A 20 nm thick Cr layer is deposited on the patterned Si samples (AJA Ebeam evaporator) and the remaining photoresist covered by Cr is lifted off by dipping the Si samples in acetone for 5 min. The final Cr mask patterned Si samples are etched for 150 μm through deep reactive ion etching (DRIE). After removing the Cr mask, the fabrication of 2X2 micronozzle through-holes on the Si samples is finished. The step-by-step process flow is shown in Fig. 3-2(b)-(h). The optical microscope image of the 2X2 nozzle array is shown in Fig. 3-1(b), with a diameter of 30±3 μm. The SEM image of a fabricated nozzle is shown in Fig. 3-1(c). The backside channel etching is performed from the bottom side of

Si samples, as detailed in Fig. 3-2(i)-(o). After DRIE and Cr mask removal, the final etching depth of the backside channel is 150 μm. Finally, the Si nozzle array samples are bonded to glass wafers using a home-built anodic bonding system, as shown in Fig. 3-2(p). To improve the hydrophilicity of the Si nozzle surface, a 50 nm thick of SiO_2 is deposited on the top surface by Plasma Enhanced Chemical Vapor Deposition (PECVD), followed by plasma treatment (100 W, 30 s, O_2 20 sccm), as shown in Fig. 3-2(q)-(s). The microfluidic channel inlet is created on a PDMS that is bonded to the micronozzle device.

3.2.3 Optical setup and synchronization of optical systems

A typical confocal setup is used to excite the droplet array, as shown in Fig. 3-3. The excitation source is an OPO pulsed laser at a wavelength of 532 nm (repetition rate: 2 Hz, pulse width: 5-7 ns, pulse energy: 1 mJ per pulse). The pump power is first attenuated by a fixed neutral density filter (OD=1), then adjusted by a continuously variable neutral density filter. The power of the OPO laser per pulse is measured with a power meter in real time. The laser excitation beam spot size is around 10 mm^2. Thus, the overall power energy density during the lasing testing was from 0.72 $\mu J/mm^2$ to 11.64 $\mu J/mm^2$. The emission light is collected through a 20X objective lens and analysed by a monochromator (Horiba iHR320, spectral resolution of 0.2 nm). The top view and side view images of the droplet are captured by the top view and side view cameras (Genie Nano C800, Teledyne DALSA) in real time for droplet size measurement and image-based lasing threshold measurement.

In. order to capture the lasing images of the droplet under excitation, a home-built LabView program has been developed to synchronize the monochromator, cameras and OPO pulsed laser. First, the monochromator is chosen as the master that sends out commands/signals. Second, an Arduino programming board (Arduino Mega 2560) receives the commands from the monochromator and sends out the trigger signals to both top view and side view cameras and OPO pulsed laser, as shown in Fig. 3-3. Through

40

synchronization, each excitation pulse from the OPO laser can be accurately matched to its corresponding lasing emission spectrum and side-view and top-view images of the droplet.

3.2.4 Formation and regeneration of microdroplet lasers

Nile Red (Sigma-Aldrich) is chosen as the organic dye for our laser system. 500 μM Nile Red is dissolved in immersion oil (Sigma-Aldrich, n=1.515). To generate droplet laser arrays, a positive pressure applied by a high precision syringe pump (Harvard Apparatus, model 55-1144) pushes the immersion oil from the backside channel to emerge from Si micronozzles to form dye-doped oil droplets in the water environment. The droplet arrays are monitored in real-time by the top-view and side-view cameras. The droplet after generation can be studied continuously for a desired period of time, in contrast to the droplet laser on-the-flow in microfluidic channels. To regenerate droplet laser arrays, a water stream is initiated to wash away the droplets on the micronozzles and new droplets subsequently form under the positive backside channel pressure. The contact angles of droplets of different sizes, 126 μm, 175 μm, 233 μm, and 303 μm in diameter, generated by the micronozzle are characterized in Fig. 3-1(d)-(g). The contact angle of all the droplets is above 150°, which indicates a good Q factor of microdroplet cavities.

3.3 Results and discussion

First, the lasing threshold of individual droplets from the droplet laser array is investigated. One of the nozzles is centered under the excitation beam through the top view camera. For each pump pulse excitation, the top-view image, side-view image, and emission spectrum of the droplet are simultaneously acquired at 2 Hz. The generation and excitation of different sizes of droplets are shown in Fig. 3-4(a), in which the sizes of droplets 1-6 are 132 μm, 172 μm, 183 μm, 194 μm, 215 μm, and 284 μm, respectively. All droplets have strong lasing emission with pump densities much higher than their lasing thresholds. Their pump energy densities are 7.5 $\mu J/mm^2$, 11.3 $\mu J/mm^2$, 11.1 $\mu J/mm^2$, 8.4
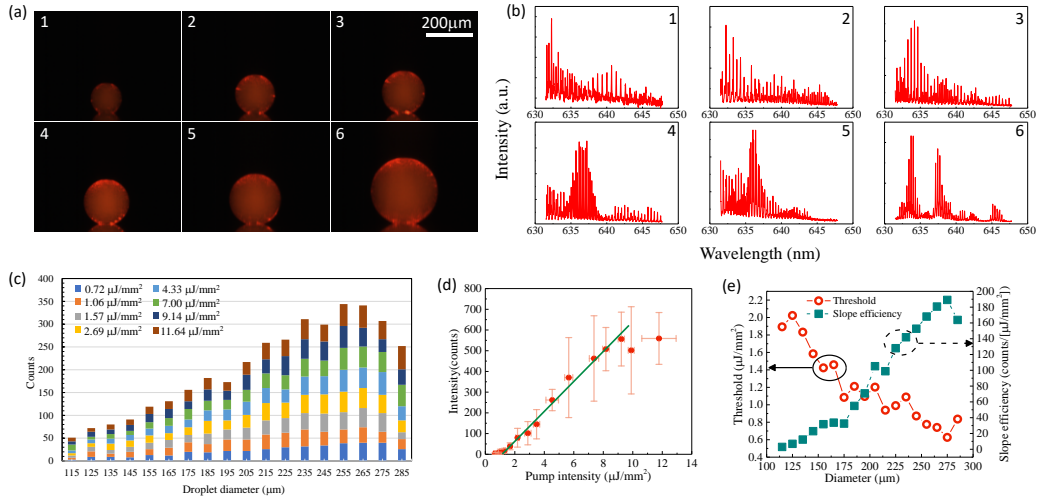
Figure 3-4 Lasing performance for droplets with different diameters. (a) shows the images of droplets 1-6 under excitation. Their diameters are 132 μm, 172 μm, 183 μm, 194 μm, 215 μm, 284 μm, respectively. Their pump energy densities are 7.5 μJ/mm², 11.3 μJ/mm², 11.1 μJ/mm², 8.4 μJ/mm², 12.0 μJ/mm², 10.7 μJ/mm², respectively. (b) shows the corresponding lasing spectra of droplets from 1-6 in (a). (c) The size distribution of droplets under different excitation pump intensity. (d) shows the relationship of lasing intensity vs pump intensity for 195-μm droplets. The estimated lasing threshold is around 1.09 μJ/mm². (e) shows threshold values and the slope efficiency for different size of droplets. The overall lasing threshold is in range of 0.63~2.02 μJ/mm².

μJ/mm², 12.0 μJ/mm², 10.7 μJ/mm², respectively. The corresponding emission spectra from each droplet are measured in Fig. 3-4(b). Additionally, the lasing emission can be clearly seen at the droplet circumference in the side-view images in Fig. 3-4(a), confirming the surface nature of the WGMs. Based on the free spectral range (FSR) of lasing emission for each droplet, the calculated sizes are 133 μm, 170 μm, 187 μm, 196 μm, 220 μm, 281 μm, respectively. FSR $\Delta\lambda = \lambda_L^2/\pi dm$, in which $\lambda_L = 640nm$, d is the diameter of droplets, m is the effective refractive index of the WGMs, $m \approx 1.515$. From the FSR measurements, the overall size measurement error from microscope images is around 1.4%. In addition to measuring individual droplet one at a time, synchronization of experimental setup allows us to characterize large number of droplets generated by the

nozzle continuously. At such continuous mode, the droplet grows to 285 μm in diameter before being released from the nozzle and is regenerated. During the growth period, the lasing emission from the droplet is acquired at 2 Hz. The excitation laser intensity is gradually increased from 0.72 μJ/mm² to 11.64 μJ/mm² for different rounds of generation process. The histogram of droplet size distribution under various excitation power densities is shown in Fig. 3-4(c). The lasing emission from a total number of 3650 droplets are characterized in a relatively short period of time. Droplet size is measured through a home-developed MATLAB program, which is detailed in supplementary *section 3.5.3*. Within each size group, the droplet lasing threshold is measured. Due to high-throughput generation, the average and standard deviation of lasing emission intensity for each droplet size can be easily obtained, which improves the measurement accuracy of the lasing threshold. Figure 3-4(d) shows the relationship between integrated lasing intensity and pump intensity for droplets of 195 μm in diameter (total number of droplets, N= 173). The lasing threshold extrapolated from the linear fitting is 1.09 μJ/mm². After applying the same process to other sizes of droplets, the relationship between lasing threshold and droplet size is presented in Fig. 3-4(e). The overall average lasing threshold is in the range of 0.63 - 2.02 μJ/mm². Based on the laser theory, the lasing threshold, $I_{pump(th)}$, is determined by the following equations.[76, 82, 109]

$$I_{th} = \frac{\gamma}{1-\gamma} \tag{3-1}$$

where γ is the fraction of gain molecules in the excited state at the threshold and is expressed by

$$\gamma = \frac{\sigma_a(\lambda_L)}{\sigma_e(\lambda_L)+\sigma_a(\lambda_L)}\left[1 + \frac{Q_{abs}}{Q_0}\right] \tag{3-2}$$

where $\sigma_e(\lambda_L)$ ($\sigma_a(\lambda_L)$) is the dye emission cross-section (dye absorption cross-section) at the lasing wavelength λ_L, Q_0 is the microdroplet empty-cavity quality factor, and $Q_{abs} =$

43

$2\pi m / \lambda_L n_t \sigma_a(\lambda_L)$ is the quality factor related to the dye absorption. n_t is the total concentration of the dye. If the empty-cavity quality factor Q_0 remains the same for all droplets, the lasing threshold should also remain the same for all droplets with different sizes. However, for our laser system, since the droplet is in contact with the Si nozzle surface, the contact area in relative to droplet size can affect the Q factor. For smaller droplets, the contact area between droplets and Si nozzle surface is relatively large comparing to the droplet, thus the Q factor is lower and lasing threshold is higher than that of the bigger droplets. Meanwhile, when droplets grow bigger in size, more dye molecules are located near the droplet surface and interact with the WGMs. Therefore, the output lasing intensity increases. As a result, with the increase of droplet size, the lasing threshold slope efficiency increases linearly and the lasing threshold decreases slightly as shown in
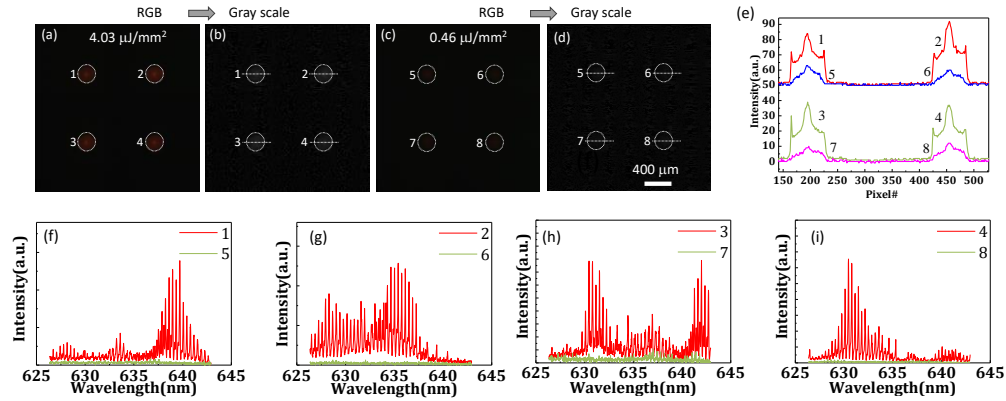
Figure 3-5 Droplet laser array lasing emission. (a) and (c) show 275-μm droplet array images excited under pump power density of 4.03 μJ/mm², 0.46 μJ/ mm², respectively. (b) and (d) show the gray-scale images of droplet array. The pixel intensity distributions of gray-scale droplet array images are shown in (e). The white dotted lines indicate where the pixels are taken from. (f)-(i) show the spectrum of each droplet under excitation.

Fig. 3-4(e).

We further investigate the lasing emission from the droplet laser array. Due to the 2X2 nozzle array design, the OPO laser beam is expanded to excite all four nozzles at the

same time. The top view camera is in use to monitor the droplet size because the side-view camera is not able to keep all four nozzles in focus at the same time. Fig. 3-5(a) and (c) are RGB images of the droplet array under excitation. The pump intensities are 4.03 µJ/mm^2 in Fig. 3-5(a) and 0.46 µJ/mm^2 in Fig. 3-5(c), which are above and below lasing threshold, respectively. After converting the RGB images of droplets into gray-scale images, as shown in Fig. 3-5(b) and (d), the pixel intensity profiles can be extracted. To examine the
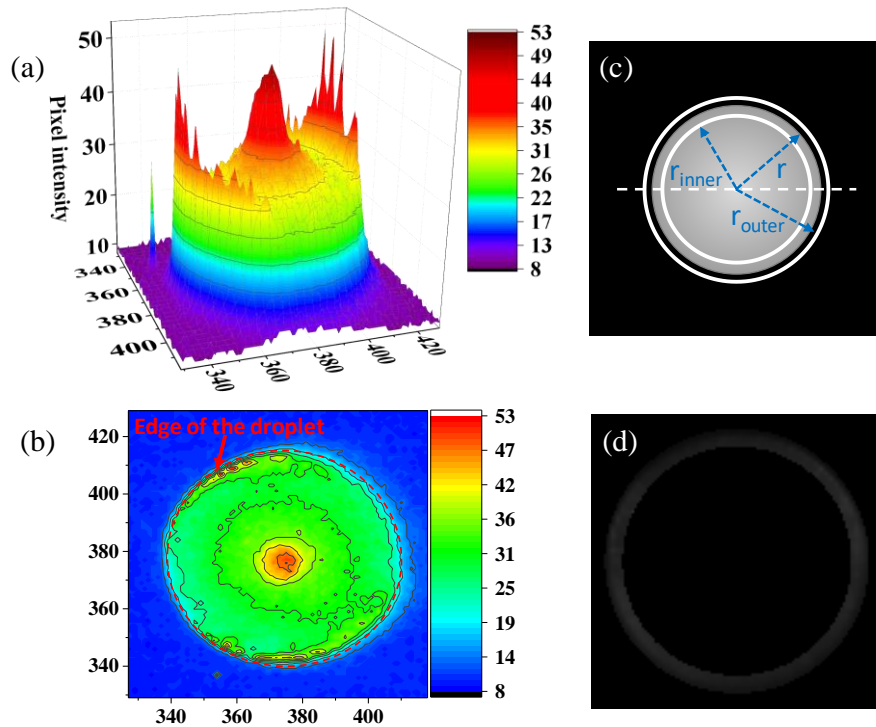
Figure 3-6 Image-based lasing threshold analysis method for droplet lasers. (a) The 3D surface and (b) contour plot for droplet pixel intensity distribution. (c) Only pixels within the ring area near the droplet edge is considered for image-based lasing threshold analysing method. r is the MATLAB-measured radius, rinner = r – 4 (pix), router = r + 3 (pix). (d) Only pixels that are within the ring area are left for further analysis.

light emission from the droplet, the pixel intensity along the straight dashed line which runs through the center of each droplet is plotted out in Fig. 3-5(e). The center and edge of a droplet are decided by our home-written MATLAB program (see ESI for detail). As shown

45

in the pixel intensity profiles, when the pump intensity is above the lasing threshold of 1.17 $\mu J/mm^2$, high-intensity pixels emerge near the surface on both sides of the droplet (red and light green curves in Fig. 3-5(e)); when the pump intensity is below the lasing threshold, no high-intensity pixels are observed (blue and magenta curves in Fig. 3-5(e)). This demonstrate that it is feasible to extract lasing information by utilizing the pixel intensity near the droplet surface. To confirm the results obtained by the camera pixel plot, the light emission from the droplets are concurrently measured by a high-resolution spectrometer. Figure 3-5(f)-(i) show the emission spectra from these four droplets that are excited above and below the lasing threshold. To note that, the lasing emission spectrum 5-8 in Fig. 3-5(f)-(i) showed very different emission signatures. This is mainly because different groups of WGMs had different lasing thresholds and 4.03 $\mu J/mm^2$ was well above their lasing thresholds. As a result, multiple groups of WGMs emerged and competed against each other. After a random selection process, the emission spectrum appeared to be different from one droplet to another, as well as from one pulse to another pulse. Furthermore, since the traditional way of measuring the lasing threshold is to take multiple emission spectra of the sample under different pump intensities and then linearly fit the relationship between integrated lasing intensity and pump intensity to estimate the lasing threshold, a spectrometer/monochromator is necessary for the experiment despite of their high cost. In order to develop an easy and low-cost method to measure the lasing threshold without any spectrometer involved, we decided to use cameras to achieve this goal, which are generally cheaper than spectrometers. We named this method as image-based lasing threshold analysing method. In our work, the images of all excited droplets are processed by our home-built MATLAB program, then the relationship between integrated lasing pixel intensity around the edges of droplets and pump intensity are studied. Due the resolution of the camera (600X800), each pixel stands for 4 μm in length or in width. In order to
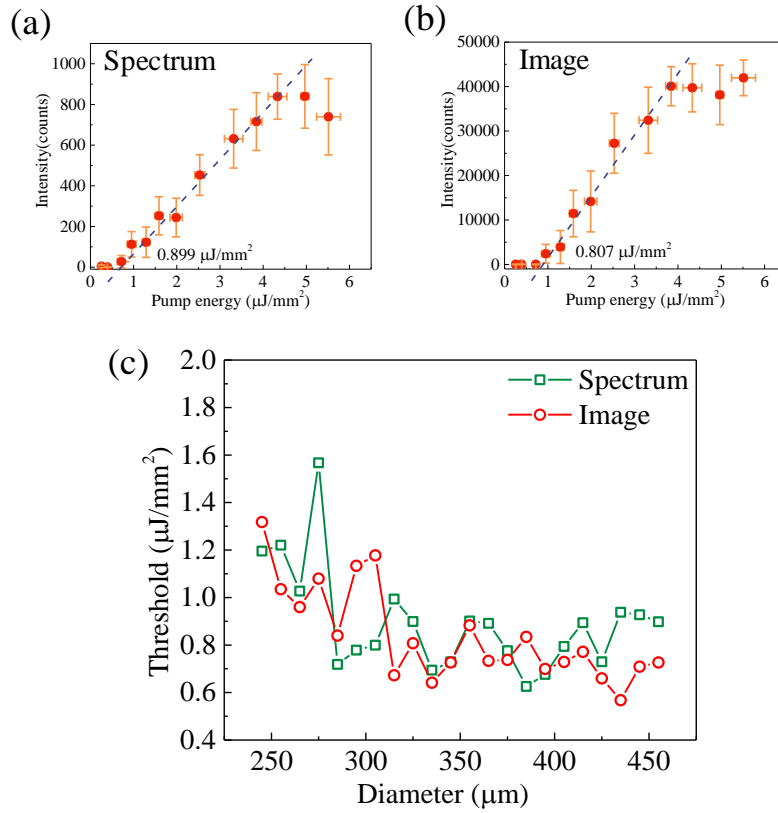
Figure 3-7 Comparison between spectrum-based and image-based lasing threshold analysis methods. (a) The relationship between integrated lasing intensity from emission spectrum and pump energy for 325-μm droplets. Through linear fitting the estimated threshold is 0.889 μJ/mm^2. (b) The relationship between integrated pixel intensity from the equator part of droplet image and pump energy for 325-μm droplets. Through linear fitting the estimated threshold is 0.807 μJ/mm^2. (c) The lasing thresholds for droplets with different sizes. Curve "Spectrum" is calculated from spectrum-base method, curve "Image" is calculated from image-based method

determine the cut-off value of pixel intensity between fluorescent emission and lasing emission, the pixel intensity distribution of the lasing droplet is plotted out in Fig. 3-6(a) and (b). Along the droplet edge, some pixels present high intensities comparing to the rest pixels, which indicates that those high-intensity pixels are contributing to the lasing emission and the rest pixels present fluorescent emission. The average pixel intensity of fluorescent emission pixels is 21 along the droplet edge, as shown in Fig. 3-6(b), thus this

47

is set as the cut-off value to differentiate pixels for lasing and pixels for fluorescence. Besides, since lasing emission is coming from WGMs and they only happen near the inner surface of the droplet, so only a ring area is chosen for the lasing analysis. The radius of the outer ring is r + 3 pixels (r is the MATLAB-measured droplet radius), the radius of the inner ring is r − 4 pixels, which is enough to include all the possible pixels for lasing emission. After applying the ring area to the droplet's gray-scale image, the actual area that is considered for lasing analysis is shown in Fig. 3-6(d). During the process of image-based lasing threshold analysing method, all the pixels within the ring area are subtracted by the cut-off pixel value, then all the positive values are integrated as pixel lasing intensities. The droplet size distribution is shown in Fig. S2, from 245 μm to 455 μm with a total number range of 40-160. Within each group, droplets are tested under different pump intensities, from 0.31 μJ/mm^2 to 5.58 μJ/mm^2. The relationship between the integrated lasing intensity (from spectrum-based method) and pump intensity is presented in Fig. 3-7(a) for 325-μm droplets. The estimated lasing threshold through linear fitting is around 0.899 μJ/mm^2. In comparison, the relationship between the integrated lasing pixel intensity (from image-based method) and pump intensity is presented in Fig. 3-7(b) for 325-μm droplets. The estimated lasing threshold through linear fitting is around 0.807 μJ/mm^2. After applying both spectrum-based method and image-based method to all the droplets, the threshold vs diameter relationship is presented in Fig. 3-7(c). Curve "Spectrum" shows the lasing thresholds that come from the spectrum-based method with an average threshold of 0.894±0.215 μJ/mm^2, curve "Image" shows the lasing thresholds that come from the image-based method with an average threshold of 0.838±0.197 μJ/mm^2. The image-based method produces an average lasing threshold that is within 6.68% difference of the average lasing threshold from the spectrum-based method, which shows a good repeatability and reliability of the image-based method for lasing threshold measurements. We admit that the

current image-based method is limited by the resolution of the camera. If the resolution is further increased the analysis for the droplet edges will be more accurate, and even smaller ring thickness is needed for pixel intensity integration.

3.4 Conclusion

In summary, we have demonstrated a droplet-based laser array and characterized the lasing threshold for droplets with size of 115 μm - 475 μm is from 0.63 - 2.02 μJ/mm^2. An image-based lasing threshold analysing method has been developed to characterize the droplet laser array in a fast and cost-effective manner. The 2x2 droplet laser array can be readily scaled up to a NxM nozzle array (where N and M are integers), which can be a useful platform for creating integrated coherent light source on chip and high-throughput intra-cavity biosensing using the lasing emission from individual droplets in the array. In terms of point-of-care applications, the bulky and costly OPO pulse laser can be easily replaced by a compact semiconductor nanosecond pulse laser to meet the needs of integration. By changing the backside channel configuration and introducing independent control on subset of nozzles, different gain media covering different emission spectral region can be achieved with this laser system, which enables the applications that require multiple operating channels, such as high speed wavelength switching light sources and on-chip spectroscopic analysis.

3.5 Supplementary

3.5.1 Anodic bonding system

As shown in Fig. 3-8, Si sample is in contact with anode, glass substrate is in contact with cathode. The glass mask is used as insulator to separate the hot plate and 5-pound weight from the electrodes. The 5-pound weight is put on top of the anodic bonding system to provide pressure for Si-glass wafer bonding. Set the voltage power supply at 900 V, start the hot plate and increase the temperature 50 °C every 5 min, then keep the temperature at 350 °C for 30 min. After bonding, let the system cool for 30 min and take off the bonded Si nozzle sample.
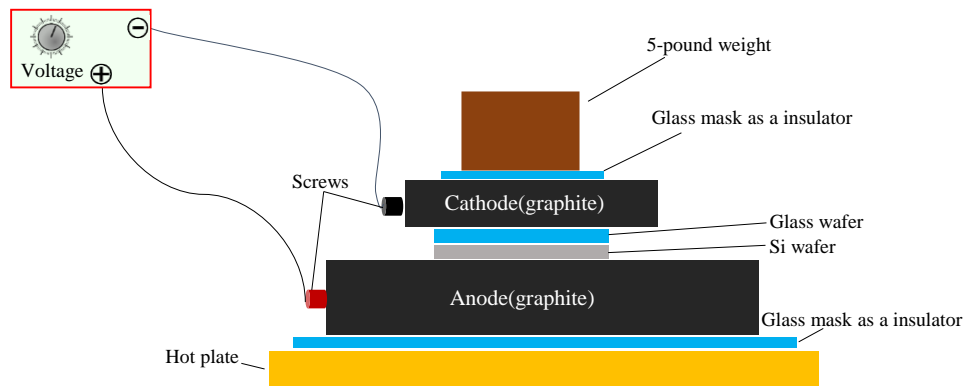
Figure 3-8 Home-built anodic bonding system

3.5.2 Soft lithography of PDMS layer fabrication

First, the fabrication of SU-8 mold. Si wafer is used as a support substrate for SU-8 mold. The Si wafer is cleaned in in Piranha solution ($V_{surfuric\ acid} : V_{H_2O_2} = 3:1$) for 15 min, rinsed with plenty of DI water and dried under N_2 flow. The SU-8 2100 negative photoresist (MicroChem) is spun at 1000 rpm for 30 s and pre-baked at 65 °C for 7 min, soft-baked at 95 °C for 60 min. Then SU-8 sample is aligned with pre-designed mask and exposed with a 20 mW/cm^2 power density for 16 s under a G-line system. After exposure, SU-8 sample is baked again at 95 °C for 20 min, followed by 20-min development with
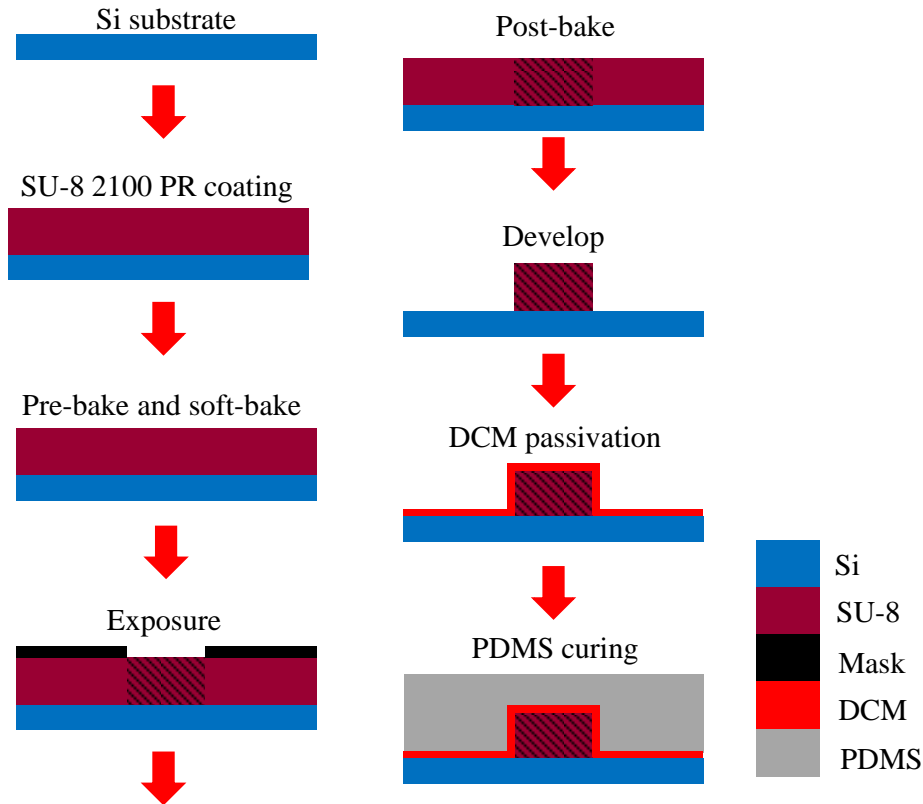
Figure 3-9 The process flow of fabrication of SU-8 mold and PDMS top channel

220-rpm agitation. At last, the SU-8 sample is cleaned with IPA rinse and dried under N_2 flow. To improve the PMDS peeling-off process, the SU-8 mold is kept in a vacuum chamber and exposed to DCM vapor (50μL drop) for 2 h.

Second, the PDMS layer preparation. PDMS mixture is prepared by mixing SYLGARD® 184 silicone elastomer (base) with SYLGARD® 184 silicone curing agent in 10:1 ratio by weight. The mixture is degassed in a vacuum chamber for 30 min. The degassed PDMS mixture is poured onto SU-8 2100 mold. Let the PDMS mixture to spread out for 10 min so that the SU-8 2100 mold is evenly covered by the PDMS mixture. The PDMS is cured at 80 °C for 2 h and peeled off from the SU-8 mold. The final thickness of PDMS is around 2 mm. The process flow is shown in Fig. 3-9.

3.5.3 Image processing for droplet size measurement

As shown in Fig. 3-10, the original RGB image is directly captured by the camera. Through our home-developed Matlab program, first, the RGB image is converted into gray scale image. Second, gray scale image is normalized to the scale of [1, 255] (minimal value corresponds to 1, maximal value corresponds to 255) to strengthen the contrast between droplet area and background area. Third, the normalized gray scale image is exported into ImageJ to perform the edge detection process. Fourth, after edge detection, a threshold is set to remove all the pixels that are below the threshold value in the background to further strengthen the contrast between droplet edge and background noise. Fifth, through a Matlab built-in function "edge", the edge of the droplet is detected and image is converted into a binary image. Sixth, inner area of the edge detected binary image is filled, and the
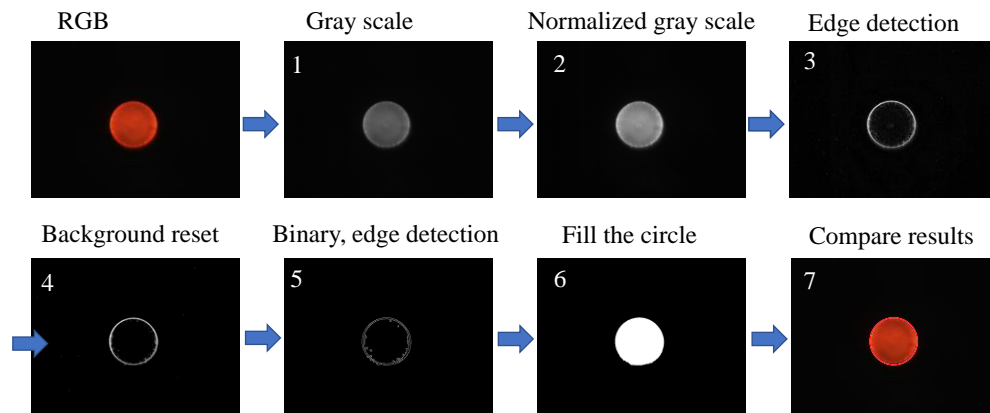
Figure 3-10 The process flow of droplet size measurement for the home-built MATLAB program.

logic value changes from "0" to "1". Seventh, for a binary image the Matlab built-in function "regionprops" is applied to find the droplet with center location and radius. Then the Matlab-found circle and original RGB image are plotted together for comparison. The radius found in step 7 is used as the droplet size.

3.5.4 Droplet size distribution of droplets with image-based method
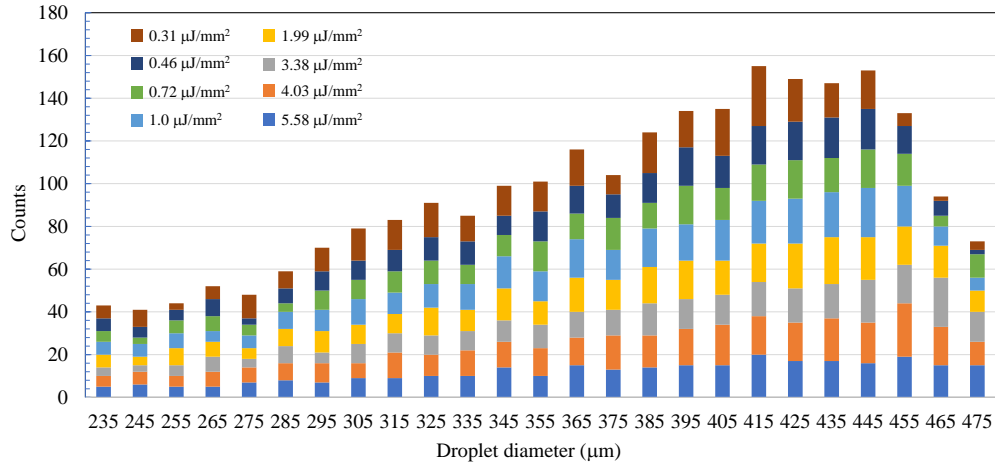
Figure 3-11 The size distribution of droplets under different excitation pump intensity

Chapter 4

Optofluidic Lasers with Monolayer Gain at the Liquid-Liquid Interface

In this chapter, we report optofluidic lasers with a monolayer gain material that self-assembles at the two-phase liquid-liquid interface. The self-assembly process deterministically introduces the gain at the surface of a microdroplet optical cavity, where the lasing mode has maximal interaction with the gain medium. A complete monolayer gain can be achieved in this surface-gain geometry, giving a surface density on the order of 10^{14} cm^{-2}, which proves to be difficult, if not possible, to achieve in the monolayer gain created at the solid-liquid interface via the surface immobilization method. We demonstrated that the lasing characteristics are of drastic difference between the gain material that is confined to the liquid-liquid interface and that is homogenously distributed in the bulk liquid solution. Our study reveals the unique capabilities of the surface-gain geometry optofluidic laser, which can be developed into a novel sensing platform to study biophysical and biochemical processes at the molecular level and has vast applications in biomedical diagnostics.

4.1 Introduction

Optofluidic lasers, which integrate micro/nanofluidics, optical micro-cavity, and gain medium in the liquid environment[80, 81, 110], have become an emerging technology in recent years. Compared to gas- and solid-state lasers, the optofluidic laser is unique in its aqueous environment compatibility and adaptive nature of liquids. Therefore, it possesses distinct advantages for applications in bioanalysis and bioimaging[11, 80-82, 111, 112], and for building novel on-chip tunable active photonic devices[8, 30, 47] (such as coherent light

sources, bio-controlled lasers, and light harvesting devices, etc.). In a typical optofluidic laser configuration, the gain material (e.g., organic dyes[8, 15, 24, 30, 82, 113, 114], quantum dots[22, 115], fluorescent proteins[11, 77], luciferins[116], etc.) is homogenously distributed in the entire bulk liquid solution. Although such a gain configuration is simple to implement, the interaction between lasing mode and gain material may not be optimal, which results in poor lasing efficiency and compromised lasing performance. For example, in ring resonators,[80, 106, 117-120] certain types of DFBs,[84] and photonic crystals,[92] the lasing modes can interact only with those gain molecules (i.e., a few percent) that are close to the cavity surface through the evanescent field. The rest of gain molecules in the bulk solution does not participate in lasing, but contributes significantly to undesirable fluorescence background. To address this problem, surface-gain geometry optofluidic laser has been studied, where a layer of gain molecules are attached to the surface (e.g., silicon dioxide) of a ring resonator via chemical surface immobilization.[76] Although lasing has been successfully achieved, the intrinsic limitation of a liquid-solid interface makes it challenging, if not possible, to achieve a complete monolayer of gain at the surface. The surface density of the sub-monolayer gain materials obtained is strongly dependent on the surface chemistry and immobilization protocols, which are known to cause large variations in molecule surface density and orientation.

Here, we demonstrated an optofluidic microdroplet laser with a monolayer gain material that self-assembles at the two-phase liquid-liquid (oil/water) interface. The self-assembly process deterministically and accurately introduces the gain at the surface of a droplet optical cavity, where the whispering gallery modes (WGMs) have maximal interaction with the gain medium. Compared to the surface immobilization method on a solid substrate, our method does not require time-consuming surface immobilization steps and is highly repeatable in monolayer laser gain formation. Additionally, the surface gain

55
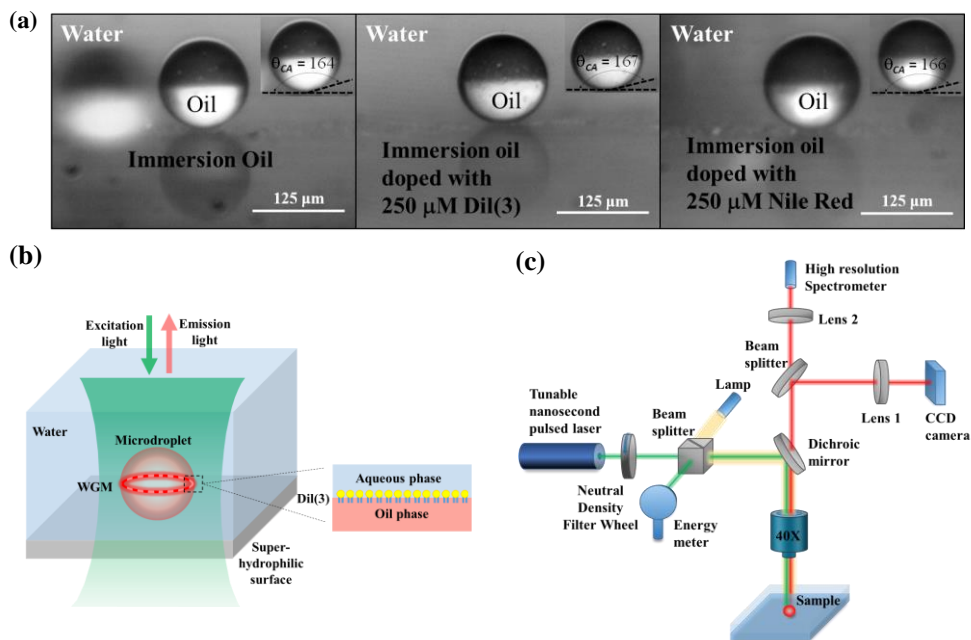
Figure 4-1 The morphology of droplets and the schematics for lasing testing setup. (a) Contact angle characterization of super-hydrophilic surface. The contact angle of oil droplet, DiI(3)-doped oil droplet, and Nile Red-doped oil droplet is 164°, 167°, and 166°, respectively. (b) Schematic illustration of the optofluidic laser with monolayer gain at the liquid-liquid interface. Microdroplets of oil phase are generated by a microfluidic T-junction and subsequently released into the aqueous phase. A super-hydrophilic surface was used to support the microdroplets to allow them being individually probed by the pump laser. Amphiphilic dye DiI(3) was used as the gain material. WGM: whispering gallery mode. Inset: Illustration of a monolayer of DiI(3) self-assembled at the oil/water interface. (c) Experimental setup for lasing characterization. Microdroplet size was measured by a CCD camera. Lasing emission from the droplet was measured by a spectrometer

formed at the two-phase liquid-liquid interface offers unprecedented capability to control, modify, program, and engineer the gain medium at the molecular level in an optofluidic laser, thus allowing the laser to be dynamically reconfigured in the most efficient way. In turn, the lasing emission generated in such surface-gain configuration can be conveniently modulated by introducing biological molecules and small chemicals in the aqueous phase to build ultrasensitive intra-cavity sensors. Furthermore, microdroplet naturally serves as a high-Q optical resonator due to its self-organized spherical shape formed by the surface

tension and its smooth interface between two-phase fluids (i.e., liquid-air interface or liquid-liquid interface). Therefore, microdroplets are very attractive in the development of ultralow-threshold lasers.[4, 28-30]

In this work, we used a surfactant dye DiI(3) as the gain material to demonstrate the concept of the surface-gain all-liquid optofluidic laser. When dissolved in oil droplets surrounded by an aqueous phase, DiI(3) diffuses to the droplet surface and self-assembles into a monolayer at the liquid-liquid interface due to its amphiphilic structure (i.e., hydrophilic chromophore and hydrophobic side chains).[75, 121, 122] At the right concentration, all gain molecules are located at the oil/water interface, and consequently, there is no free dye in the droplet bulk solution. The WGMs supported by the oil droplets interact with the gain molecules and provide the optical feedback for lasing. We demonstrated lasing from individual oil microdroplets supported by a monolayer of gain at the liquid-liquid interface. To confirm the lasing is indeed from the surface-gain, a non-surfactant dye, Nile Red, is used to generate lasing under otherwise the same experimental conditions. Drastic differences have been observed between the gain material that is confined to the liquid-liquid interface and that is homogenously distributed in the liquid solution.

4.2 Experimental design

DiI(3) (1,1'-Dioctadecyl-3,3,3',3'-tetramethylindocarbocyanine perchlorate, Sigma-Aldrich) and Nile Red (Sigma-Aldrich) are dissolved in immersion oil (refractive index = 1.515, Sigma-Aldrich) respectively to the desired concentration. Dye-doped oil microdroplets are generated using a microfluidic T-junction (see details in the supplementary, *section 4.5.2*). The droplets are subsequently released into a flow cell filled with DI water (refractive index = 1.334). The bottom surface of the flow cell is super-hydrophilic, prepared by electrodeposition of nickel cobalt hydroxide with hierarchical micro/nano structures on a fluorine doped tin oxide (FTO) glass (see details in the
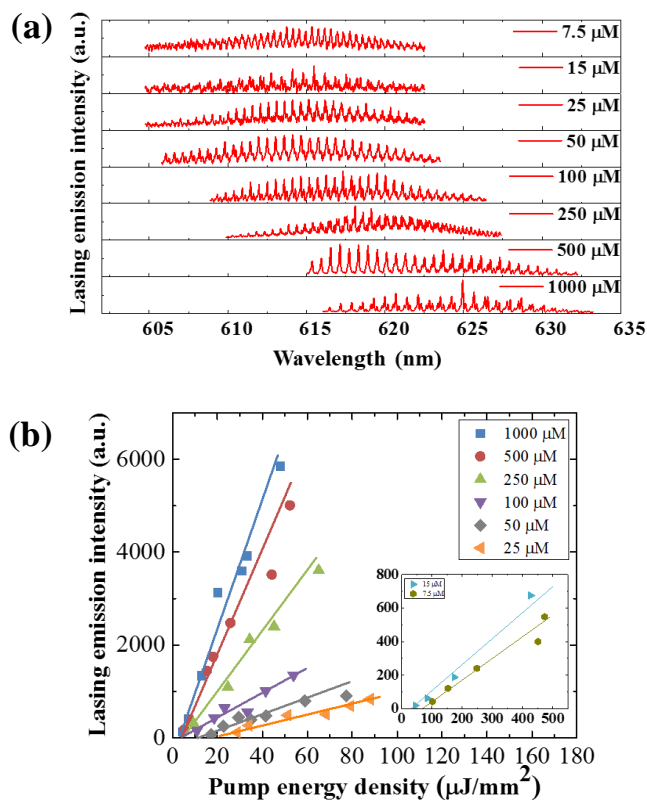
Figure 4-2 Lasing characterization of Dil(3) oil droplets under different concentrations. (a) Lasing spectra of microdroplets with different concentrations of Dil(3) (from 7.5 μM to 1 mM), pumped at well-above the threshold. Excitation wavelength: 532 nm. (b) Lasing threshold curves. The threshold of Dil(3) microdroplet is 70 μJ/mm^2 (7.5 μM), 33 μJ/mm^2 (15 μM), 20 μJ/mm^2 (25 μM), 11 μJ/mm^2 (50 μM), 5 μJ/mm^2 (100 μM), 5 μJ/mm^2 (250 μM), 4 μJ/mm^2 (500 μM), and 3 μJ/mm^2 (1 mM), respectively.

supplementary, *section 4.5.1*). Contact angle measurement on the super-hydrophilic surface is presented in Fig. 4-1(a), which shows oil droplets and dye-doped oil. droplets consistently have a contact angle of above 164°, indicating the superoleophobic nature of the surface under water. The microdroplets on the super-hydrophilic surface thus form a nearly perfect spherical resonator with good refractive index contrast to maintain a Q-factor (>10^3). As shown in Fig. 4-1(b), the microdroplet can be probed individually by the

pump laser light and the lasing emission can be continuously monitored and studied using this technique.

The experimental setup for characterization of lasing emission is illustrated in Fig. 4-1(c). The microdroplet was excited with a pulsed optical parametric oscillator (OPO) laser (repetition rate: 20 Hz, pulse width: 5 ns, wavelength: 532 nm, Continuum). The energy of the pump laser is adjusted with a tunable neutral density filter wheel and monitored by an energy meter (FieldMaxII, Coherent). The pump laser beam is reflected into flow cell by a dichroic mirror (cutoff wavelength 567 nm, long pass) and focused by a microscope objective (40x, NA = 0.6) to excite the droplets. Through the same objective lens, the emission from the droplet was collected and transmitted through the dichroic mirror and split with a 90/10 beam splitter. One path of the light was collected by a multimode fiber probe and sent to a high-resolution spectrometer (iHR320, Horiba). The other light path went to a CCD camera for imaging and droplet size characterization.

4.3 Results and discussion

To study the lasing capability and performance of the microdroplet laser with a monolayer gain at the liquid-liquid interface, various concentrations (7.5 µM - 1 mM) of DiI(3) oil solutions are used to generate the microdroplets. Those droplets with a size of 126 ± 11 µm in diameter are selected for experiment. An excitation wavelength of 532 nm was used in all experiments. The lasing emission spectra of droplets of different DiI(3) concentrations are shown in Fig. 4-2(a), which are pumped at well-above the threshold. Multiple lasing peaks corresponding to the WGMs with well-defined free spectral range is clearly observed. The lasing spectrum centers around 624 nm when DiI(3) concentration is 1 mM and gradually moves towards the shorter wavelength side of the spectrum when dye concentration is reduced. The integrated lasing intensity over the entire lasing spectrum
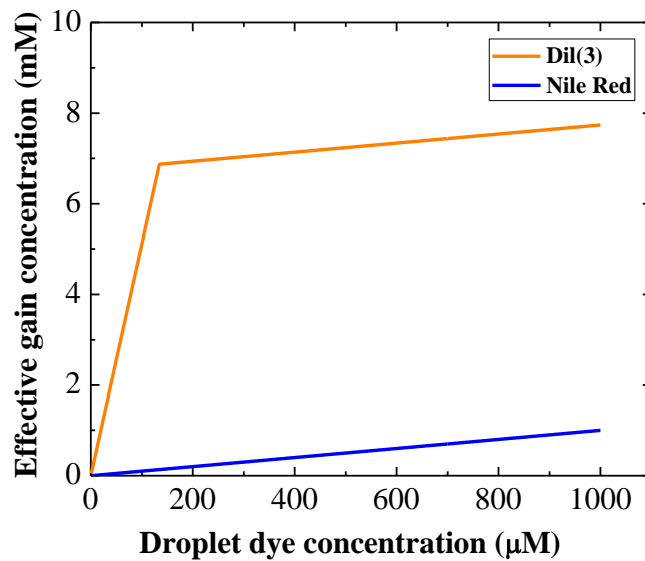
Figure 4-3 Relation between effective gain concentration and droplet bulk dye concentration for DiI(3) lasers and Nile Red lasers

(605 - 632 nm) as a function of the pump energy density is plotted in Fig. 4-2(b) for each of the dye concentration shown in Fig. 4-2(a).

In order to confirm the lasing emission in DiI(3) microdroplets is indeed from the monolayer of DiI(3) residing at the oil/water interface, we performed the control experiment using Nile Red as the gain material at otherwise the same experimental conditions. Nile Red is a commonly used gain material in dye lasers. Once dissolved in solution, Nile Red molecules are homogenously distributed in the microdroplet. In contrast, DiI(3) molecules are preferably diffuse to the oil/water interface and form a monolayer through self-assembly, due to their amphiphilic molecular structure. After DiI(3) molecules saturate the droplet surface, any additional molecules left in the solution will then be homogenously distributed in the entire volume of the droplet. Due to this key difference in spatial distribution between these two dyes in the microdroplet, the effective gain concentration, as defined by the dye concentration experienced by the WGMs (i.e., total

concentration of the dye that interacts with the WGMs), is drastically different for DiI(3) lasers and Nile Red lasers for a given concentration of dye solution used to generate the droplets. To quantitatively compare the effective gain concentration, theoretical calculation is performed for two dyes respectively and its dependence on the concentration of dye solution used to generate the droplets is shown in Fig. 4-3. For Nile Red microdroplet laser, as well as the majority of other optofluidic dye lasers, the effective gain concentration is equal to the dye solution concentration used to generate the droplets (i.e., bulk solution concentration in the droplet). However, for DiI(3) microdroplet laser the effective gain concentration is much higher than the dye solution concentration used to generate the droplets because dye molecules are favorably accumulated at the surface. The turning point in DiI(3) curve shown in Fig. 4-3 occurs at the critical concentration, where the number of DiI(3) molecules in the bulk solution is just enough to form a monolayer gain at the droplet surface and there is no free dye molecules left in the solution. The details on the analysis of surface accumulation effect on gain molecules is documented in the supplementary, *section 4.5.4*. Since effective gain concentration is equivalent to the number of dye molecules that are capable of participation in lasing, surface-gain geometry laser is intrinsically more efficient and advantageous compared to conventional optofluidic dye lasers. Lasing emission spectra and threshold curves for different dye concentrations are measured for Nile Red microdroplet laser, as shown in Fig. 4-6(a) (see details in the supplementary, *section 4.5.3*). To compare the surface-gain and bulk-gain configuration in optofluidic lasers, lasing threshold values of DiI(3) and Nile Red lasers at different droplet dye concentrations are plotted in Fig. 4-4(a). When dye concentration is reduced, Nile Red lasing threshold increases almost linearly in the logarithmic scale. However, due to the surface accumulation effect, lasing threshold stays almost unchanged when concentration is above the critical concentration, where a complete monolayer gain is formed at the droplet

(a)

(b)
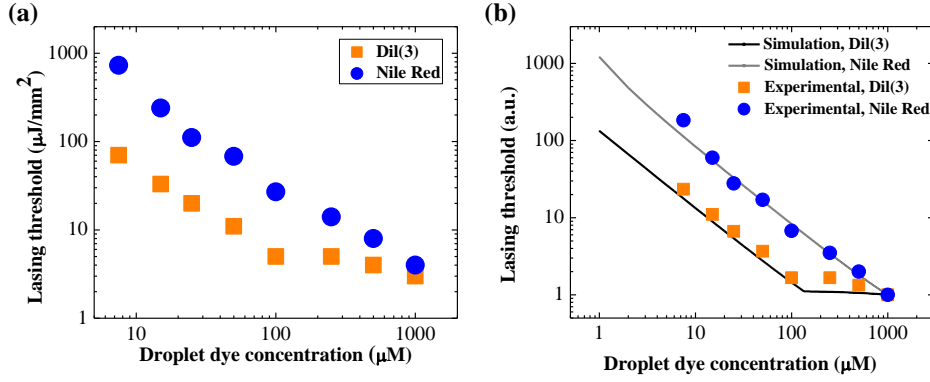
Figure 4-4 Lasing threshold for DiI(3) and Nile Red microdroplets and their dependence on the microdroplet dye concentration. (a) Experimental results. (b) Simulation results of normalized lasing threshold. Droplet cavity Q-factor of 5×10^3 is used in the simulation.

interface. When dye concentration is below the critical concentration, sub-monolayer of gain material is located at the droplet interface. Lasing can still be sustained in this region. However, lasing threshold increases quickly with decreased dye concentration, similar to the one observed in bulk-geometry optofluidic lasers.

To further understand the lasing characteristics between surface-gain and bulk-gain configuration in optofluidic lasers, theoretical analysis is performed on two types of lasers (see details in the supplementary, *section 4.5.4*). The lasing threshold, I_{th} is determined by[76, 82] Eqn 4-2 to Eqn 4-4. Dye emission cross-section and absorption cross-section are measured experimentally. Using experimentally measured data (see details in the supplementary, *section 4.5.6*), we calculate the DiI(3) emission cross-section at lasing wavelength of λ_L, DiI(3) = 618 nm to be $\sigma_e(\lambda_{L,DiI(3)}) = 7.98 \times 10^{-17}$ cm^2 and the Nile Red emission cross-section at lasing wavelength of λ_L, Nile Red = 635 nm to be $\sigma_e(\lambda_{L,Nile\ Red})$ = 1.46×10^{-16} cm^2. The absorption cross-section of DiI(3) and Nile Red at lasing wavelength region are extrapolated from their respective absorption spectrum, from which $\sigma_a(\lambda_{L,DiI(3)}) = 1 \times 10^{-21}$ cm^2 and $\sigma_a(\lambda_{L,Nile\ Red}) = 1.2 \times 10^{-20}$ cm^2 are obtained. Since direct

measurement of empty-cavity quality factor Q_0 is challenging in microdroplets, Q_0 values in the range of 10^3 to 10^5 are scanned in the simulation and its results on the threshold dependence on droplet dye bulk concentration for Dil(3) and Nile Red are compared to the experimental results to determine the empty-cavity Q-factor of our droplet lasers. From the results shown in Fig. 4-4(b), Q_0 is estimated to be around 5×10^3. It is worth noting that there is a unique turning point in the lasing threshold-concentration curve, as demonstrated in Fig. 4-4, in the surface-gain type of optofluidic laser formed at the two-phase liquid-liquid interface. This turning point corresponds to the critical concentration discussed previously, where a complete monolayer is self-assembled at the interface, which in turn is determined by the packing geometry (i.e., molecular spacing) of the gain molecules. Therefore, by mapping out the turning point in the threshold-concentration curve, the optofluidic laser platform demonstrated here could provide a convenient method to characterize molecular spacing. By linear fitting of the measurement data in the region below and above the critical concentration in Fig. 4-4(a), the critical concentration is estimated to be 122 μM, which yields a molecular spacing of 8 Å. This number is comparable to the molecular spacing of phospholipid molecules in liposome and lipid bilayer structures reported by other works.[119, 123]

4.4 Conclusion

In summary, we have developed an optofluidic droplet laser with surface-gain precisely located at the two-phase liquid-liquid interface. Lasing emission from monolayer gain and sub-monolayer gain have been achieved. The unique surface-gain geometry enables all gain material participate lasing, and thus greatly increases laser efficiency compared to the conventional optofluidic laser where gain material is homogenously distributed in the entire laser cavity. We have further demonstrated that lasing threshold in a surface-gain type of optofluidic laser is very sensitive to the molecular spacing and

packing geometry at the interface. Our technology could be potentially useful in studying phospholipids surface density and molecular orientation, and small molecule interaction dynamics within the cell membrane, all of which currently require the use of advanced technologies such as nuclear magnetic resonance (NMR), atomic force microscopy (AFM), and fluorescence microscopy.

4.5 Supplementary

4.5.1 Super-hydrophilic surface formation by electrodeposition

The inherent wetting nature of a surface is dictated by its surface free energy and can be further amplified by an increase in surface roughness.[124] Surface wettability is typically characterized by the water contact angle (WCA) on a surface. For example, transition metal hydroxides[125] and oxides such as $Ni(OH)_2$, $Co(OH)_2$, NiO, Co_3O_4, etc. are inherently hydrophilic (WCA < 90°) in nature. Introducing hierarchical micro/nano roughness further amplifies the hydrophilicity leading to the extreme wetting state of superhydrophilicity (WCA < 5°). The extremely high water affinity of such a surface can be utilized to achieve a corresponding underwater superoleophobic state,[126] i.e. the state of extreme repellence of a surface towards oil when in an aqueous medium. When immersed in water, the hierarchical structures of the super-hydrophilic surface are entirely infiltrated
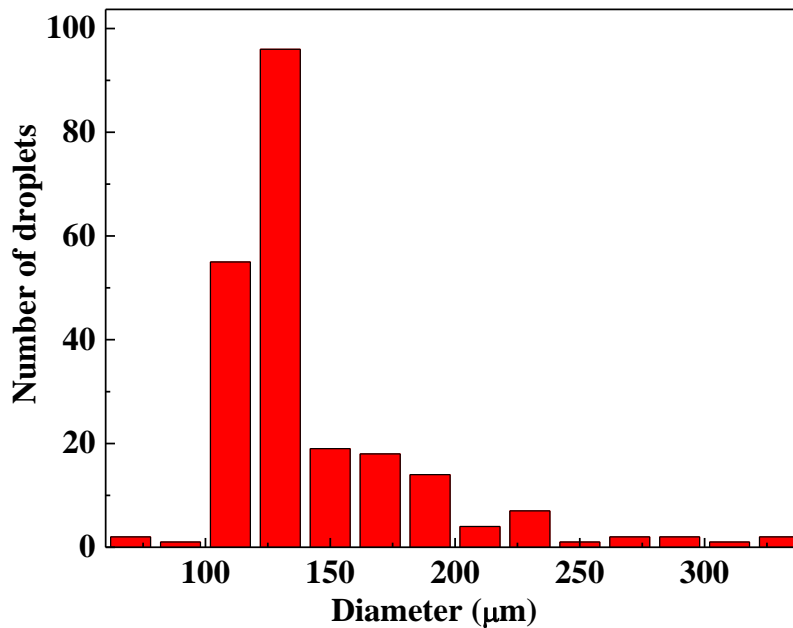
Figure 4-5 Size distribution of oil droplets generated by a T-junction

and prevent oil droplet adhesion to the surface by drastically minimizing contact area. One convenient way to prepare such underwater superoleophobic surfaces[127] is through electrodeposition, where the morphology of the deposited materials can be controlled by fine tuning of the deposition parameters such as the bath composition, pH, deposition voltage, current density, etc.[128]

We use electrodeposition in order to produce super-hydrophilic nickel cobalt hydroxide deposits with hierarchical micro/nano structures. The electrodeposits were produced in a primarily ethanol and isopropanol based medium with ~2% added volume of deionized water. A total of 0.1 mg/ml of $NiCl_2.6H_2O$ and $CoCl_2.6H_2O$ in a 1:1 ratio were dissolved into the solution to prepare the deposition bath. Deposition was carried out for 3 min at ~250 V/cm using a Matsusada high-voltage power source (Model EJ-2R100). Deposits were typically made on FTO glass substrates using a graphite foil counter electrode. Contact angle characterization images were analyzed by implementing the LB-ADSA plugin in ImageJ.[129]

4.5.2 Oil droplet generation

Oil droplets are generated following the standard protocol.[106, 130] The T-junction (MicroTee P-890, IDEX) is connected to two input microfluidic channels (150 μm in diameter) and one output channel (197 μm in diameter). Aqueous phase and oil phase are injected into two input channels, respectively, using syringe pumps (70-2202, Harvard Apparatus). The flow rate of aqueous phase and oil phase are 900 μL/min and 50 μL/min, respectively. The droplet size distribution generated is shown in Fig. 4-5. The majority of the droplets has a diameter in the range of 100 μm to 145 μm.

4.5.3 Lasing performance of Nile Red microdroplets

Lasing emission spectra of oil microdroplets with different concentrations of Nile Red are shown in Fig. 4-6(a). The diameter of oil microdroplets is 123 ± 11 μm. When the concentration of Nile Red is decreased from 1 mM to 7.5 μM, the lasing emission
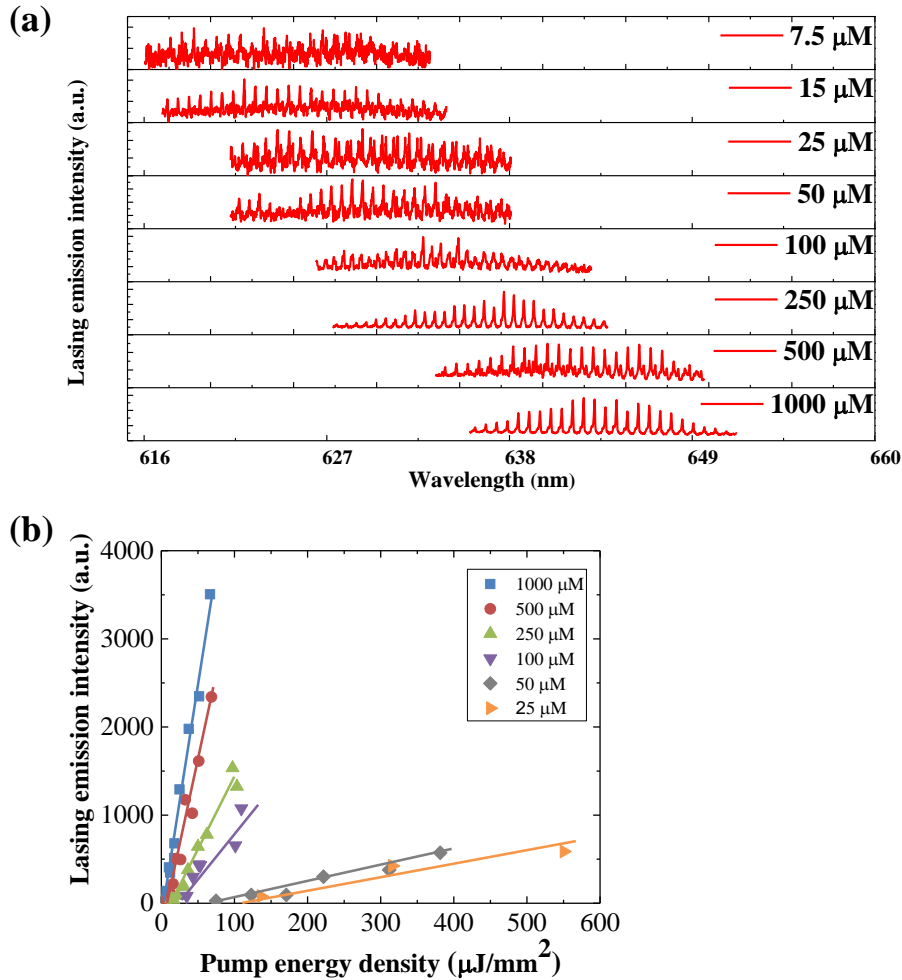
Figure 4-6 Lasing characterization of Nile Red oil droplets under different concentrations. (a) Lasing spectra of oil droplets with different concentrations of Nile Red (from 7.5 μM to 1 mM), pumped well-above threshold. Excitation wavelength: 532 nm. (b) Lasing threshold curves of oil droplets with different concentrations of Nile Red. The threshold for each concentration in increasing order is 111 μJ/mm², 68 μJ/mm², 27 μJ/mm², 14 μJ/mm², 8 μJ/mm², and 4 μJ/mm², respectively.

wavelengths shift to shorter wavelength. The lasing spectrum central position changes from 645 nm (1 mM Nile Red droplets) to 625 nm (7.5 µM Nile Red droplets). Fig. 4-6(b) shows the integrated lasing emission intensity as a function of the pump energy density for different dye concentrations. Their respective lasing thresholds are provided in the caption of Fig. 4-6.

4.5.4 Theoretical analysis of microdroplet dye lasers

Both DiI(3) and Nile Red microdroplet lasers can be modeled as the four-energy-level laser system. The corresponding population inversion condition can be written as:[19, 57, 82]

$$n_1 \sigma_e(\lambda_L) \geq (n_T - n_1)\sigma_a(\lambda_L) + \frac{2\pi m}{\lambda_L Q_0} \tag{4-1}$$

where n_T is the total concentration of the dye, n_1 is the concentration of the dye in the excited state, $\sigma_e(\lambda_L)$ ($\sigma_a(\lambda_L)$) is the dye emission cross-section (dye absorption cross-section) at the lasing wavelength λ_L, Q_0 is the microdroplet empty-cavity Q-factor, and m is the effective refractive index of the WGMs. At threshold, Eqn. (4-1) can be written as:

$$\gamma = \frac{\sigma_a(\lambda_L)}{\sigma_e(\lambda_L) + \sigma_a(\lambda_L)}\left[1 + \frac{Q_{abs}}{Q_0}\right] \tag{4-2}$$

where

$$Q_{abs} = 2\pi m / \lambda_L n_T \sigma_a(\lambda_L) \tag{4-3}$$

is the Q-factor related to the dye absorption. $\gamma \equiv n_1/n_t$ is the fraction of gain molecules in the excited state at the threshold. According to the laser theory, the lasing threshold, I_{th}, is determined by:

$$I_{th} = \frac{\gamma}{1-\gamma} \tag{4-4}$$

To solve lasing threshold according to Eqn. (4-2) - (4-4), the dye absorption cross-section and the dye emission cross-section at the lasing wavelength are measured in the experiments detailed below in Section VI and VIII, respectively.

The crucial difference between DiI(3) microdroplet laser and Nile Red microdroplet laser lies in the gain medium spatial distribution. In Nile Red laser, dye molecules are homogenously distributed in the microdroplet, as in the majority of dye lasers reported to date. However, since DiI(3) molecules are amphiphilic, which behaves like a surfactant, they will diffuse to and form a monolayer at the microdroplet surface first.

70

Any additional dye molecules will then homogenously distributed in the entire volume of the droplet. Therefore, the total concentration of the dye participating lasing (n_T) in DiI(3) laser needs to be corrected based on the following two cases.

In a droplet microcavity, WGMs form at the droplet surface (i.e., liquid-liquid interface in droplet lasers described in our work) through continuous total internal reflections and is confined inside of the droplet. Assume that WGMs spatial distribution occupies a layer with a thickness of $d_{WGMs} \sim (\lambda_L/n)$ from the droplet liquid-liquid interface. When a complete monolayer of DiI(3) is formed at the surface and there is no free dye molecules in the droplet, the total number of DiI(3) molecules are:

$$N = \frac{S}{IMD^2} = \frac{4\pi R^2}{IMD^2} \tag{4-5}$$

where S is the surface area of the droplet, R is the radius of the droplet, and IMD is the intermolecular distance between two adjacent DiI(3) molecules on the surface. Therefore the corresponding dye concentration in the droplet is written as:

$$C_c = \frac{N}{V} = \frac{N}{\frac{4}{3}\pi R^3} \tag{4-6}$$

where V is the volume of the droplet. C_c is defined as the critical concentration, where the number of DiI(3) molecules in the bulk solution is just enough to form a monolayer gain at the droplet surface and there is no free dye molecules left in the solution. When the bulk concentration is smaller than the critical concentration ($c < C_c$), the effective gain medium concentration experienced by the WGMs is

$$n_T(c) = \frac{V \cdot c}{V_{WGMs}} \tag{4-7}$$

$$V_{WGMs} = V - \frac{4}{3}\pi(R - d_{WGMs})^3 \tag{4-8}$$

When the bulk concentration is larger than the critical concentration ($c > C_c$), the effective gain medium concentration experienced by the WGMs is

$$n_T(c) = c + \left(\frac{1}{V_{WGMs}} - \frac{1}{V}\right) N \qquad (4\text{-}9)$$

For Nile Red microdroplet laser, the total concentration of the dye participating

lasing (n_T) is always equal to bulk solution concentration (c) in the droplet.

4.5.5 Fluorescence lifetime measurement

A custom-built fluorescence lifetime measurement system[131] is used to characterize the lifetime of Dil(3) and Nile Red. Briefly, laser light of 500 nm with a pulse width of ~800 ps is used to excite the sample. The fluorescence emission is detected by a photomultiplier tube (H10721-20, Hamamatsu). The signal is further amplified by a broadband preamplifier (C5594, Hamamatsu) and then acquired by a multi-channel oscilloscope (DPO 7254, Tektronix). The system response is measured by using the pure immersion oil as a control sample and is used to deconvolve the acquired fluorescence decay data from Dil(3) and Nile Red, respectively. The processed data is then fitted to a mono-exponential decay function to extract the lifetime value. According to the results shown in Fig. 4-7, the fluorescence lifetime of Dil(3) and Nile Red are 2.11 ns and 3.99 ns, respectively.
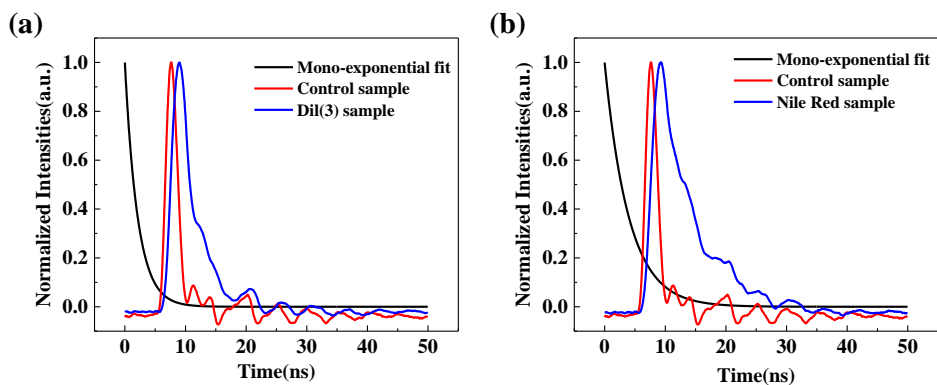
Figure 4-7 Fluorescence lifetime measurement. Fluorescence decay curves of 10 µM Dil(3) in mineral oil and 10 µM Nile Red in mineral oil are shown in (a) and (b), respectively. Control shows system response obtained with pure immersion oil. Mono-exponential fit reveals 2.11 ns lifetime for Dil(3) and 3.99 ns lifetime for Nile Red.

4.5.6 Absorption cross-section

A custom-built absorbance measurement setup is used to characterize the dye absorption cross-section. A tungsten halogen light source (HL-2000, Ocean Optics) is used to excite the sample placed in standard quartz cuvette and the fluorescence emission spectrum is measured with a spectrometer (HR 4000, Ocean Optics). The absorbance spectra of 7.5 μM DiI(3) and 7.5 μM Nile Red, $A(\lambda)$, are measured respectively. Absorption cross-section, $\sigma_a(\lambda)$, is calculated based on equation:

$$\sigma_a(\lambda) = \frac{-[\ln(10^{-A(\lambda)})]}{n(molecules/cm^3) \cdot l(cm)} = [cm^2/molecule] \qquad (4\text{-}10)$$

where l is the length of light path, n is the concentration of dye, and A is the absorbance. The absorption cross-section is shown in Fig. 4-8. The absorption cross-section values beyond 600 nm is obtained through Gaussian fitting extrapolation.
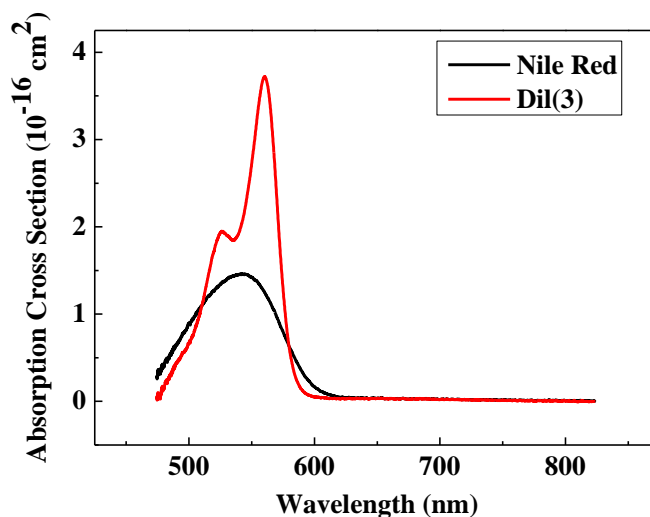
Figure 4-8 Absorption cross section of Nile Red and DiI(3) based on absorbance test with 7.5 μM solutions

4.5.7 Quantum yield measurement

To determine the quantum yield of Dil(3) and Nile Red, we measured the absorbance and fluorescence of both dyes (in immersion oil) in parallel with Rhodamine 6G (R6G) (in methanol). The absorbance and fluorescence tests are performed with Infinite M-200 (Tecan). The excitation (or absorption) wavelength is fixed at 500 nm. The experimental results are shown in Fig. 4-9. Based on Table. 4-1, the quantum yield can be calculated using equation:

$$\Phi_s = \Phi_{ref} \times \frac{FL-slope_s}{FL-slope_{ref}} \times \frac{RI_s^2}{RI_{ref}^2} \times \frac{\varepsilon_{ref}}{\varepsilon_s} \tag{4-11}$$

Table 4-1 Extinction coefficient (ε) and fluorescence efficiency ($FL-slope$) summary

Dyes	Extinction (ε)	$FL-slope$	RI
R6G/MeOH	$3.66 \times 10^4\,M^{-1}cm^{-1}$	$2827.17\,\mu M^{-1}$	1.3284 (methanol)
Dil(3)/ImOil	$3.57 \times 10^4\,M^{-1}cm^{-1}$	$753.38\,\mu M^{-1}$	1.516 (immersion oil)
Nile Red/ImOil	$2.12 \times 10^4\,M^{-1}cm^{-1}$	$1064.89\,\mu M^{-1}$	1.516 (immersion oil)
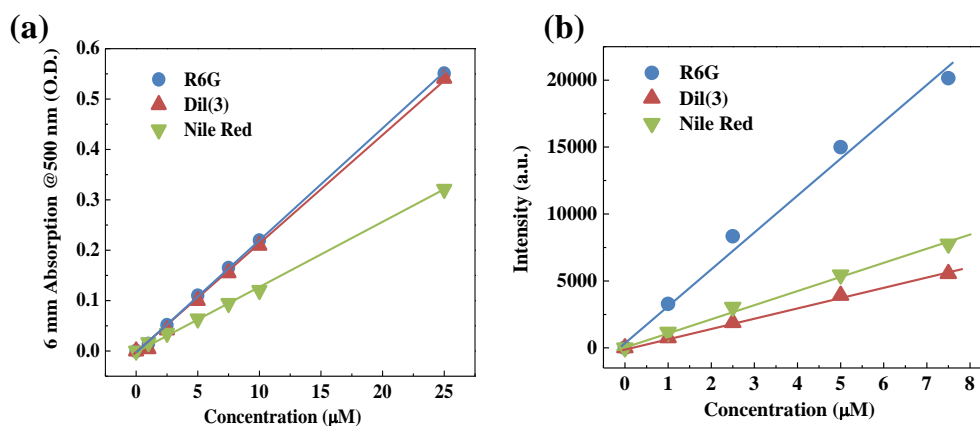
Figure 4-9 Measurements for absorbance and fluorescent intensity. (a) Absorbance of R6G, Dil(3), and Nile Red at 500 nm. (b) Integrated fluorescence intensity vs. concentration for R6G, Dil(3), and Nile Red. Integration is taken over a 270 nm span between 480-750 nm for R6G and 530-800 nm for Dil(3) and Nile Red.

where Φ is the quantum yield, RI is the refractive index of the solvent, $FL - slope$ is the fluorescence efficiency, and ε is the extinction coefficient. We calculate that $\Phi_{Dil3} = 0.33$ and $\Phi_{Nile\ Red} = 0.79$ ($\Phi_{ref} = \Phi_{R6G} = 0.93$ for R6G in methanol[132]).

4.5.8 Fluorescence quantum distribution and emission cross-section calculation

Based on the emission spectra and Gaussian fit shown in Fig. 4-10, and the fluorescence quantum yield of Dil(3) and Nile Red ($\Phi_{Dil(3)} = 0.33$, $\Phi_{Nile\ Red} = 0.79$), Dil(3) fluorescence quantum distribution at 618 nm and Nile Red fluorescence quantum distribution at 635 nm are calculated as below:

$$E(\lambda_L) = \frac{\Phi}{w\sqrt{2\pi}} exp\left[-\frac{(\lambda_L - \lambda_0)^2}{2w^2}\right] \tag{4-12}$$

where $E(\lambda_L)$ is the fluorescence quantum distribution, and λ_0 and w are the center wavelength and standard deviation of the Gaussian fit. From the results obtained in Fig. 4-10, $w_{Dil(3)} = 40.45 nm$, $w_{Nile\ Red} = 43.16 nm$, $\lambda_{0,Dil(3)} = 578 nm$, and $\lambda_{0,Nile\ Red} = 610 nm$, respectively.

Therefore,

$$E(618nm)_{Dil(3)} = \frac{0.33}{40.45nm\sqrt{2\pi}} exp\left[-\frac{(618-578)^2}{2\times40.45^2}\right] = 2\cdot10^{-3}nm^{-1}$$

$$E(635nm)_{Nile\ Red} = \frac{0.79}{43.16nm\sqrt{2\pi}} exp\left[-\frac{(635-610)^2}{2\times43.16^2}\right] = 6.2\cdot10^{-3}nm^{-1}$$

According to the following equation:[133]

(a) **(b)**
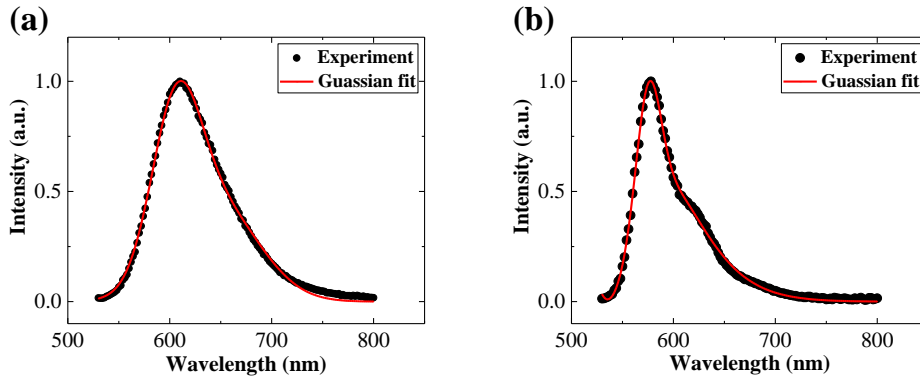
Figure 4-10 Fluorescence measurements for Nile Red and Dil(3). (a) Nile Red fluorescence spectrum. Gaussian fit reveals 610 nm center wavelength and 43.16 nm standard deviation. (b) Dil(3) fluorescence spectrum. Gaussian fit reveals 578 nm center wavelength and 40.45 nm standard deviation.

$$\sigma_e(\lambda_L) = \frac{\lambda_L^4 \cdot E(\lambda_L)}{8\pi \cdot c \cdot n_L^2 \tau_F} \tag{4-13}$$

where n_L is the medium refractive index at λ_L, and c is the speed of light in a vacuum.

Using experimentally measured data as detailed previously, the emission cross-section of Dil(3) at 618 nm is estimated to be $\sigma_e(\lambda_L) = 7.98 \times 10^{-17} cm^2$ and the emission cross-section of Nile Red at 635 nm is estimated to be $\sigma_e(\lambda_L) = 1.46 \times 10^{-16} cm^2$.

Chapter 5

Droplet-on-demand on-chip optofluidic lasers

In this chapter, we successfully demonstrated droplet-on-demand on-chip optofluidic lasers. We were able to generate different droplets ranging from 28.2 μm to 90.4 μm and the same droplet that grew from 45 μm to 80 μm with one generation round. We also achieved lasing emissions from the droplets that were generated, showing a lasing threshold as low as 1 μJ/mm^2 when the diameter of droplets was around or above 50 μm. We believe the drop-on-demand on-chip optofluidic laser platform offers great potentials for intra-cavity and interfacial-cavity sensing applications.

5.1 Introduction

Droplets, as optical cavities, confine whispering gallery modes (WGMs) with high quality factors in small volumes.[134, 135] Due to the interfacial tension between droplets and the surrounding environment, the nearly perfect spherical shape of droplets minimizes the scattering losses on the residual surface inhomogeneities, resulting a high Q factor for WGMs.[33] Therefore, droplets have been attractive for the development of optofluidic lasers. More specifically, both static droplet lasers[24-26, 28, 136] and droplet lasers on the flow[2, 29-32] have been demonstrated. Static droplet lasers often have droplets generated by ultrasonic nebulizers with a large size distribution, and keep droplets still through various ways, such as ultrasonic trapping,[24] superhydrophobic surface,[25] optical trapping[25] and viscous phase embedding.[136] The droplets generally have a prolonged lifetime before they deform, which allows enough working time for the integration of biosensing applications. Droplet lasers on the flow mostly utilize microfluidic networks. Due to the well-defined dimensions of microfluidics and high flow rates of fluids, droplets on the flow are highly

monodispersed with high throughput. However, the high linear velocity of individual droplets often makes it challenging to keep track on them.

In our work, a platform with micro-nozzle structures and assisted by pneumatic control was introduced to develop a droplet-on-demand on-chip optofluidic laser system,

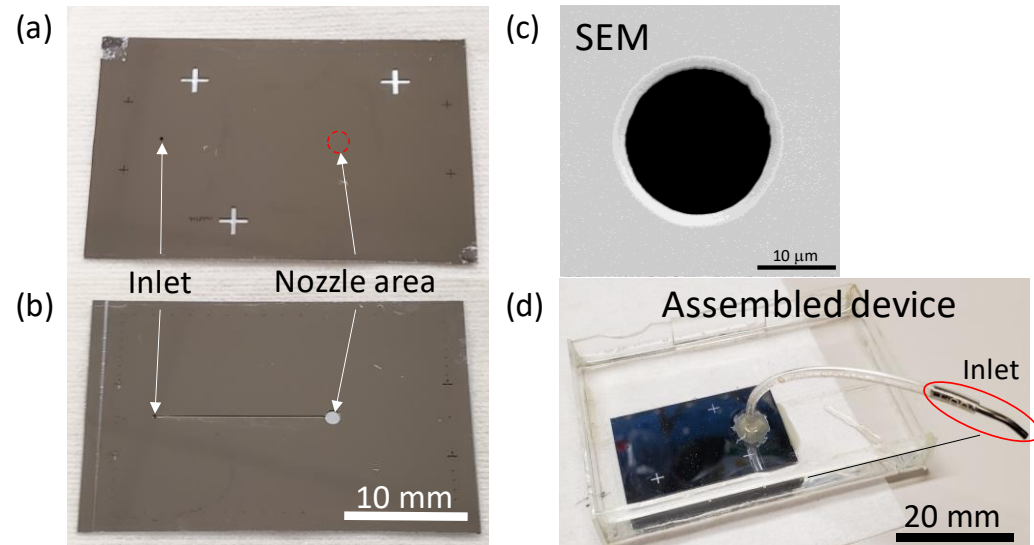Figure 5-1 The design of Si nozzle device. Pictures of frontside (a) and backside (b) of the Si nozzle chip. (c) The SEM images of the Si nozzle on the frontside, which was 20 μm in diameter. (d) The picture of an assemble Si nozzle device, which was immersed in 10 mM SDS solution in a glass container.
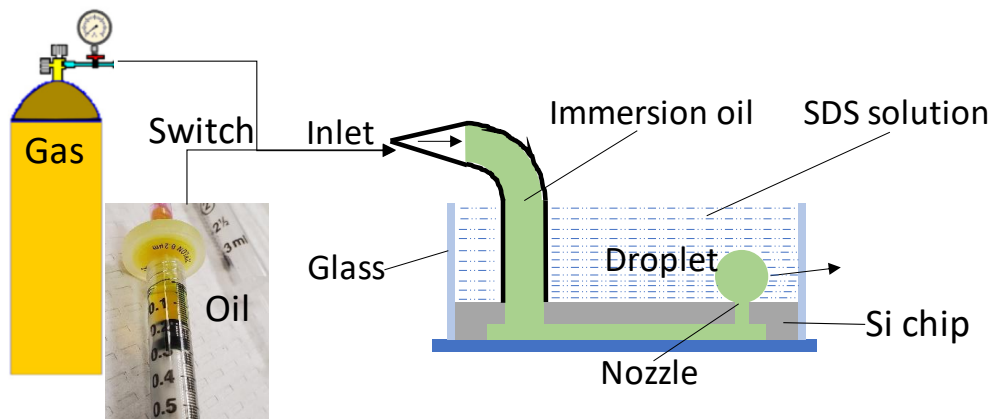

Figure 5-2 The schematics of Si nozzle device and its connections with immersion oil supply and pressurized gas supply.

aiming at combining the advantages from both static droplet lasers and droplet lasers on the flow laser platforms. The main problem to tackle in our platform is how to generate monodisperse microdroplets, which has been tried out through other platforms, like microfluidics, inkjet printing, spray nozzles and vibrating orifices. However, the key to a monodisperse droplet generation is to have a real time size monitoring and active control of their size. Size measurement is usually done by using microscope images of droplets, which is limited by diffraction to a few hundreds of nanometers. A better way is to utilize the spectrum shift of WGMs to closely monitor the size change of droplets for an extremely precise size control. In the extreme case, 1 pm size change have been demonstrated.[137, 138] Due the time limitation and difficulties of implementing WGMs theory, microscope images of droplets were adopted for the real time size monitoring for droplet generation. We successfully demonstrated a droplet-on-demand generation with diameter ranging from 28.2 μm to 90.4 μm, and characterized the lasing thresholds for droplet size from 40 mm to 55 μm. The droplet-on-demand on-chip optofluidic laser system opens more possibilities for the development of on-chip tunable lasers, intra-cavity/interfacial-cavity sensing applications.

5.2 Materials and methods

The Si nozzle chip was designed to have a straight channel in the backside, one inlet and one nozzle on the frontside. After deep Si etching on both sides of the Si chip, the inlet and nozzle on the frontside got connected with the channel on the backside. The detailed fabrication process has been discussed in Chapter 3. The frontside and backside of the fabricated Si chip were shown in Fig. 5-1(a) and (b), respectively. On the backside, a small reservoir was created right beneath the nozzle. The diameter of nozzle on the frontside is 20 μm, as shown in Fig. 5-1(c). A plastic tubing was glued to the inlet for oil delivery and applying pressure. The assembled device was shown in Fig. 5-1(d), immersed
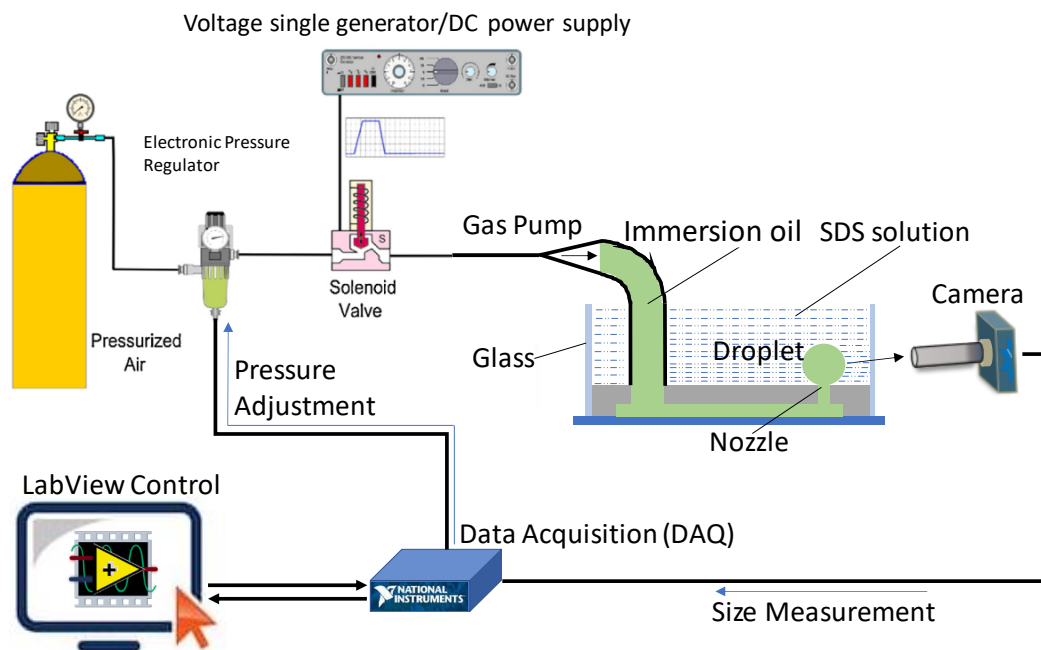
Figure 5-3 The schematic of the experimental setup, which is a feedback control for the droplet generation.

in 10 mM SDS solution in a glass container. The SDS was used to prevent the immersion oil getting stuck on the nozzle surface and keep immersion oil droplets at a high contact angle. Before starting the droplet generation, the assembled nozzle device was loaded with immersion oil through the inlet tubing. Then, the same inlet was switched to be connected to pressurized gas supply for droplet generation. The schematics was shown in Fig. 5-2.

As shown in Fig. 5-3, the generation of droplets were controlled by the feedback control loop. The pressurized air tank was the input of the electronic pressure regulator. The input pressure was 5 psi. The output pressure range of the electronic pressure regulator was from 0 psi to 1 psi. The on/off of the solenoid valve was controlled by a DC power supply. The pre-loaded immersion oil was driven by the electronic pressure regulator. Once oil emerged from the nozzle on the top side, a side-view camera captured the formation of a droplet and measured its size. The size information was sent to the computer and

compared to the target size. Depending on the current size information, the output pressure of the electronic pressure regulator was adjusted accordingly until the target size had been reached.

The electronic pressure regulator was the key part in the feedback control loop. Thus, the parameter performance of the regulator was studied. The output pressure of the regulator was measured at different command voltages, which was plotted out in Fig. 5-4(a). When the command voltage was below 0.5 V, the output pressure was 0 psi; when the command voltage was equal to or higher than 0.5 V, the relationship of pressure vs voltage was represented by the linear function of $Pressure(psi) = 0.09994 \times Voltage(V) - 0.05034$. The actual voltage response from the pressure regulator was also monitored and recorded in Fig. 5-4(b) when the set point voltage slowly increased from 0.5 V to 10 V. When the set point voltage changed by 0.5 V, it took around 5 seconds (rising time) for the monitor voltage to catch up. When the monitor voltage reached the set point voltage, the noise level of the monitor voltage was around 2~3%, which was shown in Fig. 5-4(c). The front panel of the LabView program is showing in Fig. 5-5. The window "Monitor Voltage (V)" displayed the real-time voltage of Set point voltage and Monitor voltage. The window
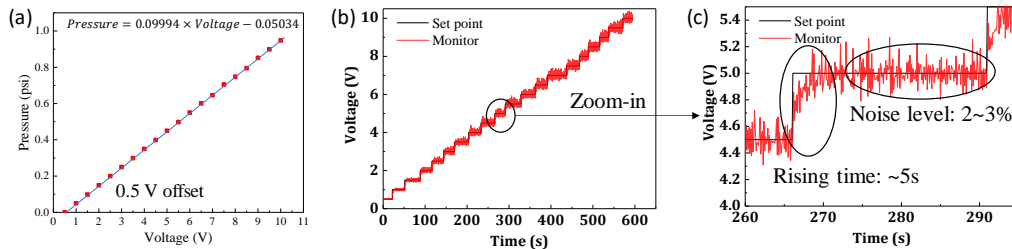
Figure 5-4 The parameter performance of the electronic pressure regulator. (a) The linear relationship between output pressure and command voltage. (b) The real time response of actual monitor voltage on the electronic pressure regulator comparing to the set point voltage for pressure control. (c) The zoom-in plot of (b), showing the rising time and noise level of the monitor voltage on the electronic pressure regulator.

"Diameter (um)" displayed the real-time diameter of Target Size and Current Size. The window "Real time droplet monitoring" monitored the growth motion of droplets and measured the size of droplets. The generation of process of droplets had two steps, first, initial generation, second, size tuning. Parameters, such as "Initial Inc Volt (V)", "Fast increase (s)", "Wait to increase (s)", were for the initial generation step. Parameter "Tuning Inc Volt (V)" was for the size tuning step.

5.3 Experiment results

To generate droplets, the voltage signal of initial generation step was shown in
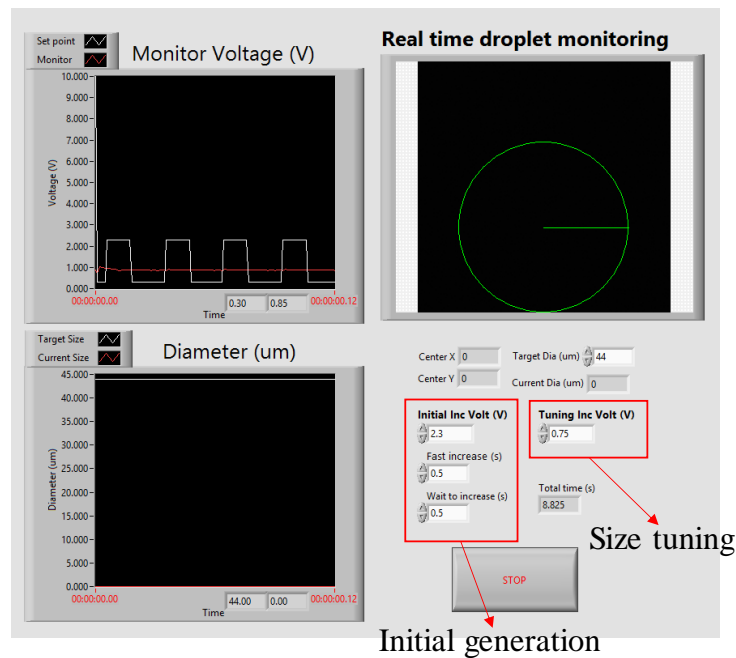
Figure 5-5 The front panel of the LabView program for droplet generation control. "Monitor Voltage (V)" window displayed the voltage change of Set point voltage and Monitor voltage. "Diameter (um)" window displayed the diameter change of Target Size and Current Size. "Real time droplet monitoring" window displayed the growth process of immersion oil droplets.

Fig.5- 6(a). The Set Voltage had three parameters: V_1 was the "Initial Inc Volt (V)", 2.3 V; T_1 was the "Fast increase (s)", 0.5 s; T_2 was the "Wait to increase (s)", 0.5 s. Due to the 5-s rising time, as shown in Fig. 5-4(c), the Actual Voltage was not able to keep up with the

Set Voltage, resulting in an oscillating signal between 0.8 V and 1.5 V. After applying the oscillating signals for around 240 s, immersion oil started to emerge from the nozzle and formed a droplet, which was shown in Fig. 5-6(b). While the oscillating signal was applied, immersion oil only formed a dome-shape drop on the nozzle, as shown in the inset picture of Fig. 5-6(c). However, after a few hundreds of oscillating cycles, a complete droplet would be formed at certain time point, and then the LabView program quickly progressed into the second step, Size Tuning. The size of droplet at the first step, initial generation, ranged from 20 μm to 40 μm. The Figure 5-6(d) showed the transition from initial generation to size tuning for immersion oil droplets. The inset of Fig 5-6(d) showed an example of a formed droplet after initial generation. To further control the droplet size to be the target size, the control algorithm for size tuning was shown in Fig. 5-7. First, the current droplet size (D_c) was compared with the target droplet size (D_t). If $D_c < D_t$, then the difference between current diameter and target diameter was compared with 14 μm. To be note that, 14 μm is an arbitrary number set by user. If $D_t - D_c \geq 14\mu m$, the "Tuning Inc Volt(V)" was set to be 0.75 V. This parameter sent commands to the pressure regulator, so that a constant pressure was applied to push the droplet to grow at a constant growth rate. 0.75 V was chosen based on experimental experience. Thus, the droplet on the nozzle would grow at a constant rate for some time until the difference between current diameter and target diameter became less than 14 μm. When $D_t - D_c < 14\mu m$, the applied voltage on the pressure regulator was adjusted based on a linear function, written as below:

$$\frac{(D_t - D_c)}{14\mu m} \times \frac{Tuning\ Inc\ Volt(V) - 0.5V}{0.5V} + 0.5V \tag{5-1}$$
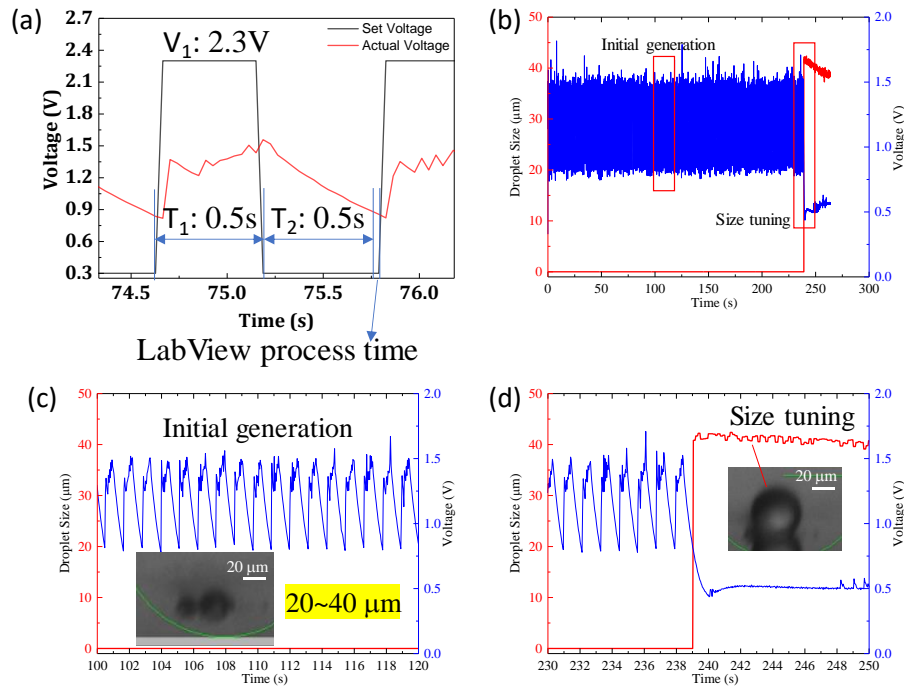
Figure 5-6 The initial generation for droplets. (a) The periodic control signals for initial generation. (b) The overall periodic signals for initial generation. (c) The zoom-in plot for initial generation signals. (d) The zoom-in plot for the transition region when oil just came out from nozzle and formed a droplet. V_1: Initial Inc Volt (V). T_1: Fast increase(s). T_2: Wait to increase(s).

The smaller the difference between current diameter and target diameter became, the slower the droplet grew. Until $D_t - D_c = 0$, the voltage on pressure regulator was set to 0.5 V and the growth of droplet was stopped. With the two-step droplet generation control, droplet generation with different sizes have been carried out. As shown in Fig. 5-8(a), different target diameters were set, and the increase trends of droplet diameters were recorded in real time. All the generation were conducted at single size tuning step with different rounds of generation. For example, when the target size was set to be 40 μm, the final diameter achieved through the LabView program was 35.1 μm; when the target size was set to be 50 μm, the final diameter was 49.9 μm; when the target size was set to be 90 μm, the final diameter was 89.9 μm. It shows that when droplet diameter is larger than 50
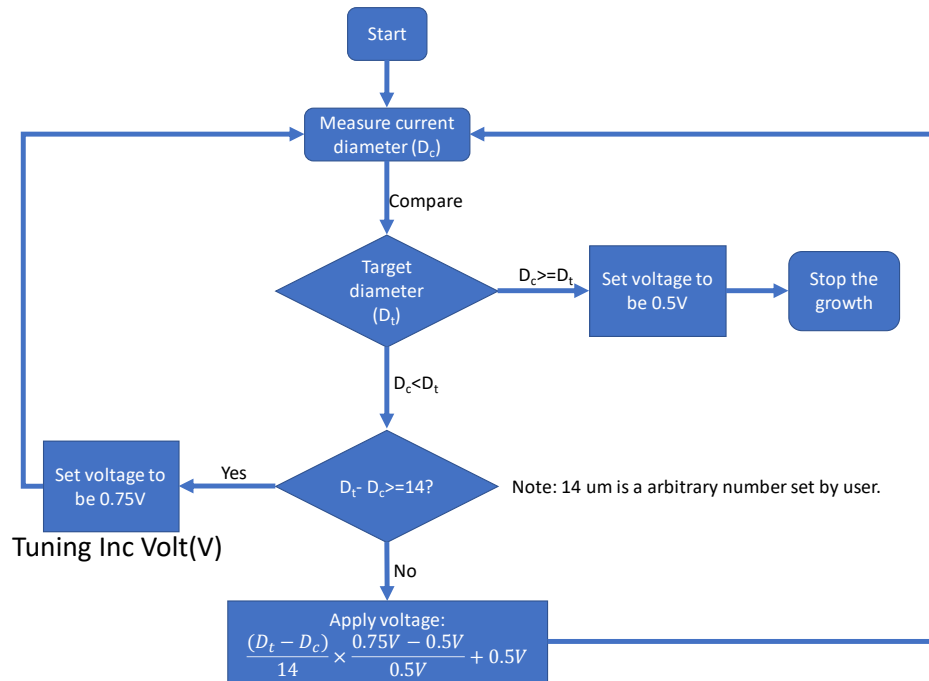
Figure 5-7 The flow chart for the second step of droplet generation, size tuning

μm, the final diameter can reach the target size within 1 μm deviation. However, when the target diameter is smaller than 50 μm, the final diameter presents a larger size deviation. Besides, multiple size tuning steps were tested, as shown in Fig. 5-8(b). Firstly, the target size was set at 50 μm. After a period of stabilization, final diameter reached at 45 μm. Then, the target size was set at 55 μm/60 μm/65 μm/80 μm, the final diameter reached 55 μm/60 μm/65 μm/80 μm, respectively. The difference between final diameter and target diameter was consistent with the generations with single size tuning step. Overall, droplets with diameter ranging from 35.1 μm to 94.9 μm were generated.
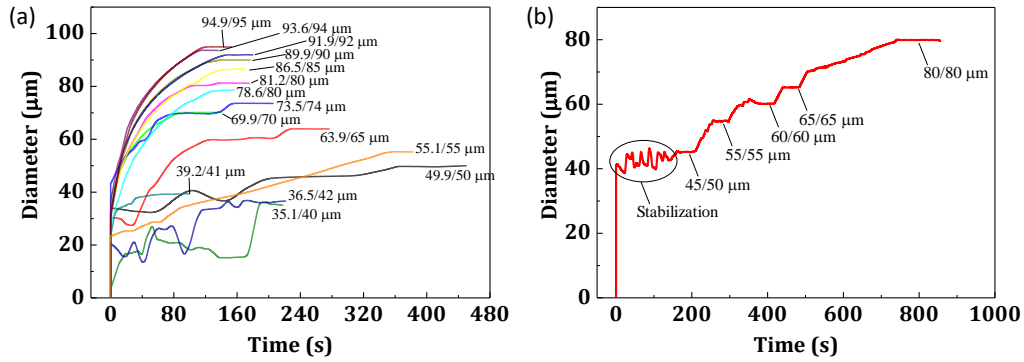
Figure 5-8 Droplet on demand generation. (a) Single size tuning step. (b) Multiple size tuning steps. Note: size label on each plot means "final diameter/target diameter".

However, the size information through optical images always has a measurement error. In order to investigate the measurement accuracy through optical images, the whispering gallery modes (WGMs) from lasing droplets were utilized as the tool to extract the real droplet size. As shown in Fig. 5-9, the lasing spectra of droplets with different sizes were presented. The diameter information for each spectrum was labelled on the right-upper corner as diameter from spectrum/diameter from optical images. The diameter from spectrum was calculated from the free spectral range (FSR) of each spectrum. The formula is shown as following:

$$D = \frac{\lambda^2}{FSR \cdot n \cdot \pi}$$

(5-2)
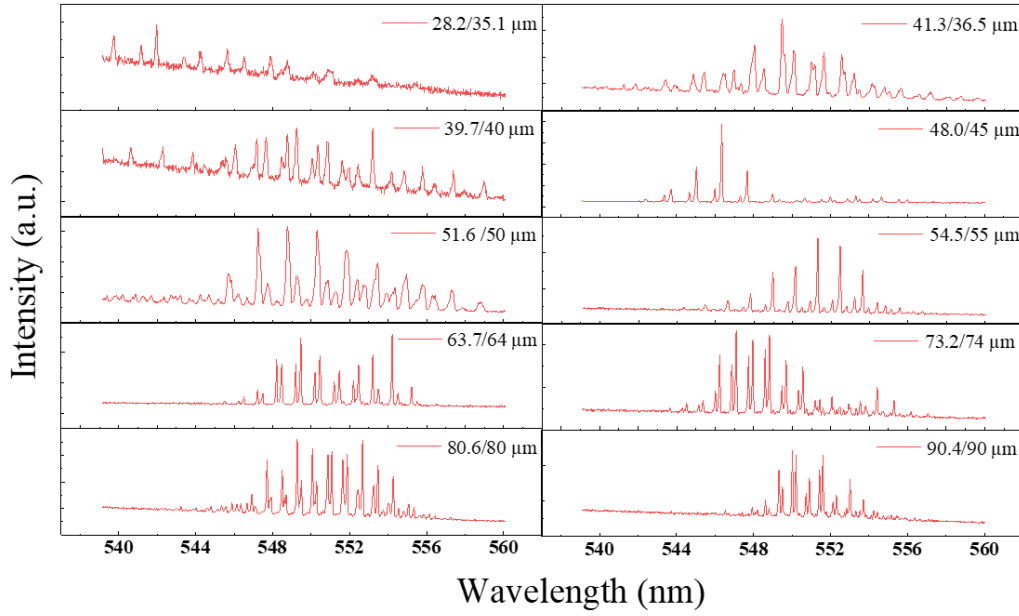
Figure 5-9 Lasing emission of droplets at different sizes.

in which, $\lambda = 550nm$, $n = 1.515$, FSR is measured from each spectrum. The size measurement from spectrum provided a reference which allowed an error correction of diameters measured

$$y_2 = 0.98933x + 0.88431$$

$$y_1 = 1.52839x - 20.93737$$
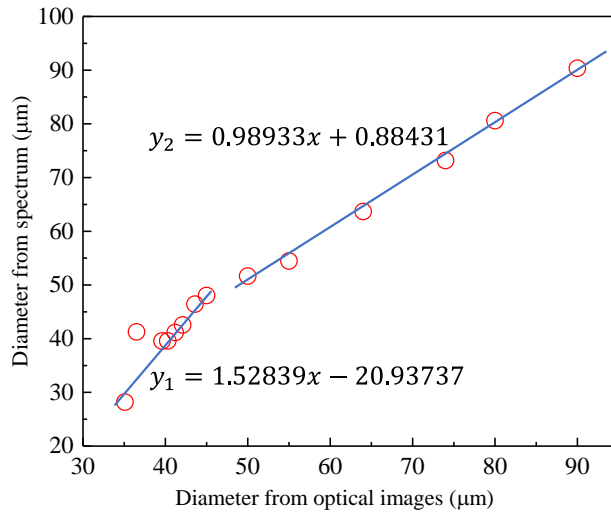
Figure 5-10 The relationship of diameter from spectrum vs diameter from optical images

from optical images. Therefore, the relationship of diameter from spectrum vs diameter from optical images was plotted out in Fig. 5-10. Followed by linear fitting, it turned out that there were two different linear relations when the diameter from optical images was below and above 45 μm:

$$y = \begin{cases} 0.98933x + 0.88431(x \geq 45 \ \mu m) \\ 1.52839x - 20.93737(x < 45 \ \mu m) \end{cases} \tag{5-3}$$

in which, x represents the diameter from optical images, y represents the diameter from spectrum. Thus, by applying Eqn. (5-3) to the diameter measured from optical images, their measurement error can be minimized. So far, the droplet on-demand generation has been demonstrated.

The lasing emission characterization of droplets from 40 to 55 μm has been studied. The droplets were doped with 5 mM BODIPY, as gain medium. The lasing intensity vs pump energy density relation for a 41.3-μm droplet was studied and presented
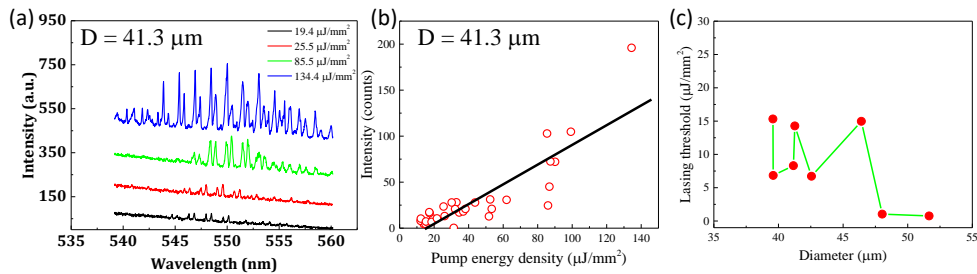
Figure 5-11 The lasing emission characterization of droplets from 40 μm to 55 μm. (a) The lasing emission spectrum of a 41.3-μm droplet under different pump energy densities. (b) The relation of lasing intensity vs pump energy density for the lasing threshold measurement. The lasing threshold was 14.3 μJ/mm^2. (c) The lasing thresholds for droplets ranging from 40 μm to 55 μm.

in Fig. 5-11(a) and (b). Through linear fitting, the lasing threshold of the 41.3-μm droplet was 14.3 μJ/mm^2. The lasing threshold summary of droplets from 40 to 55 μm was presented in Fig. 5-11(c). The droplet size was around 50 μm, the lasing threshold became around 1 μJ/mm^2, much lower than droplets with smaller size. This may because that the

droplet size was large enough, so that the contact area between droplets and the nozzle caused a much less radiative loss, which contributed to a reduced lasing threshold.

5.4 Conclusions

In summary, we have successfully demonstrated droplet on-demand generation and on-chip droplet lasers. We believe the on-chip droplet laser platforms have potential applications on intra-cavity sensing and interfacial cavity sensing.

Chapter 6

Summary and Outlook

In this dissertation, we have successfully developed an integrated optofluidic droplet laser based on micro-nozzle structures and extended our droplet laser platform into a laser array. We also developed a feedback control system with pneumatic control assisted to have droplet on-demand for the reconfigurable on-chip droplet laser system. At last, we studied a droplet laser system with a monolayer gain at the surface of droplets, which maximized the efficiency of gain molecules to lasing emissions.

In contrast to the traditional solid-phase-based lasers, optofluidic lasers offer advantages on flexible and reconfigurable gain materials and optical cavities, easy integration with microfluidic devices, flexibility of implementing different active tuning mechanisms. As for the development of optofluidic droplet lasers, we will further develop the integrated on-chip droplet lasers to have smaller footprint and smaller droplets as optical cavities. The integration of active tuning mechanisms, such piezo-electric vibration or deformation, ultrasonic waves, AC/DC electric field modification, and temperature control, could add more freedom for tunable droplet laser development. The liquid-liquid interface of droplets could lead to meaningful research in many biological applications.

However, there are a few challenges which need to overcome in the future. First, the surface property of nozzles plays a key role to maintain a high contact angle for droplets. The surface would deteriorate over time, as well as the Q factor of droplets. This affects the consistency of the performance of the droplet laser. To develop effective surface treatment methods for different materials would be very important to prolong the lifetime of the laser system. Second, the regeneration (removal) of the droplets needs a better way, other than relying on the one-directional water flow rinsing. Because the one-directional water flow can't remove the droplets from the nozzle surface evenly, often leaving some residues on the nozzle along the

direction of water flow. By having a symmetric design for water rinsing function and placing the rinsing water flow front much closer to the droplets, this may help to reduce the residues around the nozzle. Third, currently the pump light coupling method is through free space, which is attenuated by every interface that the light encounters. So is the lasing emission from droplets. By embedding fibers near the droplets for excitation and emission collection, the light coupling efficiency and the lasing emission collection would be significantly increased. Fourth, the size tuning of droplets needs to happen at very small incremental steps to tune the lasing wavelength of droplet lasers, which is often challenging to observe from optical images. Thus, WGMs should be utilized to monitor the size changes.

Lastly, we believe that our on-chip droplet laser platform will have significant impact in the following areas. (1) It will provide a powerful platform for the development of high-speed wavelength switching light sources and on-chip spectroscopic analysis. (2) Its liquid-liquid interface will allow laser gain profile engineering and enable various studies in biological fields. (3) The size tuning capability will offer a flexible sensing platform for intra-cavity and interfacial cavity sensing applications.

References

1. V. R. Horowitz, D. D. Awschalom and S. J. L. o. a. C. Pennathur, *Optofluidics: field or technique?*, 2008, **8**, 1856-1863.

2. M. Tanyeri, R. Perron and I. M. Kennedy, *Lasing droplets in a microfabricated channel, Optics letters*, 2007, **32**, 2529-2531.

3. M. Lončar, A. Scherer and Y. Qiu, *Photonic crystal laser sources for chemical detection, Applied Physics Letters*, 2003, **82**, 4648-4650.

4. A. Kiraz, A. Sennaroglu, S. Doğanay, M. Dündar, A. Kurt, H. Kalaycıoğlu and A. Demirel, *Lasing from single, stationary, dye-doped glycerol/water microdroplets located on a superhydrophobic surface, Optics communications*, 2007, **276**, 145-148.

5. K. Ichimura, S.-K. Oh and M. Nakagawa, *Light-driven motion of liquids on a photoresponsive surface, Science*, 2000, **288**, 1624-1626.

6. Y. Sun and X. Fan, *Distinguishing DNA by Analog-to-Digital-like Conversion by Using Optofluidic Lasers, Angewandte Chemie International Edition*, 2012, **51**, 1236-1239.

7. C. Monat, P. Domachuk and B. Eggleton, *Integrated optofluidics: A new river of light, Nature photonics*, 2007, **1**, 106.

8. B. Helbo, A. Kristensen and A. Menon, *A micro-cavity fluidic dye laser, Journal of Micromechanics and Microengineering*, 2003, **13**, 307.

9. Q. Kou, I. Yesilyurt and Y. Chen, *Collinear dual-color laser emission from a microfluidic dye laser, Applied physics letters*, 2006, **88**, 091101.

10. G. Aubry, Q. Kou, J. Soto-Velasco, C. Wang, S. Meance, J. He and A. Haghiri-Gosnet, *A multicolor microfluidic droplet dye laser with single mode emission, Applied Physics Letters*, 2011, **98**, 111111.

11. M. C. Gather and S. H. Yun, *Single-cell biological lasers, Nature Photonics*, 2011, **5**, 406.

12. Y.-C. Chen, X. Tan, Q. Sun, Q. Chen, W. Wang and X. Fan, *Laser-emission imaging of nuclear biomarkers for high-contrast cancer screening and immunodiagnosis, Nature biomedical engineering*, 2017, **1**, 724.

13. W. Wang, C. Zhou, T. Zhang, J. Chen, S. Liu and X. Fan, *Optofluidic laser array based on stable high-Q Fabry–Pérot microcavities, Lab on a Chip*, 2015, **15**, 3862-3869.

14. S. Balslev and A. Kristensen, *Microfluidic single-mode laser using high-order Bragg grating and antiguiding segments, Optics Express*, 2005, **13**, 344-351.

15. Z. Li, Z. Zhang, T. Emery, A. Scherer and D. Psaltis, *Single mode optofluidic distributed feedback dye laser, Optics Express*, 2006, **14**, 696-701.

16. M. Gersborg-Hansen and A. Kristensen, *Optofluidic third order distributed feedback dye laser, Applied Physics Letters*, 2006, **89**, 103518.

17. Y. Chen, Z. Li, M. D. Henry and A. Scherer, *Optofluidic circular grating distributed feedback dye laser, Applied Physics Letters*, 2009, **95**, 031109.

18. M. Karl, G. L. Whitworth, M. Schubert, C. P. Dietrich, I. D. Samuel, G. A. Turnbull and M. C. Gather, *Optofluidic distributed feedback lasers with evanescent pumping: Reduced threshold and angular dispersion analysis, Applied Physics Letters*, 2016, **108**, 261101.

19. H.-J. Moon, Y.-T. Chough and K. An, *Cylindrical microcavity laser based on the evanescent-wave-coupled gain, Physical review letters*, 2000, **85**, 3161.

20. S. I. Shopova, H. Zhou, X. Fan and P. Zhang, *Optofluidic ring resonator based dye laser, Applied physics letters*, 2007, **90**, 221101.

21. W. Lee, H. Li, J. D. Suter, K. Reddy, Y. Sun and X. Fan, *Tunable single mode lasing from an on-chip optofluidic ring resonator laser, Applied Physics Letters*, 2011, **98**, 061103.

22. A. Kiraz, Q. Chen and X. Fan, *Optofluidic lasers with aqueous quantum dots, ACS photonics*, 2015, **2**, 707-713.

23. M. Hossein-Zadeh and K. J. Vahala, *Fiber-taper coupling to Whispering-Gallery modes of fluidic resonators embedded in a liquid medium, Optics express*, 2006, **14**, 10800-10810.

24. H. Azzouz, L. Alkhafadiji, S. Balslev, J. Johansson, N. A. Mortensen, S. Nilsson and A. Kristensen, *Levitated droplet dye laser, Optics Express*, 2006, **14**, 4374-4379.

25. E. Özelci, M. Aas, A. Jonáš and A. Kiraz, *Optofluidic FRET microlasers based on surface-supported liquid microdroplets, Laser Physics Letters*, 2014, **11**, 045802.

26. M. Aas, A. Jonáš, A. Kiraz, O. Brzobohatý, J. Ježek, Z. Pilát and P. Zemánek, *Spectral tuning of lasing emission from optofluidic droplet microlasers using optical stretching, Optics express*, 2013, **21**, 21380-21394.

27. R. Chen and H. D. Sun, *Tuning whispering gallery mode lasing from self-assembled polymer droplets, Scientific reports*, 2013, **3**, 1362.

28. M. Humar and S. H. Yun, *Intracellular microlasers, Nature photonics*, 2015, **9**, 572-576.

29. S.-X. Qian, J. B. Snow, H.-M. Tzeng and R. K. Chang, *Lasing droplets: highlighting the liquid-air interface by laser emission, Science*, 1986, **231**, 486-488.

30. S. K. Tang, Z. Li, A. R. Abate, J. J. Agresti, D. A. Weitz, D. Psaltis and G. M. Whitesides, *A multi-color fast-switching microfluidic droplet dye laser, Lab on a Chip*, 2009, **9**, 2767-2771.

31. S. K. Tang, R. Derda, Q. Quan, M. Lončar and G. M. Whitesides, *Continuously tunable microdroplet-laser in a microfluidic channel, Optics express*, 2011, **19**, 2204-2215.

32. L. Zheng, M. Zhi, Y. Chan and S. A. Khan, *Embedding liquid lasers within or around aqueous microfluidic droplets, Lab on a Chip*, 2018, **18**, 197-205.

33. M. L. Gorodetsky, A. A. Savchenkov and V. S. Ilchenko, *Ultimate Q of optical microsphere resonators, Optics Letters*, 1996, **21**, 453-455.

34. A. Serpengüzel, J. C. Swindal, R. K. Chang and W. P. Acker, *Two-dimensional imaging of sprays with fluorescence, lasing, and stimulated Raman scattering, Applied optics*, 1992, **31**, 3543-3551.

35. A. Jonáš, Y. Karadag, M. Mestre and A. Kiraz, *Probing of ultrahigh optical Q-factors of individual liquid microdroplets on superhydrophobic surfaces using tapered optical fiber waveguides, JOSA B*, 2012, **29**, 3240-3247.

36. S. Maayani, L. L. Martin and T. Carmon, *Water-walled microfluidics for high-optical finesse cavities, Nature communications*, 2016, **7**, 10435.

37. S. Avino, A. Krause, R. Zullo, A. Giorgini, P. Malara, P. De Natale, H. P. Loock and G. Gagliardi, *Direct Sensing in Liquids Using Whispering-Gallery-Mode Droplet Resonators, Advanced Optical Materials*, 2014, **2**, 1155-1159.

38. R. Symes, R. M. Sayer and J. P. Reid, *Cavity enhanced droplet spectroscopy: Principles, perspectives and prospects, Physical Chemistry Chemical Physics*, 2004, **6**, 474-487.

39. V. Vassiliev, V. Velichansky, V. Ilchenko, M. Gorodetsky, L. Hollberg and A. Yarovitsky, *Narrow-line-width diode laser with a high-Q microsphere resonator, Optics Communications*, 1998, **158**, 305-312.

40. S. Schiller and R. L. Byer, *High-resolution spectroscopy of whispering gallery modes in large dielectric spheres, Optics Letters*, 1991, **16**, 1138-1140.

41. H.-M. Tzeng, K. F. Wall, M. Long and R. Chang, *Laser emission from individual droplets at wavelengths corresponding to morphology-dependent resonances, Optics letters*, 1984, **9**, 499-501.

42. H.-B. Lin, J. D. Eversole and A. J. Campillo, *Spectral properties of lasing microdroplets, JOSA B*, 1992, **9**, 43-50.

43. G. F. Christopher and S. L. Anna, *Microfluidic methods for generating continuous droplet streams, Journal of Physics D: Applied Physics*, 2007, **40**, R319.

44. Z. Z. Chong, S. H. Tan, A. M. Gañán-Calvo, S. B. Tor, N. H. Loh and N.-T. Nguyen, *Active droplet generation in microfluidics, Lab on a Chip*, 2016, **16**, 35-58.

45. A. Kiraz, Y. Karadağ and A. Coskun, *Spectral tuning of liquid microdroplets standing on a superhydrophobic surface using electrowetting, Applied Physics Letters*, 2008, **92**, 191104.

46. A. Bakal, C. Vannahme, A. Kristensen and U. Levy, *Tunable on chip optofluidic laser, Applied Physics Letters*, 2015, **107**, 211105.

47. Z. Li, Z. Zhang, A. Scherer and D. Psaltis, *Mechanically tunable optofluidic distributed feedback dye laser, Optics express*, 2006, **14**, 10494-10499.

48. Q. Chen, H. Liu, W. Lee, Y. Sun, D. Zhu, H. Pei, C. Fan and X. Fan, *Self-assembled DNA tetrahedral optofluidic lasers with precise and tunable gain control, Lab on a Chip*, 2013, **13**, 3351-3354.

49. Y. Sun, S. I. Shopova, C.-S. Wu, S. Arnold and X. Fan, *Bioinspired optofluidic FRET lasers via DNA scaffolds, Proc. Natl. Acad. Sci. USA*, 2010, **107**, 16039-16042.

50. Y. Sun and X. Fan, *Distinguishing DNA by Analog-to-Digital-like Conversion by Using Optofluidic Lasers, Angew. Chem. Int. Ed.*, 2012, **51**, 1236-1239.

51. M. C. Gather and S. H. Yun, *Single-cell biological lasers, Nat. Photon.*, 2011, **5**, 406-410.

52. Y.-C. Chen, X. Tan, Q. Sun, Q. Chen, W. Wang and X. Fan, *Laser-emission imaging of nuclear biomarkers for high-contrast cancer screening and immunodiagnosis, Nat. Biomed. Eng.*, 2017, **1**, 724-735.

53. W. Wang, C. Zhou, T. Zhang, J. Chen, S. Liu and X. Fan, *Optofluidic laser array based on stable high-Q Fabry–Pérot microcavities, Lab Chip*, 2015, **15**, 3862-3869.

54. A. Bakal, C. Vannahme, A. Kristensen and U. Levy, *Tunable on chip optofluidic laser, Appl. Phys. Lett.*, 2015, **107**, 211105.

55. Z. Li, Z. Zhang, A. Scherer and D. Psaltis, *Mechanically tunable optofluidic distributed feedback dye laser, Opt. Express*, 2006, **14**, 10494-10499.

56. W. Song, A. E. Vasdekis, Z. Li and D. Psaltis, *Optofluidic evanescent dye laser based on a distributed feedback circular grating, Appl. Phys. Lett.*, 2009, **94**, 161110.

57. S. Lacey, I. M. White, Y. Sun, S. I. Shopova, J. M. Cupps, P. Zhang and X. Fan, *Versatile opto-fluidic ring resonator lasers with ultra-low threshold, Opt. Express*, 2007, **15**, 15523-15530.

58. Y. Sun, J. D. Suter and X. Fan, *Robust integrated optofluidic-ring-resonator dye lasers, Opt. Lett.*, 2009, **34**, 1042-1044.

59. E. Mobini, B. Abaie, M. Peysokhan and A. Mafi, *Spectral selectivity in optical fiber capillary dye lasers, Optics Letters*, 2017, **42**, 1784-1787.

60. M. Aas, A. Jonáš, A. Kiraz, O. Brzobohatý, J. Ježek, Z. Pilát and P. Zemánek, *Spectral tuning of lasing emission from optofluidic droplet microlasers using optical stretching, Opt. Express*, 2013, **21**, 21380-21394.

61. S. K. Tang, Z. Li, A. R. Abate, J. J. Agresti, D. A. Weitz, D. Psaltis and G. M. Whitesides, *A multi-color fast-switching microfluidic droplet dye laser, Lab Chip*, 2009, **9**, 2767-2771.

62. H. Azzouz, L. Alkhafadiji, S. Balslev, J. Johansson, N. A. Mortensen, S. Nilsson and A. Kristensen, *Levitated droplet dye laser, Opt. Express*, 2006, **14**, 4374-4379.

63. A. Kiraz, A. Sennaroglu, S. Doğanay, M. Dündar, A. Kurt, H. Kalaycıoğlu and A. Demirel, *Lasing from single, stationary, dye-doped glycerol/water microdroplets located on a superhydrophobic surface, Opt. Commun.*, 2007, **276**, 145-148.

64. H. Zhang, A. Balram, D. D. Meng and Y. Sun, *Optofluidic Lasers with Monolayer Gain at the Liquid–Liquid Interface, ACS Photonics*, 2017, **4**, 621-625.

65. B. Zhen, S.-L. Chua, J. Lee, A. W. Rodriguez, X. Liang, S. G. Johnson, J. D. Joannopoulos, M. Soljačić and O. Shapira, *Enabling enhanced emission and low-threshold lasing of organic molecules using special Fano resonances of macroscopic photonic crystals, Proc. Natl. Acad. Sci. USA*, 2013, **110**, 13711-13716.

66. M. Tanyeri, R. Perron and I. M. Kennedy, *Lasing droplets in a microfabricated channel, Opt. Lett.*, 2007, **32**, 2529-2531.

67. M. Aas, A. Jonáš and A. Kiraz, *Lasing in optically manipulated, dye-doped emulsion microdroplets, Opt. Commun.*, 2013, **290**, 183-187.

68. S.-H. Huang, W.-H. Tan, F.-G. Tseng and S. Takeuchi, *A monolithically three-dimensional flow-focusing device for formation of single/double emulsions in closed/open microfluidic systems, J. Micromech. Microeng.*, 2006, **16**, 2336.

69. S. Okushima, T. Nisisako, T. Torii and T. Higuchi, *Controlled production of monodisperse double emulsions by two-step droplet breakup in microfluidic devices, Langmuir*, 2004, **20**, 9905-9908.

70. C. Cramer, P. Fischer and E. J. Windhab, *Drop formation in a co-flowing ambient fluid, Chem. Eng. Sci.*, 2004, **59**, 3045-3058.

71. Y. Liu, D. Ganser, A. Schneider, R. Liu, P. Grodzinski and N. Kroutchinina, *Microfabricated polycarbonate CE devices for DNA analysis, Anal. Chem.*, 2001, **73**, 4196-4201.

72. C.-H. Chan, J.-K. Chen and F.-C. Chang, *Specific DNA extraction through fluid channels with immobilization of layered double hydroxides on polycarbonate surface, Sens. Actuator B-Chem.*, 2008, **133**, 327-332.

73. D. Ogończyk, J. Węgrzyn, P. Jankowski, B. Dąbrowski and P. Garstecki, *Bonding of microfluidic devices fabricated in polycarbonate, Lab Chip*, 2010, **10**, 1324-1327.

74. P. Jankowski, D. Ogończyk, L. Derzsi, W. Lisowski and P. Garstecki, *Hydrophilic polycarbonate chips for generation of oil-in-water (O/W) and water-in-oil-in-water (W/O/W) emulsions, Microfluid. Nanofluidics*, 2013, **14**, 767-774.

75. M. Aas, A. Jonáš and A. Kiraz, *Lasing in optically manipulated, dye-doped emulsion microdroplets, Optics Communications*, 2013, **290**, 183-187.

76. Q. Chen, M. Ritt, S. Sivaramakrishnan, Y. Sun and X. Fan, *Optofluidic lasers with a single molecular layer of gain, Lab on a Chip*, 2014, **14**, 4590-4595.

77. Q. Chen, X. Zhang, Y. Sun, M. Ritt, S. Sivaramakrishnan and X. Fan, *Highly sensitive fluorescent protein FRET detection using optofluidic lasers, Lab on a Chip*, 2013, **13**, 2679-2681.

78. M. Tanyeri and I. M. Kennedy, *Detecting single bacterial cells through optical resonances in microdroplets, Sensor letters*, 2008, **6**, 326-329.

79. M. Humar and I. Muševič, *Surfactant sensing based on whispering-gallery-mode lasing in liquid-crystal microdroplets, Optics express*, 2011, **19**, 19836-19844.

80. X. Fan and I. M. White, *Optofluidic microsystems for chemical and biological analysis, Nature photonics*, 2011, **5**, 591.

81. X. Fan and S.-H. Yun, *The potential of optofluidic biolasers, Nature methods*, 2014, **11**, 141.

82. Y. Sun and X. Fan, *Distinguishing DNA by Analog-to-Digital-like Conversion by Using Optofluidic Lasers, Angewandte Chemie*, 2012, **124**, 1262-1265.

83. Y. Karadag, M. Aas, A. Jonáš, S. Anand, D. McGloin and A. Kiraz, *Dye lasing in optically manipulated liquid aerosols, Optics letters*, 2013, **38**, 1669-1671.

84. W. Song, A. E. Vasdekis, Z. Li and D. Psaltis, *Low-order distributed feedback optofluidic dye laser with reduced threshold, Applied Physics Letters*, 2009, **94**, 051117.

85. J. Galas, J. Torres, M. Belotti, Q. Kou and Y. Chen, *Microfluidic tunable dye laser with integrated mixer and ring resonator, Applied Physics Letters*, 2005, **86**, 264101.

86. J. Galas, C. Peroz, Q. Kou and Y. Chen, *Microfluidic dye laser intracavity absorption, Applied physics letters*, 2006, **89**, 224101.

87. G. Aubry, S. Méance, A.-M. Haghiri-Gosnet and Q. Kou, *Flow rate based control of wavelength emission in a multicolor microfluidic dye laser, Microelectronic Engineering*, 2010, **87**, 765-768.

88. M. C. Gather and S. H. Yun, *Lasing from Escherichia coli bacteria genetically programmed to express green fluorescent protein, Optics letters*, 2011, **36**, 3299-3301.

89. A. J. Kuehne, M. C. Gather, I. A. Eydelnant, S.-H. Yun, D. A. Weitz and A. R. Wheeler, *A switchable digital microfluidic droplet dye-laser, Lab on a Chip*, 2011, **11**, 3716-3719.

90. M. Humar, M. C. Gather and S.-H. Yun, *Cellular dye lasers: lasing thresholds and sensing in a planar resonator, Optics express*, 2015, **23**, 27865-27879.

91. M. Karl, C. P. Dietrich, M. Schubert, I. D. W. Samuel, G. A. Turnbull and M. C. Gather, *Single cell induced optical confinement in biological lasers, Journal of Physics D: Applied Physics*, 2017, **50**, 084005.

92. B. Zhen, S.-L. Chua, J. Lee, A. W. Rodriguez, X. Liang, S. G. Johnson, J. D. Joannopoulos, M. Soljačić and O. Shapira, *Enabling enhanced emission and low-threshold lasing of organic molecules using special Fano resonances of macroscopic photonic crystals, Proceedings of the National Academy of Sciences*, 2013, **110**, 13711-13716.

93. R. C. Polson and Z. V. Vardeny, *Random lasing in human tissues, Applied physics letters*, 2004, **85**, 1289-1291.

94. Q. Song, S. Xiao, Z. Xu, J. Liu, X. Sun, V. Drachev, V. M. Shalaev, O. Akkus and Y. L. Kim, *Random lasing in bone tissue, Optics letters*, 2010, **35**, 1425-1427.

95. B. Shivakiran Bhaktha, N. Bachelard, X. Noblin and P. Sebbah, *Optofluidic random laser, Applied Physics Letters*, 2012, **101**, 151101.

96. N. Bachelard, S. Gigan, X. Noblin and P. Sebbah, *Adaptive pumping for spectral control of random lasers, Nature physics*, 2014, **10**, 426.

97. M. Maeda, S. Miyawaki, A. Abe, Y. Oki, H. Watanabe and M. Tanaka, 2004.

98. T. Watanabe, H. Abe, Y. Nishijima and T. Baba, *Array integration of thousands of photonic crystal nanolasers, Applied Physics Letters*, 2014, **104**, 121108.

99. Y. Oki, S. Miyamoto, M. Maeda and N. J. Vasa, *Multiwavelength distributed-feedback dye laser array and its application to spectroscopy, Optics letters*, 2002, **27**, 1220-1222.

100. Y. Oki, S. Miyawaki, M. Maeda and M. Tanaka, *Spectroscopic applications of integrated tunable solid-state dye laser, Optical review*, 2005, **12**, 301.

101. S. Omi, H. Watanabe, Y. Yang and Y. Oki, 2009.

102. S. Lee and S. Lee, *Micro total analysis system (μ-TAS) in biotechnology, Applied microbiology and biotechnology*, 2004, **64**, 289-299.

103. Y. Oki, S. Kataoka, N. Kamogawa, H. Watanabe, K. Yamashita and M. Miyazaki, 2008.

104. M. Iqbal, M. A. Gleeson, B. Spaugh, F. Tybor, W. G. Gunn, M. Hochberg, T. Baehr-Jones, R. C. Bailey and L. C. Gunn, *Label-free biosensor arrays based on silicon ring resonators and high-speed optical scanning instrumentation, IEEE Journal of Selected Topics in Quantum Electronics*, 2010, **16**, 654-661.

105. S. Wondimu, M. Hippler, C. Hussal, A. Hofmann, S. Krämmer, J. Lahann, H. Kalt, W. Freude and C. Koos, *Robust label-free biosensing using microdisk laser arrays with on-chip references, Optics express*, 2018, **26**, 3161-3173.

106. P. Garstecki, M. J. Fuerstman, H. A. Stone and G. M. Whitesides, *Formation of droplets and bubbles in a microfluidic T-junction—scaling and mechanism of break-up, Lab on a Chip*, 2006, **6**, 437-446.

107. A. S. Utada, A. Fernandez-Nieves, H. A. Stone and D. A. Weitz, *Dripping to jetting transitions in coflowing liquid streams, Physical review letters*, 2007, **99**, 094502.

108. M. Hashimoto, P. Garstecki and G. M. Whitesides, *Synthesis of Composite Emulsions and Complex Foams with the use of Microfluidic Flow-Focusing Devices, Small*, 2007, **3**, 1792-1802.

109. A. E. Siegman, *Lasers university science books, Mill Valley, CA*, 1986, **37**, 169.

110. Z. Li and D. Psaltis, *Optofluidic distributed feedback dye lasers, IEEE Journal of Selected Topics in Quantum Electronics*, 2007, **13**, 185-193.

111. Y. Chen, L. Lei, K. Zhang, J. Shi, L. Wang, H. Li, X. Zhang, Y. Wang and H. L. Chan, *Optofluidic microcavities: Dye-lasers and biosensors, Biomicrofluidics*, 2010, **4**, 043002.

112. X. Wu, M. K. K. Oo, K. Reddy, Q. Chen, Y. Sun and X. Fan, *Optofluidic laser for dual-mode sensitive biomolecular detection with a large dynamic range, Nature communications*, 2014, **5**, 3779.

113. Q. Chen, H. Liu, W. Lee, Y. Sun, D. Zhu, H. Pei, C. Fan and X. Fan, *Self-assembled DNA tetrahedral optofluidic lasers with precise and tunable gain control, Lab Chip*, 2013, **13**, 3351-3354.

114. W. Song, A. E. Vasdekis, Z. Li and D. Psaltis, *Optofluidic evanescent dye laser based on a distributed feedback circular grating, Applied Physics Letters*, 2009, **94**, 161110.

115. J. Schafer, J. P. Mondia, R. Sharma, Z. Lu, A. Susha, A. Rogach and L. Wang, *Quantum dot microdrop laser, Nano letters*, 2008, **8**, 1709-1712.

116. X. Wu, Q. Chen, Y. Sun and X. Fan, *Bio-inspired optofluidic lasers with luciferin, Applied Physics Letters*, 2013, **102**, 203706.

117. M. T. Hill, H. J. Dorren, T. De Vries, X. J. Leijtens, J. H. Den Besten, B. Smalbrugge, Y.-S. Oei, H. Binsma, G.-D. Khoe and M. K. Smit, *A fast low-power optical memory based on coupled micro-ring lasers, nature*, 2004, **432**, 206-209.

118. J. Zhu, S. K. Ozdemir, Y.-F. Xiao, L. Li, L. He, D.-R. Chen and L. Yang, *On-chip single nanoparticle detection and sizing by mode splitting in an ultrahigh-Q microresonator, Nature Photonics*, 2010, **4**, 46-49.

119. C.-H. Huang and J. Mason, *Geometric packing constraints in egg phosphatidylcholine vesicles, Proceedings of the National Academy of Sciences*, 1978, **75**, 308-310.

120. I. N. Kurniasih, H. Liang, P. C. Mohr, G. Khot, J. r. P. Rabe and A. Mohr, *Nile red dye in aqueous surfactant and micellar solution, Langmuir*, 2015, **31**, 2639-2648.

121. S. Holler, N. L. Goddard and S. Arnold, *Spontaneous emission spectra from microdroplets, The Journal of chemical physics*, 1998, **108**, 6545-6547.

122. L. Folan and S. Arnold, *Determination of molecular orientation at the surface of an aerosol particle by morphology-dependent photoselection, Optics letters*, 1988, **13**, 1-3.

123. A. Ruaudel-Teixier and M. Vandevyver, *Energy transfer in dye monomolecular layers, Thin Solid Films*, 1980, **68**, 129-133.

124. A. Balram, S. Santhanagopalan, B. Hao, Y. K. Yap and D. D. Meng, *Electrophoretically-Deposited Metal-Decorated CNT Nanoforests with High Thermal/Electric Conductivity and Wettability Tunable from Hydrophilic to Superhydrophobic, Advanced Functional Materials*, 2016, **26**, 2571-2579.

125. D. Dubal, A. Jagadale, S. Patil and C. Lokhande, *Simple route for the synthesis of supercapacitive Co–Ni mixed hydroxide thin films, Materials Research Bulletin*, 2012, **47**, 1239-1245.

126. J. Yong, Q. Yang, F. Chen, H. Bian, G. Du, U. Farooq and X. Hou, *Reversible Underwater Lossless Oil Droplet Transportation, Advanced Materials Interfaces*, 2015, **2**, n/a-n/a.

127. U. Manna and D. M. Lynn, *Synthetic Surfaces with Robust and Tunable Underwater Superoleophobicity, Advanced Functional Materials*, 2015, **25**, 1672-1681.

128. Y.-H. Chang, Y.-T. Huang, M. K. Lo, C.-F. Lin, C.-M. Chen and S.-P. Feng, *Electrochemical fabrication of transparent nickel hydroxide nanostructures with tunable superhydrophobicity/superhydrophilicity for 2D microchannels application, J. Mater. Chem. A*, 2014, **2**, 1985-1990.

129. A. F. Stalder, T. Melchior, M. Müller, D. Sage, T. Blu and M. Unser, *Low-bond axisymmetric drop shape analysis for surface tension and contact angle measurements of sessile drops, Colloids and Surfaces A: Physicochemical and Engineering Aspects*, 2010, **364**, 72-81.

130. K. Wang, Y. Lu, J. Xu and G. Luo, *Determination of dynamic interfacial tension and its effect on droplet formation in the T-shaped microdispersion process, Langmuir*, 2009, **25**, 2153-2158.

131. B. Saremi, M.-Y. Wei, Y. Liu, B. Cheng and B. Yuan, *Re-evaluation of biotin-streptavidin conjugation in Förster resonance energy transfer applications, Journal of biomedical optics*, 2014, **19**, 085008.

132. D. Magde, R. Wong and P. G. Seybold, *Fluorescence quantum yields and their relation to lifetimes of rhodamine 6G and fluorescein in nine solvents: improved absolute standards for quantum yields, Photochemistry and photobiology*, 2002, **75**, 327-334.

133. A. Deshpande, A. Beidoun, A. Penzkofer and G. Wagenblast, *Absorption and emission spectroscopic investigation of cyanovinyldiethylaniline dye vapors, Chemical Physics*, 1990, **142**, 123-131.

134. R. K. Chang and A. J. Campillo, *Optical processes in microcavities*, World scientific, 1996.

135. K. J. Vahala, *Optical microcavities, Nature*, 2003, **424**, 839-846.

136. R. Chen and H. D. Sun, *Tuning whispering gallery mode lasing from self-assembled polymer droplets, Scientific reports*, 2013, **3**, 1-5.

137. F. Vollmer and S. Arnold, *Whispering-gallery-mode biosensing: label-free detection down to single molecules, Nature methods*, 2008, **5**, 591.

138. F. Vollmer, S. Arnold and D. Keng, *Single virus detection from the reactive shift of a whispering-gallery mode, Proceedings of the National Academy of Sciences*, 2008, **105**, 20701-20704.

Biographical Information

Dr. Han Zhang received his Bachelor of Science degree in Opto-Electronic Information Engineering from Huazhong University of Science and Technology in 2014, then received his PhD degree in Electric Engineering from the University of Texas at Arlington in 2020. His research has been focusing on the development of on-chip Optofluidic laser systems. He has successfully demonstrated optofluidic droplet lasers with micro-nozzle structures, further developed a droplet laser array and a droplet-on-demand on-chip optofluidic laser system. He also demonstrated droplet laser systems with a monolayer gain medium, which has potentials in biological studies at the molecular level. Next, Dr. Zhang is going to focus on integrating an on-chip laser source onto an optofluidic detection system and the development of an on-chip nanopore sensor.